ADVANCED STEEL CONSTRUCTION

An International Journal

Volume 10 Number 3

September 2014

CONTENTS

Technical Papers

Website: *http://www.hkisc.org*
ISSN 1816-112X
Science Citation Index Expanded, Materials Science Citation Index and ISI Alerting

Cover: Flower Dome Conservatories @Gardens by The Bay, Singapore

ADVANCED STEEL CONSTRUCTION

VOL.10, NO.3 (2014)

ADVANCED STEEL CONSTRUCTION

an International Journal

ISSN 1816-112X

Volume 10 Number 3 *September 2014*

ISSN 1816-112X

Science Citation Index Expanded, Materials Science Citation Index and ISI Alerting

Advanced Steel Construction
an international journal

Cover: Flower Dome Conservatories @Gardens by The Bay, Singapore
The two arch structures behind the big trees. Grand Award of IStructE-UK/Structural Division-HKIE 2013. Stability design by second-order direct analysis without effective length, jointly by The National University of Singapore and The Hong Kong Polytechnic University

General Information
Advanced Steel Construction, an international journal

Aims and scope

The International Journal of Advanced Steel Construction provides a platform for the publication and rapid dissemination of original and up-to-date research and technological developments in steel construction, design and analysis. Scope of research papers published in this journal includes but is not limited to theoretical and experimental research on elements, assemblages, systems, material, design philosophy and codification, standards, fabrication, projects of innovative nature and computer techniques. The journal is specifically tailored to channel the exchange of technological know-how between researchers and practitioners. Contributions from all aspects related to the recent developments of advanced steel construction are welcome.

Instructions to authors

Submission of the manuscript. Authors may submit double-spaced manuscripts preferably in MS Word by emailing to one of the chief editors as follows for arrangement of review. Alternatively papers can be submitted on a diskette to one of the chief editors.

Asian Pacific , African and organizing editor : Professor S.L. Chan, Email: ceslchan@polyu.edu.hk
American editor : Professor W.F. Chen, Email: waifah@hawaii.edu
European editor : Professor R. Zandonini, Email: riccardo_zandonini@ing.unitn.it

All manuscripts submitted to the journal are recommended to accompany with a list of four potential reviewers suggested by the author(s). This list should include the complete name, address, telephone and fax numbers, email address, and at least five keywords that identify the expertise of each reviewer. This scheme will improve the process of review.

Style of manuscript

General. Author(s) should provide full postal and email addresses and fax number for correspondence. The manuscript including abstract, keywords, references, figures and tables should be in English with pages numbered and typed with double line spacing on single side of A4 or letter-sized paper. The front page of the article should contain:

a) a short title (reflecting the content of the paper);
b) all the name(s) and postal and email addresses of author(s) specifying the author to whom correspondence and proofs should be sent;
c) an abstract of 100-200 words; and
d) 5 to 8 keywords.

The paper must contain an introduction and a conclusion. The length of paper should not exceed 25 journal pages (approximately 15,000 words equivalents).

Tables and figures. Tables and figures including photographs should be typed, numbered consecutively in Arabic numerals and with short titles. They should be referred in the text as Figure 1, Table 2, etc. Originally drawn figures and photographs should be provided in a form suitable for photographic reproduction and reduction in the journal.

Mathematical expressions and units. The Systeme Internationale (SI) should be followed whenever possible. The numbers identifying the displayed mathematical expression should be referred to in the text as Eq. (1), Eq. (2).

References. References to published literature should be referred in the text, in the order of citation with Arabic numerals, by the last name(s) of the author(s) (e.g. Zandonini and Zanon [3]) or if more than three authors (e.g. Zandonini et al. [4]). References should be in English with occasional allowance of 1-2 exceptional references in local languages and reflect the current state-of-technology. Journal titles should be abbreviated in the style of the Word List of Scientific Periodicals. References should be cited in the following style [1, 2, 3].

Journal: [1] Chen, W.F. and Kishi, N., "Semi-rigid Steel Beam-to-column Connections, Data Base and Modelling", Journal of Structural Engineering, ASCE, 1989, Vol. 115, No. 1, pp. 105-119.
Book: [2] Chan, S.L. and Chui, P.P.T., "Non-linear Static and Cyclic Analysis of Semi-rigid Steel Frames", Elsevier Science, 2000.
Proceedings: [3] Zandonini, R. and Zanon, P., "Experimental Analysis of Steel Beams with Semi-rigid Joints", Proceedings of International Conference on Advances in Steel Structures, Hong Kong, 1996, Vol. 1, pp. 356-364.

Proofs. Proof will be sent to the corresponding author to correct any typesetting errors. Alternations to the original manuscript at this stage will not be accepted. Proofs should be returned within 48 hours of receipt by Express Mail, Fax or Email.

Copyright. Submission of an article to "Advanced Steel Construction" implies that it presents the original and unpublished work, and not under consideration for publication nor published elsewhere. On acceptance of a manuscript submitted, the copyright thereof is transferred to the publisher by the Transfer of Copyright Agreement and upon the acceptance of publication for the papers, the corresponding author must sign the form for Transfer of Copyright.

Permission. Quoting from this journal is granted provided that the customary acknowledgement is given to the source.

Page charge and Reprints. There will be no page charges if the length of paper is within the limit of 25 journal pages. A total of 30 free offprints will be supplied free of charge to the corresponding author. Purchasing orders for additional offprints can be made on order forms which will be sent to the authors. These instructions can be obtained at the Hong Kong Institute of Steel Construction, Journal website: http://www.hkisc.org

The International Journal of Advanced Steel Construction is published quarterly by learnt society, The Hong Kong Institute of Steel Construction, c/o Department of Civil & Environmental Engineering, The Hong Kong Polytechnic University, Hung Hom, Kowloon, Hong Kong.

Subscription inquiries and change of address. Address all subscription inquiries and correspondence to Member Records, IJASC. Notify an address change as soon as possible. All communications should include both old and new addresses with zip codes and be accompanied by a mailing label from a recent issue. Allow six weeks for all changes to become effective.

The Hong Kong Institute of Steel Construction
HKISC
c/o Department of Civil and Environmental Engineering,
The Hong Kong Polytechnic University,
Hunghom, Kowloon, Hong Kong, China.
Tel: 852- 2766 6047 Fax: 852- 2334 6389
Email: *ceslchan@polyu.edu.hk* Website: *http://www.hkisc.org/*
ISSN 1816-112X
Science Citation Index Expanded, Materials Science Citation Index and ISI Alerting

ISSN 1816-112X

Science Citation Index Expanded, Materials Science Citation Index and ISI Alerting

Advanced Steel Construction
an international journal

VOLUME 10 NUMBER 3 SEPTEMBER 2014

Technical Papers

EXPERIMENTAL STUDY ON LOAD CAPACITIES OF ISOLATED HEAVY-DUTY SCAFFOLDS USED IN CONSTRUCTION

Jui-Lin Peng [1,*], Chung-Ming Ho [2], Chenyu Chen [3] and Yeong-Bin Yang [1,4]

[1] *Professor, Department of Construction Engineering, National Yunlin University of Science & Technology, Douliou, Yunlin, 64002, Taiwan, ROC.*
[2] *Ph.D. Student, Graduate School of Engineering Science & Technology, National Yunlin University of Science & Technology, Douliou, Yunlin, 64002, Taiwan, ROC.*
[3] *Assistant Professor, Department of Architecture, National Cheng Kung University, Tainan, Taiwan, ROC.*
[4] *Professor, On leave from Department of Civil Engineering, National Taiwan University, Taipei, Taiwan, ROC.*
**(Corresponding author: E-mail: peng.jl@msa.hinet.net and pengjl@yuntech.edu.tw)*

Received: 3 November 2012; Revised: 10 May 2013; Accepted: 30 June 2013

ABSTRACT: The isolated heavy-duty scaffolds, which have higher load capacity, are often considered to serve as the falsework during the construction stage of a building with high clearance, large spans and thick slabs in order to meet the load demand of the building. Because isolated heavy-duty scaffolds serve as temporary structures and are promptly dismantled after the construction is complete, their importance is often neglected. Until now, data regarding the structural design of isolated heavy-duty scaffolds has been rather scarce, and the assembly of isolated heavy-duty scaffolds on construction sites still relies mainly on the experience of construction workers. This phenomenon results in a high risk of collapse of isolated heavy-duty scaffolds actually applied on construction sites. This study explores the critical loads and the failure modes of isolated heavy-duty scaffolds in various setups by testing actual setups of isolated heavy-duty scaffolds on construction sites. The results show that, since the bending moment stiffness provided by the base screw jacks of isolated heavy-duty scaffolds is negligible, the base screw jack has a limited effect on the overall load capacity of isolated heavy-duty scaffolds. When isolated heavy-duty scaffolds are set up on ground with varying elevation or on ground under an inclined top slab with varying elevation, their load capacity is not substantially affected as long as the difference in elevation is less than 56 cm. When assembled in multiple layers on construction sites, isolated heavy-duty scaffolds are often erected with steel tube shores on the top layer. However, this combined scaffolding structure reduces the load capacity of isolated heavy-duty scaffolds by as much as 70%. In this case, directly extending the top screw jacks of the isolated heavy-duty scaffolds is better than using a combined scaffolding structure. As for the isolated heavy-duty scaffolds after being repeatedly used, this study uses a repeated loading test to simulate the lower bound strength of isolated heavy-duty scaffolds on construction sites. Contractors can choose an appropriate reduction factor based on cost and construction safety considerations when engineers design the strengths of reusable isolated heavy-duty scaffolds.

Keywords: Critical load, falsework, heavy-duty scaffold, steel shore

1. INTRODUCTION

Structures that require large spaces such as factory buildings, warehouses and gymnasiums tend to have high headroom, large spans and thick slabs. During construction of these building structures, door-type steel scaffolds and tubular steel adjustable shores are unsuitable for use as falseworks because of their low load capacity. Instead, isolated heavy-duty scaffolds are preferable because of their higher load capacity. Figure 1 shows the isolated heavy-duty scaffolds used during construction of a new factory building with high headroom in Taiwan.

Up to now, no specific design codes have provided design references for isolated heavy-duty scaffolds used on Taiwan construction sites. Therefore, effectively controlling variation in the load carrying capacities of various setups of isolated heavy-duty scaffolds is often difficult. The assembly of isolated heavy-duty scaffolds on construction sites often relies on the experience of

construction workers. This phenomenon increases the risk of collapse in isolated heavy-duty scaffolds actually applied on construction sites. Thus, a clear understanding of the structural behaviors of these scaffolds is essential. Figure 2 shows a falsework that collapsed during grouting on a construction site in Kaohsiung, Taiwan.

Fig ite

Figure 2. Falsework Collapse at a Construction Site in Taiwan

Until now, many construction falseworks have been studied. In terms of modular frame-type scaffolds, Weesner and Jones [1] performed numerical analyses and tests of frame-type steel scaffolding structures to explore the ultimate load carrying capacity of frame-type steel scaffolding structures. Their numerical analysis included both eigen buckling analysis and geometrically nonlinear analysis, and the tests were mainly loading tests.

In terms of modular door-type steel scaffolds, Yu *et al.* [2, 3, 4] explored the load capacities of modular door-type steel scaffolds. Similarly, they performed numerical analyses and loading tests to explore the relationship between layer number and load capacity in modular door-type steel

scaffolds. Huang *et al.* [5, 6] performed numerical analyses and loading tests of door-type steel scaffolds to confirm the relationship between load capacity and layer number in door-type steel scaffolds. Their numerical analysis was performed using an eigenvalue solution. They also derived an analytical solution to establish an analytical model for door-type steel scaffolds.

Peng *et al.* [7, 8, 9, 10, 11] performed a theoretical analysis and experimental study of door-type steel scaffolding systems with varying setups and varying numbers of layers. The theoretical analysis used an analytical solution to establish simplified models of door-type steel scaffolding systems, and the numerical analysis mainly applied second-order elastic with semi-rigid joint analysis. In addition to comparing load capacities between a steel scaffolding system alone and a steel scaffolding system combined with wooden shores, they also compared failure modes between these two systems. Additionally, Kuo *et al.* [12] and Peng *et al.* [13] compared the effects of various loading paths and loading patterns on the load capacities of door-type steel scaffolding systems and analyzed the effects of influence lines on these loads. Additionally, Peng *et al.* [14, 15] also investigated the structural behaviors of modular scaffolds used for finishing of the façade of buildings based on a series of experimental tests and numerical analyses.

In terms of the study of tube and couple scaffolds, Liu *et al.* [16] conducted experimental study on full-scale large-sized tube and couple scaffolds without X-bracing and explored the structural behaviors of the whole tube and couple scaffolding system after loading. In terms of the study of system scaffolds, Peng *et al.* [17] conducted numerical analysis and experimental study to explore the load capacities and failure modes of system scaffolds with different setups. In terms of the reliability and the probabilistic studies of steel scaffolds, Zhang *et al.* [18, 19] conducted the reliability analyses of the scaffolding systems and explored the variability of parameters related to the use of steel scaffolds, such as semi-rigid stiffness, load eccentricities and initial geometric imperfections.

The above researches show that falsework-related studies have mainly focused on the temporary supports for frame-type steel scaffolds, door-type steel scaffolds, tube and couple scaffolds, and system scaffolds. Studies of isolated heavy-duty scaffolds are relatively rare. Since the dimensions and the assemblies of isolated heavy-duty scaffolds substantially differ from those of other scaffolds, previous falsework-related studies can serve only as references and are not directly applicable to isolated heavy-duty scaffolds. Therefore, the load capacities and failure models of isolated heavy-duty scaffolds require further study.

2. RESEARCH OBJECTIVE AND TEST PLANNING

2.1 Research Objective

This study explored the load carrying capacities and failure modes of isolated heavy duty scaffolds by comparing the loading test results of various setups of isolated heavy-duty scaffolds actually used on construction sites. Hopefully, the results of this study can be directly used in the construction industry as a reference for strength design of isolated heavy-duty scaffolds. Serving as temporary structures during the construction stage, the isolated heavy-duty scaffolds used on construction sites have diverse setups and qualities. Thus, this preliminary research appropriately focuses on loading tests in order to realize the actual failure models of isolated heavy-duty scaffolds. After that, the further analytical study will be conducted based on these test results.

2.2 Test Planning

Five main tests were performed in isolated heavy-duty scaffolds: (1) the effect of stiffness of base screw jacks on load capacity, (2) the effect of top slope and inclined ground on load capacity, (3) the effect of extension of top and base screw jacks on load capacity, (4) the effect of steel tube shores added at the top of isolated heavy-duty scaffolds on load capacity, (5) the lower limit of load capacity of reusable scaffolds. The procedures for performing the tests are summarized below.

2.2.1 Two-layer basic setup

This test explored the load capacities and failure modes of a basic two-layer setup for isolated heavy-duty scaffolds. The test results can be used to compare with those of other setups of isolated heavy-duty scaffolds used in this study. In the two-layer basic setup, the height of each layer is 150 cm, and the height of both top and base screw jacks is 20 cm. The scaffolds are reinforced with plane braces as shown in Figure 3.

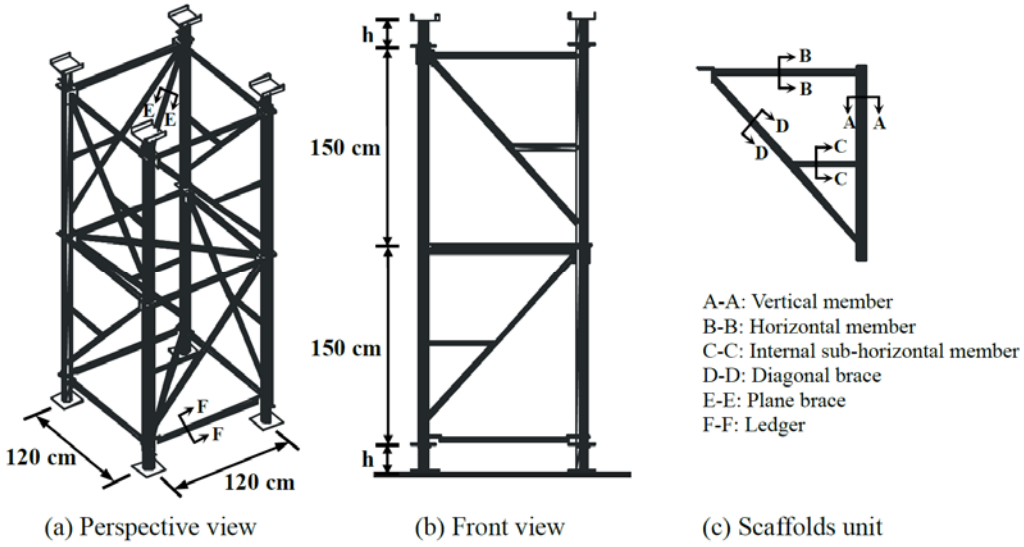

Figure 3. Test configuration for Two-layer Basic Setup and Cross-sectional Positions of Isolated Heavy-duty Scaffold Unit

2.2.2 Two-layer basic setup with non-stiffened base screw jacks

To determine how the stiffness of base screw jacks affects the load capacity, a two-layer basic test setup was used with the base plates of the base screw jacks cut off so that, when the deformation and failure of the scaffolds occur, the base screw jacks would not provide additional bending moment stiffness. In further analyses, the boundary condition of this base screw jack without the base plate can be considered as a hinge joint. Figure 4 shows the test configuration.

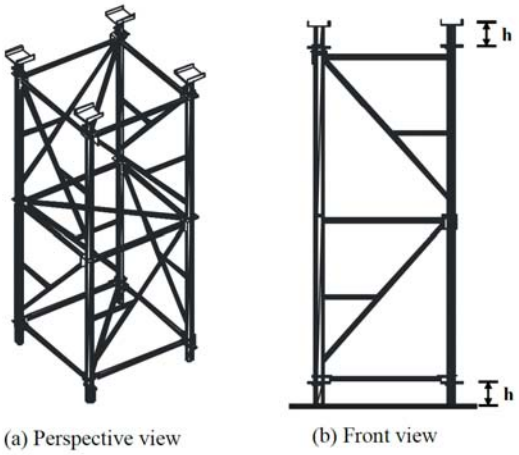

Figure 4. Test Configuration of Two-layer Basic Setup with Non-stiffened Base Screw Jacks

2.2.3 Difference in ground elevation

Driveways or stairways in a building often require the scaffolds setup on ground with varying elevation during the construction stage. This test explores how varying ground elevation affects the load capacities and failure modes of isolated heavy-duty scaffolds. Scaffolds on two different elevations (33.2 cm and 56 cm) are tested. The two elevations 33.2 cm and 56 cm are based on the inclinations of the ground which are 15.5 degrees and 25 degrees, respectively. With the width of the scaffold 120 cm, the elevation 33.2 cm is equal to 120 cm multiplied by tan (15.5°) and the elevation 56 cm is equal to 120 cm multiplied by tan (25°).Figure 5(a) shows the test configuration for scaffolds erected on ground with two different elevations.

In the test configuration for a 33.2 cm difference in elevation, the height of the front row base screw jacks is adjusted to 20 cm, and that of the back row base screw jacks is adjusted to 53.2 cm (=33.2+20). Each scaffold layer is 150 cm high, and both layers are reinforced with plane braces. The height of top screw jacks is adjusted to 20 cm. The test configuration for the 56 cm difference in ground elevation is the same as the test configuration for the 33.2 cm difference in ground elevation with the exception of the back row base screw jacks, which are adjusted to 76 cm (=56+20).

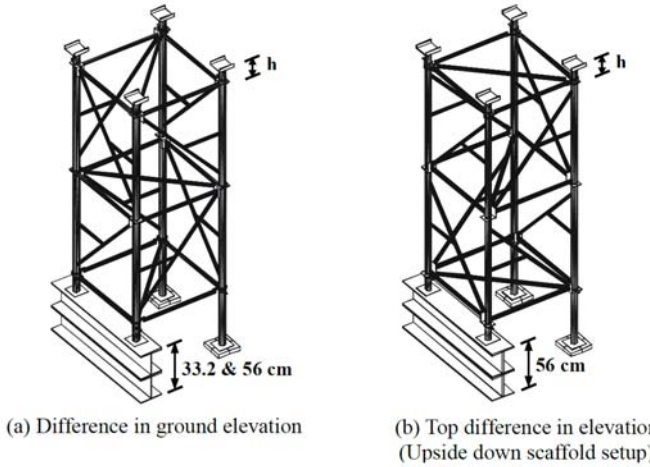

Figure 5. Test Configuration of Two-layer Setup with Difference in Elevation between Top and Ground

2.2.4 Top difference in elevation

To cope with the height of roof beams or slabs during the construction of a building, scaffolding height may differ because of varying heights of roof beams or slabs. A 56 cm difference in scaffolding height was tested. Since the steel loading-holder is on the top of the oil pressure machine, configuring scaffolds with top difference in elevation was very difficult in the laboratory. The solution was to simulate the top difference in elevation of the scaffolds on the ground by performing the tests with the scaffolding structure assembled upside down. In the test configuration for scaffolds with 56 cm top difference in elevation, other than the scaffolding structure is put upside down, the remaining structures were measured using the same test configuration used for the 56 cm difference in ground elevation, including all screw jacks and blocks (as described in the previous section). Figure 5(b) shows the test configuration.

2.2.5 Extension of top screw jacks

Since each layer is 1.5 m high, the total height of a multiple-layer isolated heavy-duty scaffold is often insufficient for the full headroom of the interior of a construction structure. In this case, extending the top screw jacks to fill the gap is advised. Figure 6 shows the test configuration.

Two-layer isolated heavy-duty scaffolds are tested. The top screw jacks of the scaffolds are extended to 75 cm, and the height of the base screw jacks is 20 cm. The height of each layer of the scaffolds is 150 cm, and both layers are reinforced with plane braces.

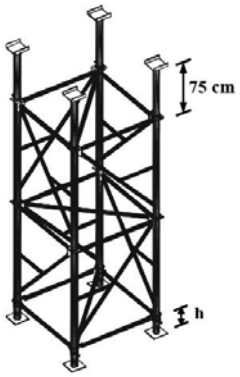

Figure 6. Test Configuration of Two-layer Setup with Extension of Top Screw Jacks

2.2.6 Extension of both top and base screw jacks

To solve the problem discussed above regarding the gap between the scaffolds and slab, the base screw jacks should also be extended when the extended top screw jacks cannot fill up the gap. In other words, both the top and base screw jacks should be extended to fill the gap between the scaffolds and slabs (Figure 7). The test configuration extends both the top and base screw jacks of the two-layer isolated heavy-duty scaffolds to 75 cm, respectively. Each scaffold layer is 150 cm high, and both layers are reinforced with plane braces.

2.2.7 Steel tube shores with and without enclosed restraint on top of the scaffolds

Similarly, the above problem of the gap between the scaffolds and slabs observed during the site investigation is often solved by adding steel tube shores on top of the scaffolds to fill the gap between the scaffolds and slab. The steel tubes can also be reinforced by horizontal enclosed restraint with stringers. This study tested the load capacities and failure modes of this combined

scaffolding structure, *i.e.*, steel tube shores added to the top of isolated heavy-duty scaffolds. Figure 8 shows the test configuration of the scaffolds reinforced with steel tube shores without enclosed restraint. Figure 9 shows the test configuration of the scaffolds reinforced with steel tube shores with enclosed restraint.

For the test configuration of the scaffolds reinforced with steel tube shores without enclosed restraint, the scaffold assembly is identical to that in the basic two-layer setup described above. This study simulated the configuration actually used on construction sites by placing two I-beams (200 cm long, 15 cm high) on the top screw jacks of the scaffolds. Four steel tube shores (44 cm in length) are mounted on top of the I-beams by clamps as shown in Figure 9. Both the top and bottom ends of the steel tube shores are fixed with screw jacks of door-type steel scaffolds, with the bottom end fixed on the I-beams by four clamps and with the top ends sticking against the loading-holder of the test machine. The screw jack of the door-type steel scaffolds is 5 cm, and the length inserted into the steel tube of scaffolds is 10 cm.

The scaffolds reinforced with steel tube shores "with" and "without" enclosed restraints are configured similarly. The only difference is that four reinforced horizontal stringers for the "with" case are fixed with swivel couplers at the centers of the steel tube shores on top of the scaffolds.

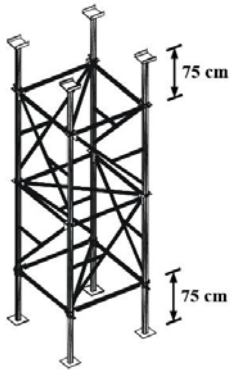

Figure 7. Test Configuration of Two-layer Setup with Extension of Both Top and Base Screw Jacks

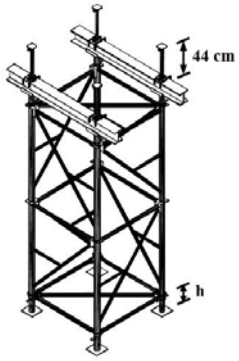

Figure 8. Test Configuration of Two-layer Setup Reinforced with Steel Tube Shores without Enclosed Restraint

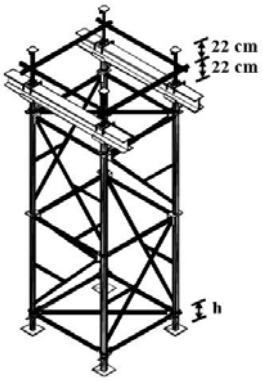

Figure 9. Test Configuration of Two-layer Setup Reinforced with Steel Tube Shores with Enclosed Restraint

2.2.8 Lower strength bound of reusable scaffolds

On construction sites, the isolated heavy-duty scaffolds are usually assembled with reusable scaffolds. To obtain the load capacity of these reusable scaffolds in the worst condition, reloading the scaffolds is advised. A second loading is performed after finishing the first loading and then readjusting the scaffolds. When the first-loading test finishes and unloads, the deformed scaffolds are reinstalled and their setups are based on those of the first-loading tests as far as possible. This study defines the re-installed process of scaffolds as the readjusting. The load capacity of the scaffolds obtained at the second loading can be considered the lower limit of the load capacity of reusable scaffolds. The quotient obtained by dividing the lower limit value of load capacity of the second loading by that of the first loading gives the reduction in the strength of the reusable isolated heavy-duty scaffolds.

3. CROSS-SECTIONAL DIMENSIONS AND MATERIAL PROPERTIES

Figures 3(a) and 3(c) give the cross-sectional positions measured in multiple sets of isolated heavy-duty scaffolds where A-A is the vertical member of the scaffold unit: D (diameter) = 76.5 $\pm$ 0.5mm, t (thickness) = 3.2 $\pm$ 0.1mm; B-B is the horizontal member of the scaffold unit: D = 40.2 $\pm$ 0.2mm, t = 2.1 $\pm$ 0.1mm; C-C is the internal sub-horizontal member of the scaffold unit: D = 33.4 $\pm$ 0.1mm, t = 2.0 $\pm$ 0.1mm; D-D is the diagonal brace of the scaffold unit: D = 33.4 $\pm$ 0.1mm, t = 1.8 $\pm$ 0.1mm; E-E is the plane brace: D = 42.3 $\pm$ 0.1mm, t = 1.9 $\pm$ 0.1mm; F-F is the ledger: D = 42.4 $\pm$ 0.2mm, t = 2.4 $\pm$ 0.2mm. Three scaffold units were randomly selected for elastic modulus test of the materials. The average value of elastic modulus of the scaffold units was 19,982kN/cm^2, which approximates the nominal value of 20,012.4kN/cm^2.

4. RESULTS AND DISCUSSIONS

4.1 Two-layer Basic Setup

The two tests (A and B) performed for this setup showed that the failure loads of the isolated heavy-duty scaffolds are 894.003 kN and 920.688 kN, respectively, and that the vertical deformations of the scaffolds under maximum loads are 20.575 mm and 21.208 mm, respectively. Table 1 shows the test results.

Figure 10 shows the P-Δ curve (curve of loads and vertical deformations) for the results of test A under the first and second loadings. The curve for the first loading shows that the load and deformation relationship increases linearly. When the load increases to the maximum value of 894.003 kN, the vertical deformation is 20.575 mm. After the buckling failure occurs, the load decreases rapidly. Figure 11 shows the failure mode of the scaffolds. The left-rear vertical member of the first layer and the right-rear vertical member of the second layer are severely deformed, and an inclination in the top screw jacks results from severe deformation of the vertical members.
After the first loading, the scaffolds were unloaded and then readjusted. After these, we applied the second loading to simulate the load capacity of the reusable scaffolds in the worst case. The maximum load capacities obtained in tests A and B are 288.316 kN and 653.534 kN, respectively, and the corresponding vertical deformations are 26.025 mm and 21.750 mm, respectively. The failure modes of the second loading resemble those of the first loading. Figure 10 shows the comparatively flat P-Δ curve obtained in the second loading, which substantially differs from that observed in the first loading. However, vertical deformations are similar in the first and second loadings under maximum load (approximately 2 cm).

Table 1 shows that the average maximum load capacity of the two-layer basic setup scaffolds is 907.346 kN and that the average corresponding vertical deformation is 20.892 mm. The average maximum load capacity of the second loading is 470.925 kN, which is 52% of that of the first loading (=470.925/907.346). The experimental results obtained for this basic setup of isolated heavy-duty scaffolds were then used for the control setup in further tests of other configurations.

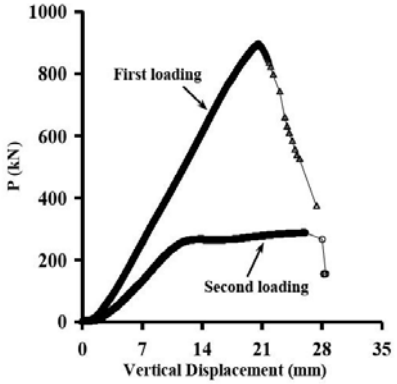

Figure 10. P-Δ Curves of Two-layer Basic Setup under the First and Second Loadings in Test A

4.2 Two-layer Basic Setup with Non-stiffened Base Screw Jacks

The test configurations for the two-layer basic setup scaffolds with non-stiffened base screw jacks are identical to those for the two-layer basic setup scaffolds. The only difference is that the non-stiffened base screw jacks are used in these test configurations. That is, the base plate of the base screw jacks is removed so that the jacks do not provide additional bending moment stiffness. Three tests were performed (tests A, B and C). In tests A, B, and C, the maximum load capacities obtained in the first loading are 762.584 kN, 912.560 kN and 899.974 kN, respectively, and the corresponding vertical deformations are 18.319 mm, 20.479 mm and 22.371 mm, respectively. Table 1 shows the test results.

Figure 12 shows the P-Δ curves observed in test A under the first and second loadings. The curve for the first loading shows a linear increase in the load and deformation relationship. At the maximum load of 762.584 kN, the corresponding vertical deformation is 18.319 mm, and buckling failure of the scaffolds occurs immediately. The right-front vertical member of the first layer deforms severely. Figure 13 shows the failure mode of the scaffolds.

Figure 11. Failure Mode A of Two-layer Basic Setup in Test

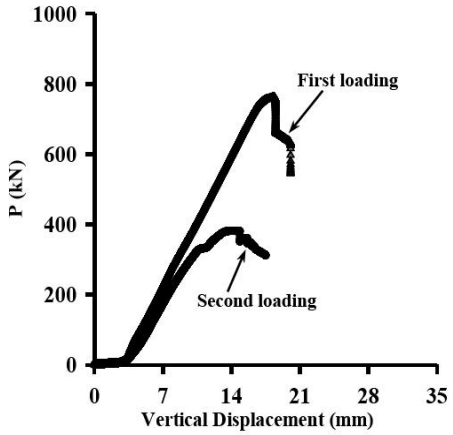

Figure 12. P-Δ Curves of Two-layer Basic Setup with Non-stiffened Base Screw Jacks under the First and Second Loadings in Test A

Figure 13. Failure Mode of Two-layer Setup with Non-stiffened Base Screw Jacks

The maximum load capacities of second loading of tests A, B and C are 382.272kN, 577.229 kN and 623.155 kN, respectively, and the corresponding vertical deformations are 14.200 mm, 15.225 mm and 17.387 mm. The failure modes are similar to those of the first loading. Figure 12 shows that the P-Δ curve obtained under the second loading resembles that observed under the first loading.

Table 1. Results of Loading Tests of Isolated Heavy-duty Scaffolds with Various Configurations

Type	Figure	Test number and (DIE type)	Max. load capacity / Corr. deformation	Test groups (load capacity test value [kN], deformation [mm])					
				Group A	Group B	Group C	Group D	Group E	Average value
Two-layer basic setup		B2HS (△h=0)	1st loading, capacity (2nd loading, capacity)	894.003 (288.316)	920.688 (653.534)	---	---	---	907.346 (470.925)
			1st loading, deformation (2nd loading, deformation)	20.575 (26.025)	21.208 (21.750)	---	---	---	20.892 (23.888)
Two-layer basic setup with non-stiffened base screw jacks		NB2HS (△h=0)	1st loading, capacity (2nd loading, capacity)	762.584 (382.272)	912.560 (577.229)	899.974 (623.155)	---	---	858.373 (527.552)
			1st loading, deformation (2nd loading, deformation)	18.319 (14.200)	20.479 (15.225)	22.371 (17.387)	---	---	20.390 (15.604)
Difference in ground elevation		JHSG(33.2) (△h=33.2)	1st loading, capacity (2nd loading, capacity)	911.671 (515.991)	862.262 (539.247)	---	---	---	886.967 (527.619)
			1st loading, deformation (2nd loading, deformation)	19.450 (13.412)	20.800 (14.731)	---	---	---	20.125 (14.072)
		JHSG(56) (△h =56)	1st loading, capacity (2nd loading, capacity)	875.120 (565.270)	905.383 (720.106)	---	---	---	890.252 (642.688)
			1st loading, deformation (2nd loading, deformation)	20.600 (15.283)#	21.288 (27.163)#	---	---	---	20.944 (21.223)
Top difference in elevation		PHSU(56) (△h =56)	1st loading, capacity (2nd loading, capacity)	998.337 (720.458)	883.406 (496.046)	---	---	---	940.872 (608.252)
			1st loading, deformation (2nd loading, deformation)	21.475 (17.500)	20.319 (15.987)	---	---	---	20.897 (16.744)
Extension of top screw jacks		UJ75HS Ext. 75cm (△h =0)	1st loading, capacity (2nd loading, capacity)	912.533 (613.863)	846.912 (530.194)	780.047 (490.530)	824.617 (609.762)	---	841.027 (561.087)
			1st loading, deformation (2nd loading, deformation)	22.338 (20.419)	21.425 (19.288)	24.463 (24.213)	21.338 (17.775)	---	22.391 (20.424)
Extension of both top and base screw jacks		UJ75J75HS Ext. 75cm (△h =0)	1st loading, capacity (2nd loading, capacity)	813.937 (266.141)	878.900 (365.079)	963.234 (212.806)	672.834 (370.881)	849.996 (298.410)	835.780 (302.663)
			1st loading, deformation (2nd loading, deformation)	21.700 (20.125)	21.538 (22.000)	23.663 (28.913)	20.006 (15.537)	21.750 (18.881)	21.731 (21.091)
Steel tube shores without enclosed restraint		USS44HS tube length 44cm (△h =0)	Load capacity	231.210	234.283	---	---	---	232.747
			Deformation	47.689	45.114	---	---	---	46.402
Steel tube shores with enclosed restraint		USSG44HS tube length 44cm (△h =0)	Load capacity	220.610	207.607	---	---	---	214.108
			Deformation	23.836	28.651	---	---	---	26.244

Notes:

1. Figures in brackets represent the results of the second loading.
2. Without specification, all the test configurations have top and base screw jacks.
3. --- : There is no test value.
4. △h : difference in elevation (cm)
5. # : Since the deformation cannot be restored after the first loading, the deformation of the second loading is considered the relative value.

The tests of the two-layer basic setup scaffolds with non-stiffened base screw jacks showed that the average maximum load capacity is 858.373 kN and that the average corresponding vertical deformation is 20.390 mm. The average maximum load capacity of the second loading is 527.552 kN, and the average corresponding vertical deformation is 15.604 mm. The average maximum load capacity of the second loading is 61% (=527.552/858.373)of that of the first loading.

Table 1 shows that the average maximum load capacity of the two-layer setup scaffolds with non-stiffened base screw jacks is 858.373 kN. Comparing with the average maximum load capacity of the two-layer basic setup scaffolds (907.346 kN), the strength of the two-layer basic setup scaffolds with non-stiffness base screw jacks is 95% (=858.373/907.346) of that of the two-layer basic setup scaffolds. That is to say, the bending moment stiffness added by the base screw jacks to the overall scaffold is negligible. This insignificant bending moment results mainly from the short height of the base screw jacks (20 cm) and the placement of the ledgers above the base screw jacks to prevent their deformation. Therefore, with or without the base plates under the base screw jacks, the load capacity of the scaffolds is not substantially affected.

4.3 Difference in Ground Elevation

4.3.1 33.2 cm difference in ground elevation

Two tests (tests A and B) of differences in ground elevation were performed. The maximum load capacities obtained in tests A and B under the first loading are 911.671 kN and 862.262 kN respectively, and the corresponding vertical deformations are 19.450 mm and 20.800 mm. Table 1 shows the test results.

Figure 14 shows the P-Δ curves of the first and second loadings on scaffolds with 33.2 cm difference in ground elevation in test A. The curve obtained for the first loading shows a linear increase in the load and deformation relationship. The maximum load capacity is 911.671 kN, and the corresponding vertical deformation is 19.450 mm. Figure 15 shows the failure mode of the scaffolds.

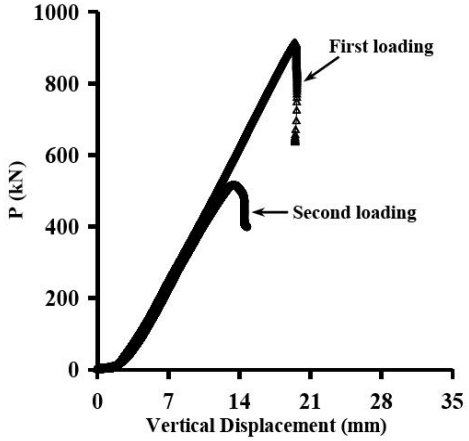

Figure 14. P-Δ Curves of Two-layer Setup with 33.2 cm Difference in Ground Elevation under the First and Second Loadings in Test A

The maximum load capacities of second loading of tests A and B are 515.991 kN and 539.247 kN, respectively, and the corresponding vertical deformations are 13.412 mm and 14.731 mm, respectively. Again, the failure modes resemble those observed in the first loading. Figure 14 shows that the P-Δ curve was similar under the first and second loadings.

Under the first loading, Table 1 shows that the average maximum load capacity of the two-layer scaffolds with 33.2 cm difference in ground elevation is 886.967 kN, and the average corresponding vertical deformation is 20.125 mm. The average maximum load capacity in the second loading is 527.619 kN, and the average corresponding vertical deformation is 14.072 mm. To put it another way, the load capacity of the scaffolds in the second loading is 59% (=527.619/886.967)of that of the first loading. Comparisons showed that the 886.967 kN average maximum load capacity of the two-layer scaffolds with 33.2 cm difference in ground elevation was 98%(=886.967/907.346) of the 907.346 kN maximum load capacity of the two-layer basic setup scaffolds. That implies that the effect of the 33.2 cm difference in ground elevation on the load capacity of isolated heavy-duty scaffolds is not statistically significant.

Figure 15. Failure Mode of Two-layer Setup with 33.2 cm Difference in Ground Elevation

4.3.2 56 cm difference in ground elevation

Tests A and B were performed similarly. The maximum load capacities of the first loading are 875.120 kN and 905.383 kN, respectively, and the corresponding vertical deformations are 20.600 mm and 21.288 mm. Table 1 shows the test results.

Figure 16 shows the P-Δ curves for the first and second loadings on scaffolds with 56 cm difference in ground elevation in test A. Under the maximum load capacity of 875.120 kN, vertical deformation is 20.600 mm. The right-front vertical member of the first layer is severely deformed, and the screw jacks show inclinations resulting from severe deformation of vertical members. Figure 17 shows the failure mode of the scaffolds.

The maximum load capacities of second loading of tests A and B are 565.270 kN and 720.106 kN, respectively, and the corresponding vertical deformations are 15.283 mm and 27.163 mm. The failure modes resemble those observed under the first loading. Figure 16 shows the similar P-Δ curves observed under the first and second loadings.

The above tests of the two-layer scaffolds with 56 cm difference in ground elevation under the first loading showed that the average maximum load capacity is 890.252 kN and that the average corresponding vertical deformation is 20.944 mm. The average maximum load capacity in the second loading is 642.688 kN, and the corresponding average vertical deformation is 21.223 mm. The load capacity of the scaffolds in the second loading is 72% (=642.688/890.252) of that in the first loading.

Comparing with the average maximum load capacity of the two-layer basic setup scaffolds (907.346 kN), the average maximum load capacity of the two-layer scaffolds with 56 cm difference in ground elevation (890.252 kN) is 98% (=890.252/907.346) of that of the basic setup. Therefore, when the screw jacks are extended to 76 cm on one side, the effect of the 56 cm difference in ground elevation on the load capacity of isolated heavy-duty scaffolds is negligible.

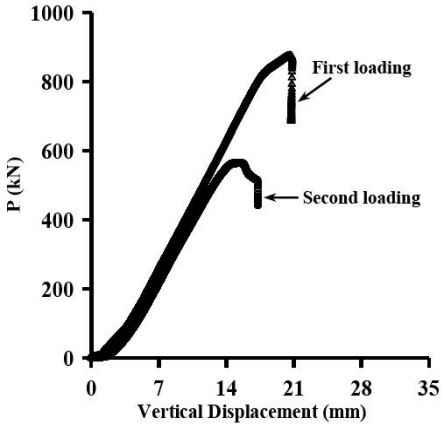

Figure 16. P-Δ Curves of Two-layer Setup with 56 cm Difference in Ground Elevation under the First and Second Loadings in Test A

Figure 17. Failure Mode of Two-layer Setup with 56 cm Difference in Ground Elevation

4.4 Top Difference in Elevation

The tests were performed in two groups (A and B). Table 1 shows the test results. The maximum load capacities for groups A and B under the first loading are 998.337 kN and 883.406 kN, respectively, and the corresponding vertical deformations are 21.475 mm and 20.319 mm.

Figure 18 shows the P-Δ curves obtained in test A of the first and second loadings on scaffolds with 56 cm top difference in elevation. The maximum value of load capacity is 998.337 kN, and the corresponding vertical deformation is 21.475 mm. The left-rear vertical member of the first layer and the right-rear vertical member of the second layer are severely deformed, and the screw jacks

show an inclination resulting from severe deformation of vertical members. Figure 19 shows the failure mode of the scaffolds.

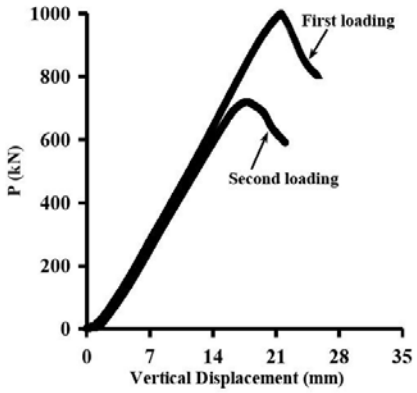

Figure 18. P-Δ Curves of Two-layer Setup with 56 cm Difference in Top Elevation under the First and Second Loadings in Test A

Figure 19. Failure Mode of Two-layer Setup with 56 cm Difference in Top Elevation

The maximum load capacities of second loading of tests A and B are 720.458 kN and 496.046 kN, respectively, and the corresponding vertical deformations are 17.500 mm and 15.987 mm. Again the failure modes resemble those obtained in the first loading. Figure 18 shows the similar P-Δ curves obtained in the first and second loadings.

The above tests showed that, under the first loading, the two-layer scaffolds with 56 cm top difference in elevation had an average maximum load capacity of 940.872 kN and an average corresponding vertical deformation of 20.897 mm. Under the second loading, the average maximum load capacity is 608.252 kN, which is 65% (=608.252/940.872) of that under first loading, and the average corresponding vertical deformation is 16.744 mm.

Comparing with the average maximum load capacity of the two-layer basic setup scaffolds (907.346 kN), the average maximum load capacity of the two-layer scaffolds with 56 cm top difference in elevation (940.872 kN) is 104% (=940.872/907.346) of that of the basic setup. This

result can be attributed to the test error. This infers that when the top screw jacks are extended to 76 cm on one side, the effect of 56 cm top difference in elevation has a negligible effect on the load capacity of the isolated heavy-duty scaffolds.

4.5 Extension of Top Screw Jacks

This case included four tests (A, B, C and D). The maximum load capacities observed in four tests under first loading are 912.533 kN, 846.912 kN, 780.047 kN and 824.617 kN, respectively, and the corresponding vertical deformations are 22.338 mm, 21.425 mm, 24.463 mm and 21.338 mm. Table 1 shows the test results.

Figure 20 shows the P-Δ curves of the first and second loadings on scaffolds with top screw jacks extended in test A. The curve for the first loading shows that the load and deformation relationship increases linearly. At the maximum load of 912.533 kN, the corresponding vertical deformation is 22.338 mm. The two vertical members on the rear row of the first layer deform severely, and the screw jacks show an inclination resulting from severe deformation of the vertical members. Figure 21 shows the failure mode of the scaffolds.

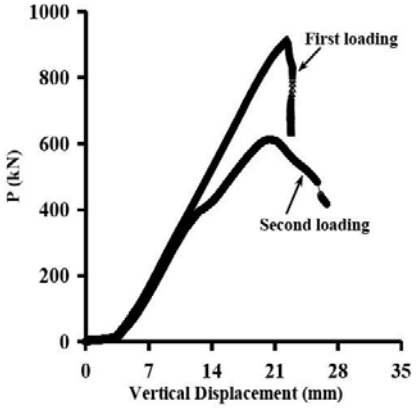

Figure 20. P-Δ Curves of Two-layer Setup with Extension of Top Screw Jacks under the First and Second Loadings in Test A

Figure 21. Failure Mode of Two-layer Setup with Extension of Top Screw Jacks

The maximum load capacities of second loading of tests A, B, C and D are 613.863 kN, 530.194 kN, 490.530 kN and 609.762 kN, respectively, and the corresponding vertical deformations are 20.419 mm, 19.288 mm, 24.213 mm and 17.775 mm. Basically, the failure modes are similar to those obtained in the first loading. Figure 20 shows the similar P-Δ curves obtained under the first and second loadings.

The above tests show that the average maximum load capacity of the two-layer scaffolds with top screw jacks extended in the first loading is 841.027 kN, and the average corresponding vertical deformation is 22.391 mm. The average maximum load capacity in the second loading is 561.087 kN, and the average corresponding vertical deformation is 20.424 mm. The load capacity of the scaffolds in the second loading is 67% (=561.087/841.027) of that in the first loading.

Comparing with the average maximum load capacity of the two-layer basic setup scaffolds (907.346 kN), the average maximum load capacity of the two-layer scaffolds with top screw jacks extended (841.027 kN) is 93% (=841.027/907.346) of that of the basic setup. This implies that extending the top screw jacks of isolated heavy-duty scaffolds to 75 cm has a negligible effect on the load capacity of the isolated heavy-duty scaffolds.

4.6 Extension of Both Top and Base Screw Jacks

For the five tests in this case (A, B, C, D and E), the maximum load capacities under the first loading are 813.937 kN, 878.900 kN, 963.234 kN, 672.834 kN and 849.996 kN, respectively, and the corresponding vertical deformations are 21.700 mm, 21.538 mm, 23.663 mm, 20.006 mm and 21.750 mm. Table 1 shows the test results.

Figure 22 shows the P-Δ curves obtained in test A of scaffolds with both top and base screw jacks extended under the first and second loadings. The curve for the first loading shows that the correlation between load and deformation increases linearly after loading. When the load increases to the maximum value of 813.937 kN, vertical deformation is 21.700 mm. The failure mode shows that the deformations occur at the connection joints between the top/base screw jacks and the vertical members of the scaffolds. The deformation of the scaffolds unit is comparatively smaller than that of two screw jacks.Figure 23 shows the failure mode of the scaffolds.

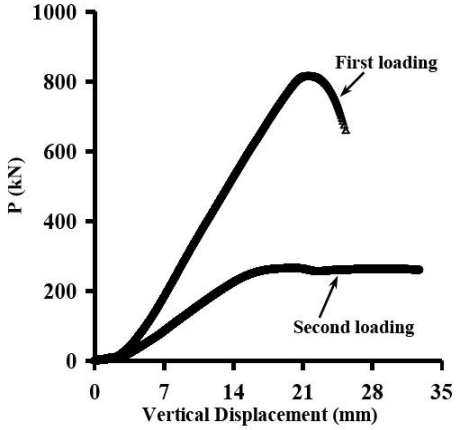

Figure 22. P-Δ Curves of Two-layer Setup with Extensions of Both Top and Base Screw Jacks under the First and Second Loadings in Test A

Figure 23. Failure Mode of Two-layer Setup with Extensions of Both Top and Base Screw Jacks

The maximum load capacities of second loading of groups A, B, C, D and E tests are 266.141 kN, 365.079 kN, 212.806 kN, 370.881 kN and 298.410 kN, respectively, and the corresponding vertical deformations are 20.125 mm, 22.000 mm, 28.913 mm, 15.537 mm and 18.881 mm. The failure modes observed under the second loading generally resemble those under the first loading. However, Figure 22 shows that the P-Δ curve under the second loading differs from that under the first one. Because the deformation of the scaffolds after the first loading was comparatively more obvious, this led to a bigger initial imperfection of the scaffolds under the second loading than that of other test configurations.

The above tests of the two-layer scaffolds with both top and base screw jacks extended showed that average maximum load capacity in the first loading is 835.780 kN and that the average corresponding vertical deformation is 21.731 mm. The average maximum load capacity in the second loading is 302.663 kN, and the average corresponding vertical deformation is 21.091 mm. The load capacity of the scaffolds in the second loading is 36% (=302.663/835.780) of the load capacity in the first loading. As shown above, the decrease of the load capacity is substantial. This is due to that serious deformations occur at the connecting joints between the top/base screw jacks and the vertical members of the scaffolds, which led to serious inclination of the scaffolds before being put under the second loading (Figure 24).

The comparisons showed that the average maximum load capacity in two-layer scaffolds with both top and base screw jacks extended (835.780 kN) is 92% (=835.780/907.346) of that in two-layer basic setup scaffolds (907.346 kN). The extension of both the top and base screw jacks seems to have a negligible effect on the load capacity of isolated heavy-duty scaffolds.

However, comparison between the poorer load capacity obtained in test D (672.834 kN) and the average maximum load capacity of the two-layer basic setup scaffolds (907.346 kN) shows that the load capacity of test D approximates 74% (=672.834/907.346) that of the basic setup, which represents a 26% decrease in the load capacity of the basic setup. In addition, the failure modes revealed deformations at the connecting joints between the top/base screw jacks and the vertical members of the scaffolds. This failure style is different from that of other scaffold setups, of which the deformations usually occur on the scaffolds unit. Scaffold setups with both top and base screw jacks extended should be used cautiously in construction sites.

Figure 24. Failure at Connecting Joints between Top Screw Jacks and Vertical Members Observed in Test of Extension of Both Top and Base Screw Jacks

4.7 Steel Tube Shores without Enclosed Restraint on Top of Scaffolds

Under the first loading, tests A and B in this case revealed the maximum load capacities of 231.210 kN and 234.283 kN, respectively, and the corresponding vertical deformations of 47.689 mm and 45.114 mm. Table 1 shows the test results.

Figure 25 shows the P-Δ curve obtained in test A of the two-layer isolated heavy-duty scaffolds reinforced with steel tube shores without an enclosed restraint on the top. The curve in the figure shows that the load and deformation relationship increases linearly after loading. When the load is increased to 113.659 kN, an up-and-down movement of the curve results from a tilt in the four steel tube shores on top of the isolated heavy-duty scaffolds. The maximum load capacity of the two-layer isolated heavy-duty scaffolds is 231.211 kN, and the corresponding vertical deformation is 47.689 mm.

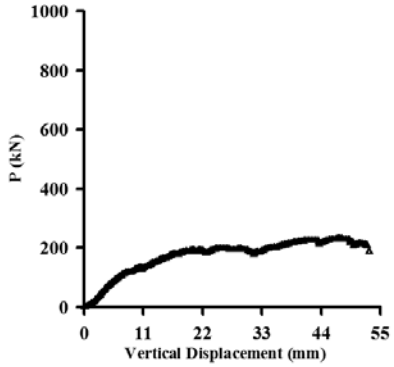

Figure 25. P-Δ Curve of Two-layer Setup Reinforced with Steel Tube Shores without Enclosed Restraint on the Top in Test A

The test configuration with steel tube shores added without an enclosed restraint on top of the isolated heavy-duty scaffolds is a combined setup involving two different materials, which is unlike the setups mentioned above. When failure occurred, the steel tube shores without enclosed restraint on top of the scaffolds became tilted. During loading, both ends of the top steel tube shores were somewhat damaged by the simple style screw jacks. The deformation of the isolated heavy-duty scaffold unit was comparatively less than that of steel tube shores. Figure 26 shows the failure mode of the scaffolds. Similar failure modes were observed in tests A and B. The extreme failure of the 4 steel tube shores on the upper layer precluded readjustment and restoration of the original position of the scaffolds. Therefore, the second loading was not performed.

The above tests of two-layer scaffolds reinforced with steel tube shores without enclosed restraint showed an average maximum load capacity of 232.747 kN and an average corresponding vertical deformation of 46.402 mm. The average maximum load capacity in the two-layer scaffolds reinforced with steel tube shores without enclosed restraint on the top (232.747 kN) is 26%(=232.747/907.346) of that in the two-layer basic setup scaffolds (907.346 kN). The load capacity decreases by 74%.Further comparisons showed that the average maximum load capacity of the two-layer scaffolds reinforced with steel tube shores without enclosed restraint on the top (232.747 kN) was only 28% (=232.747/841.617) of that of two-layer heavy-duty scaffolds with top screw jacks extended (841.027 kN). This result shows that when steel tube shores without enclosed restraint are added on top of the isolated heavy-duty scaffolds, the load capacity of the scaffold system will be seriously reduced.

Figure 26. Failure Mode of Two-layer Setup Reinforced with Steel Tube Shores without Enclosed Restraint

4.8 Steel Tube Shores with Enclosed Restraint on Top of Scaffolds

In the two tests in this case (A and B), the maximum load capacities obtained under the first loading are 220.610 kN and 207.607 kN, respectively, and the corresponding vertical deformations are 23.836 mm and 28.651 mm. Table 1 shows the test results.

Figure 27 shows the P-Δ curve obtained in test A of two-layer isolated heavy-duty scaffolds reinforced with steel tube shores with enclosed restraint on the top. When failure occurred, the maximum load was 220.610 kN, and the corresponding vertical deformation was 23.836 mm. Additionally, the four steel tube shores on the top of the isolated heavy-duty scaffolds tilted

simultaneously, and both ends of these top steel tube shores were somewhat damaged by the simple style screw jacks. The deformation was less severe in the isolated heavy-duty scaffolds than in the steel tube shores. Figure 28 shows the failure mode of the scaffolds.

In the two-layer scaffolds reinforced with steel tube shores with enclosed restraint on the top, this study shows that the average maximum load capacity is 214.10 kN and the average corresponding vertical deformation is 26.244 mm. Comparing with the average maximum load capacity of the two-layer heavy-duty scaffolds with top screw jacks extended (841.027 kN), the average maximum load capacity of the two-layer scaffolds reinforced with steel tube shores with enclosed restraint on the top is 25%(=214.108/841.617) of that of the scaffolds with top screw jacks extended. This result shows that the load capacity of the scaffolds reinforced with steel tube shores *with* enclosed restraint is slightly lower than that of the scaffolds reinforced with steel tube shores *without* enclosed restraint. Because one of the four steel tube shores is tilted, the other 3 shores are pulled together due to the enclosed restraint. Therefore, the load capacity of the scaffolds reinforced with four steel tube shores *with* enclosed restraint is slightly lower than that of the scaffolds reinforced with four steel tube shores *without* enclosed restraint.

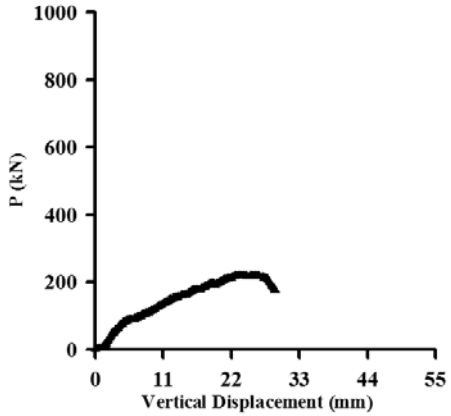

Figure 27. P-Δ Curve of Two-layer Setup Reinforced with Steel Tube Shores with Enclosed Restraint on the Top in Test A

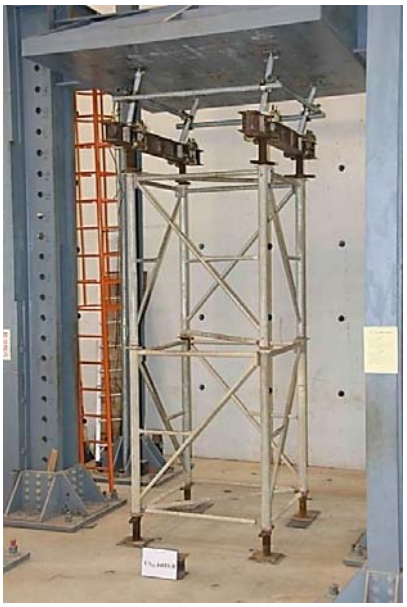

Figure 28. Failure Mode of Two-layer Setup Reinforced with Steel Tube Shores with Enclosed Restraint

5. COMPARISON OF CRITICAL LOADS OF ISOLATED HEAVY-DUTY SCAFFOLDS

5.1 Comparison of Different Scaffold Setups

The critical loads of various test configurations of the two-layer isolated heavy-duty scaffolds were compared based on that of the basic setup of two-layer isolated heavy-duty scaffolds. Figure 29 shows the comparison results. Comparison with the basic setup showed that the critical load of scaffolds with non-stiffness base screw jacks is 95% of that of scaffolds in the basic setup. Thus, the bending moment stiffness provided by the base screw jacks of the scaffolds is negligible.

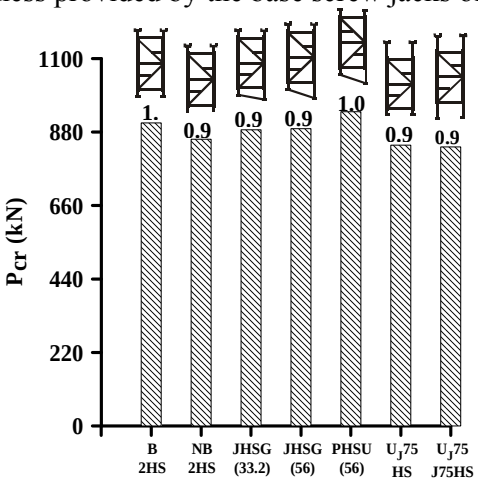

Figure 29. Comparison of Critical Loads of Isolated Heavy-duty Scaffolds in Various Configurations

The critical load of the scaffolds with 33.2 cm difference in ground elevation is 98% of that of scaffolds in the basic setup. The critical load of the scaffolds with 56 cm difference in ground elevation is also approximately 98% of that of scaffolds in the basic setup. Therefore, extending the base screw jacks of the scaffolds with difference in ground elevation on one side has a negligible effect on the critical load of the isolated heavy-duty scaffolds.

The comparisons showed that the critical load of scaffolds with 56 cm top difference in elevation is 104% of that of scaffolds in the basic setup. This difference is likely a result of test error. However, it is also the possible error that the scaffolding structure was put upside down to simulate the top difference in elevation of the scaffolds on the ground. Essentially, in scaffolds with top difference in elevation in this study, the extension of the top screw jacks on only one side has insignificant effect on the critical load of the isolated heavy-duty scaffolds.

The comparisons showed that the critical load of scaffolds with top screw jacks extended to 75 cm is 93% of that of scaffolds in the basic setup, and the critical load of the scaffolds with both top and base screw jacks extended to 75 cm is 92% of that in scaffolds in the basic setup. The test results for these configurations in this study show that extending the screw jacks of the scaffolds has a negligible effect on the critical load of isolated heavy-duty scaffolds.

However, when both top and base screw jacks of the scaffolds are extended to 75 cm, one test revealed only 74% of load capacity of the basic setup. As observed in failure mode, the deformation occurred at the connecting joints between the extended top/base screw jacks and the vertical members of the scaffolds. Therefore, contractors and designers must confirm the quality of the top and base screw jacks before applying this configuration.

5.2 Scaffolds with Different Top Shoring Configurations

Figure 30 shows the effect of different top steel tube shores configurations on scaffold load capacity. As shown in the comparison in the previous section, the test value of the scaffolds with top screw jacks extended to 75 cm approximated 93% that observed in the basic setup.

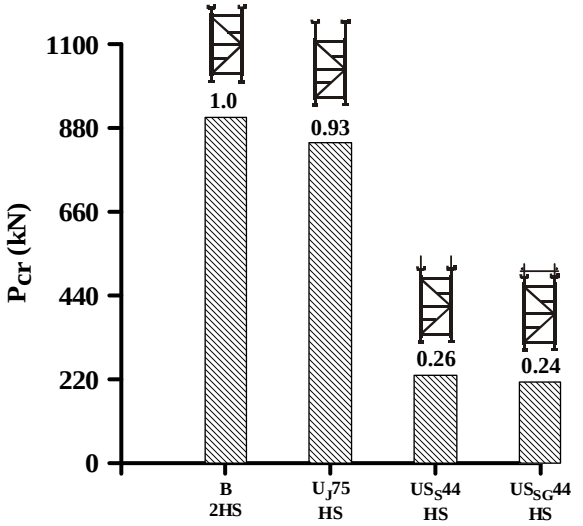

Figure 30. Comparison of Load Capacities of Isolated Heavy-duty Scaffolds in Different Top Steel Tube Shores Configurations

The test value of the isolated heavy-duty scaffolds with four steel tube shores (44 cm) *without* enclosed restraint on the top approximated 26% of that of the basic setup scaffolds. The test value of the isolated heavy-duty scaffolds with four steel tube shores (44 cm) *with* enclosed restraint on the top approximated 24% of that of the basic setup scaffolds. As indicated above, four steel tube shores (44 cm) added to the top of the isolated heavy-duty scaffolds substantially affected the load capacity of the isolated heavy-duty scaffolds.

In the case of four steel tube shores with enclosed restraint added to the top of isolated heavy-duty scaffolds, the failure of any one of the four steel tube shores under loading affected the other three shores. Since this phenomenon causes the failure of the entire scaffolding structure, it reduces the load capacity of the isolated heavy-duty scaffolds. Therefore, when using combined scaffold setups on construction sites, reinforcing the four steel tube shores with horizontal enclosed restraints is not advised.

As shown in the tests of the scaffolds with various top shoring configurations in Figure 30, the scaffolds with extended top screw jacks had the highest load capacity. Therefore, if the height of the isolated heavy-duty scaffolds must be extended, simply extending the top screw jacks is better than using the combined setup by adding steel tube shores on top of the scaffolds, which is usually used in the construction sites. Although extension of the top screw jacks reduces the risk of collapse of isolated heavy-duty scaffolds, excessive elongation of top screw jacks can cause a local failure of the screw jacks.

In addition, Table 1 shows that the vertical deformations of various setups of isolated heavy duty scaffolds were about 2 cm when the failure loads reached. The vertical deformation increases when the stories of the isolated heavy duty scaffolds are added. This vertical deformation needs to be considered especially during grouting concrete when the precision of the beams and slabs is required.

6. LOWER STRENGTH BOUND OF REUSABLE SCAFFOLDS

After observing the results of the first loading in the above tests, the scaffolds were unloaded, readjusted and put under the second loading. The test results for the second loading were considered the lower strength bound of reusable scaffolds. The strength reduction in the reusable isolated heavy-duty scaffolds was calculated by dividing the maximum load capacity of the second loading by that of the first loading is (Table 2).

Figure 31 shows the distribution of 1- to 3-fold standard deviations in the load capacity of reusable isolated heavy-duty scaffolds. The mean value of the reduction factor μ is 0.629, and the standard deviation σ is 0.113. Considering the lower limit of the load capacity, the reduction factor 0.516 is obtained by subtracting a 1-fold standard deviation from the mean value of reusable scaffolds (μ-σ). The reduction factor 0.403 is obtained by subtracting a 2-fold standard deviation (μ-2σ), and the reduction factor 0.29 is obtained by subtracting a 3-fold standard deviation (μ-3σ). When using the reusable isolated heavy-duty scaffolds to assemble temporary structures, the designers may choose an appropriate reduction factor to obtain a structural design consistent with the safety requirement.

Table 2. Ratios of Various Lower Strength Bounds of Reusable Isolated Heavy-duty Scaffolds

Type	Difference in elevation	Test group	Average values (kN)		2nd loading/ 1st loading	Average value	Standard deviation
			1st loading, capacity	2nd loading, capacity			
Two-layer basic setup	△h =0	A	894.003	288.316	0.323	0.629	0.113
		B	920.688	653.534	0.710		
Two-layer basic setup with non-stiffened base screw jacks	△h =0	A	762.584	382.272	0.501		
		B	912.560	577.229	0.633		
		C	899.974	623.155	0.692		
Difference in ground elevation	△h =33.2	A	911.671	515.991	0.566		
		B	862.262	539.247	0.625		
	△h =56	A	875.120	565.270	0.646		
		B	905.383	720.106	0.795		
Top difference in elevation	△h =56	A	998.337	720.458	0.722		
		B	883.406	496.046	0.562		
Extension of top screw jacks	△h =0	A	912.533	613.863	0.673		
		B	846.912	530.194	0.626		
		C	780.047	490.530	0.629		
		D	824.617	609.762	0.739		

Notes:
Average value: $\bar{x} = \sum_{i=1}^{n} x_i / n$; Standard deviation: $\sigma = \sqrt{\frac{\sum (x - \bar{x})^2}{(n-1)}}$

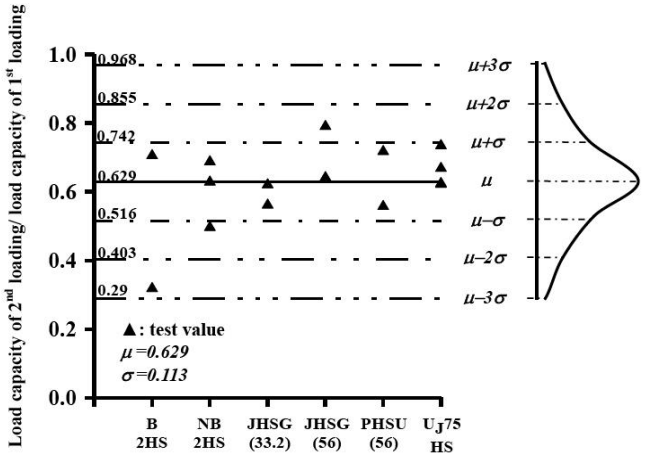

Figure 31. Distribution of 1- to 3-fold Standard Deviations in Load Capacities of Various Reusable Isolated Heavy-duty Scaffolds

7. CONCLUSIONS

The isolated heavy-duty scaffolds, which have high load capacity, are often used as the falsework during the construction stage of structures with high clearance, large spans and thick slabs, such as factory buildings, warehouses or gymnasiums. This study explores the critical loads and failure modes of isolated heavy-duty scaffolds in various setups by testing these scaffold configurations actually used on construction sites. The results of the tests are summarized as follows.

Since the bending moment stiffness provided by the base screw jacks of isolated heavy-duty scaffolds is negligible, the base has limited effect on the overall load capacity of isolated heavy-duty scaffolds. When isolated heavy-duty scaffolds are set up on ground with varying elevation or under an inclined top slab with varying elevation, their load capacity is not substantially affected as long as the difference in elevation is less than 56 cm. In a modular structure, the total height of multiple-layer isolated heavy-duty scaffolds is often insufficient to reach the interior ceiling of a construction structure, which leaves a gap between the top of the scaffolds and the slab of the construction structure. On construction sites, the gap is typically filled by adding steel tube shores on the top of the isolated heavy-duty scaffolds. However, the load capacity of the combined scaffolding structure is only 30% of that of the isolated heavy-duty scaffolds. In other words, this combined setup causes about 70% reductions in the load capacity of these scaffolds. Instead of the combined scaffolding structure, it is advisable to directly extend the top screw jacks of the isolated heavy-duty scaffolds to fill the gap between the top of the scaffolds and the slab. The load capacity of isolated heavy-duty scaffolds assembled from a single material is much higher than that of the scaffolds composed of other materials. For the strength design of the reusable isolated heavy-duty scaffolds, the reduction factors presented in this study can be used as reference. Designers can consider appropriate reduction factors to design reusable isolated heavy-duty scaffolds with various setups based on construction safety considerations. The vertical deformation of the isolated heavy duty scaffolding systems in tests of this study is about 2 cm. The value of the vertical deformation can be considered an index to evaluate the displacement of the beams and slabs after grouting concrete.

ACKNOWLEDGEMENTS

The authors would like to thank the National Science Council, Taiwan, R.O.C., for funding this study (Project number: NSC 101-2221-E-224-055 and NSC98-2923-E-002-005-MY3). T. Y.Hua Construction Ltd. is appreciated for providing test materials and partial funding. The authors also gratefully acknowledge Mr. Zhi-Wei Kuo for performing tests and data sorting in this study.

REFERENCE

[1] Weesner, L.B. and Jones, H.L., “Experimental and Analytical Capacity of Frame Scaffolding”, Engineering Structures, 2001, Vol. 23, No. 6, pp. 592-599.

[2] Yu, W.K., “An Investigation into Structural Behaviour of Modular Steel Scaffolds”, Steel and Composite Structures, 2004, Vol. 4, No. 3, pp. 211-226.

[3] Yu, W.K. and Chung K.F., “Prediction on Load Carrying Capacities of Multi-storey Door-type Modular Steel Scaffolds”, Steel and Composite Structures, 2004a, Vol. 4, No. 6, pp. 471-487.

[4] Yu, W.K., Chung, K.F. and Chan, S.L., “Structural Instability of Multi-storey Door-type Modular Steel Scaffolds,” Engineering Structures, 2004b, Vol. 26, pp. 867-881.

[5] Huang, Y.L., Chen, H.J., Rosowsky, D.V. and Kao, Y.G., "Load-carrying Capacities and Failure Modes of Scaffolding Shoring Systems, Part I: Modeling and Experiments", Structural Engineering and Mechanics, 2000a, Vol. 10, No. 1, pp. 57-79.
[6] Huang, Y.L., Kao, Y.G. and Rosowsky, D.V., "Load-carrying Capacities and Failure Modes of Scaffolding Shoring Systems, Part II: Analytical Model and its Closed-form Solution", Structural Engineering and Mechanics, 2000b, Vol. 10, No. 1, pp. 53-66.
[7] Peng, J.L., Pan, A.D., Rosowsky, D.V., Chen, W.F., Yen, T. and Chan, S.L., "High Clearance Scaffold Systems during Construction – I. Structural Modelling and Modes of Failure", Engineering Structures, 1996a, Vol. 18, No. 3, pp. 247-257.
[8] Peng, J.L., Rosowsky, D.V., Pan, A.D., Chen, W.F., Chan, S.L. and Yen, T., "High Clearance Scaffold Systems during Construction - II. Structural Analysis and Development of Design Guidelines," Engineering Structures, 1996b, Vol. 18, No. 3, pp. 258-267.
[9] Peng, J.L., Pan, A.D.E., Chen, W.F., Yen, T., and Chan, S.L., "Structural Modeling and Analysis of Modular Falsework Systems", Journal of Structural Engineering, ASCE, 1997, Vol. 123, No. 9, pp. 1245-1251.
[10] Peng, J.L., Pan, A.D.E., and Chan, S.L., "Simplified Models for Analysis and Design of Modular Falsework," Journal of Constructional Steel Research (Special Issue on Nonlinear Behaviour and Design of Steel Frames and Members), 1998, Vol. 48, No. 2/3, pp. 189-209.
[11] Peng, J.L., Pan, A.D.E. and Chen, W.F., "Approximate Analysis Method for Modular Tubular Falsework," Journal of Structural Engineering, ASCE, 2001, Vol. 127, No. 3, pp. 256-263.
[12] Kuo, C.C., Peng, J.L., Yen, T. and Chan, S.L., "Experimental Study of Modular Falsework System with Wooden Shores under Various Path Loads", Advances in Structural Engineering, 2008, Vol. 11, No. 4, pp. 369-382.
[13] Peng, J.L., Chan, S.L. and Wu, C.L., "Effects of Geometrical Shape and Incremental Loads on Scaffold Systems", Journal of Constructional Steel Research, 2007, Vol. 63, Issue 4, pp.448-459.
[14] Peng, J.L., Chen, K.H., Chan, S.L. and Chen, W.T., "Experimental and Analytical Investigations of Scaffolds with Anchor Rod and Plank", International Journal of Structural Stability and Dynamics, 2009a, Vol. 9, Issue 2, pp. 307-332.
[15] Peng, J.L., Chen, K.H., Chan, S.L. and Chen, W.T., "Experimental and Analytical Studies on Steel Scaffolds under Eccentric Loads", Journal of Constructional Steel Research, 2009b, Vol. 65, Issue 2, pp.422-435.
[16] Liu, H., Zhao, Q., Wang, X., Zhou, T., Wang, D., Liu, J. and Chen, Z., "Experimental and Analytical Studies on the Stability of Structural Steel Tube and Couple Scaffolds without X-bracing", Engineering Structures, 2010, Vol. 32, pp. 1003-1015.
[17] Peng, J.L., Yen,T., Kuo, C.C., and Chan, S.L., "Analytical and Experimental Bearing Capacities of System Scaffolds", Journal of Zhejiang University Science A, 2009c, Vol. 10, No. 1, pp. 82-92.
[18] Zhang, H., Chandrangsu, T. and Rasmussen, K.J.R., "Probabilistic Study of the Strength of Steel Scaffold Systems," Structural Safety, 2010, Vol. 32, pp. 393–401.
[19] Zhang, H., Rasmussen, K.J.R., and Ellingwood, B.R., "Reliability Assessment of Steel Scaffold Shoring Structure for Concrete Formwork", Engineering Structures, 2012, Vol. 36, pp.81–89.

SIDESWAY MAGNIFICATION FACTORS FOR STEEL MOMENT FRAMES WITH VARIOUS TYPES OF COLUMN BASES

J. Kent Hsiao

Associate Professor, Department of Civil and Environmental Engineering, Southern Illinois University Carbondale, Carbondale, IL, USA
E-mail: hsiao@engr.siu.edu

Received: 26 June 2012; Revised: 12 July 2013; Accepted: 17 July 2013

ABSTRACT: The sidesway magnification factor was introduced to the design of columns in moment frames subjected to the P-Δ effect. Three approaches for the computation of the sidesway magnification factor, namely, the column-lateral-buckling-strength approach, the story-lateral-stiffness approach, and the modified-story-lateral-stiffness approach, were suggested by the 2005 AISC Specification for Structural Steel Buildings, the ASCE/SEI 7-10 Minimum Design Loads for Buildings and Other Structures, and the 2010 AISC Specification for Structural Steel Buildings, respectively. This paper evaluates the sidesway magnification factors derived from the aforementioned three approaches for four different column base conditions, namely, ideal fixed-, ideal pinned-, practical fixed-, and practical pinned-base conditions. The results of the study conducted in this paper are that (1) if only the flexural deflections are considered in the frame analysis, the sidesway magnification factor derived from the modified story-lateral-stiffness approach closely agrees with that derived from the column-lateral-buckling-strength approach and (2) if the flexural deflections, as well as the shear and axial deformations, are considered in the frame analysis, the sidesway magnification factor derived from the story-lateral-stiffness approach closely agrees with that derived from the column-lateral-buckling-strength approach.

Keywords: Deflection, Effective length, Lateral forces, Sidesway, Steel columns, Steel frames

1. INTRODUCTION

Many methods have been introduced to the P-Δ analysis of columns in moment frames. These methods include the amplification factor method, the direct method, the iterative method, the negative property fictitious member methods, and the second-order computer program method. The amplification factor method is a rapid, but very approximate method while the direct method gives accurate results for low- or medium-rise rigid frames [1]. Both the amplification factor method and the direct method are commonly used by structural engineers for the computation of the sidesway magnification factor for the design of columns in steel moment frames subjected to the P- Δ effect. The amplification factor method involves the computation of the lateral buckling strength of the columns in the story being considered; this method was suggested by the 2005 AISC Specification for Structural Steel Buildings [2]. The direct method involves the computation of the lateral stiffness of the story being considered; this method was suggested by the 2005 AISC Specification for Structural Steel Buildings, the ASCE/SEI 7-10 Minimum Design Loads for Buildings and Other Structures [3], and the 2010 AISC Specification for Structural Steel Buildings [4]. The following is a summary of the approaches for the computation of the sidesway magnification factor caused by the P-Δ effects suggested by the 2005 AISC, ASCE/SEI 7-10, and 2010 AISC, respectively.

The 2005 AISC Specification for Structural Steel Buildings suggests the following two approaches for the computation of the sidesway amplifier values (B_2) for the design of columns in moment frames subjected to the P-Δ effect:

$$B_2 = \frac{1}{1 - \frac{\alpha \sum P_{nt}}{\sum \frac{\pi^2 EI}{(K_2 L)^2}}} \geq 1 \quad (1)$$

$$B_2 = \frac{1}{1 - \frac{\alpha \sum P_{nt}}{R_M \frac{\sum HL}{\Delta_H}}} \geq 1 \quad (2)$$

where α = 1.00 for the Load and Resistance Factor Design (LRFD); $\sum P_{nt}$ = the total vertical load supported by the story; E = the modulus of elasticity of steel, 29,000 ksi (200 000 MPa); I = the moment of inertia in the plane of bending; K_2 = the effective length factor in the plane of bending, based on sidesway buckling; L = the story height; R_M = 0.85 for moment-frame systems; $\sum H$ = the story shear produced by the lateral forces used to compute Δ_H; and Δ_H = the first-order interstory drift resulting from lateral forces.

The first approach (Eq. 1) uses the same method as the aforementioned "amplification factor method," which involves the computation of the Euler load of the column [5] and the elastic story sidesway buckling resistance. The effective length factor (K_2) presented in Eq. 1 can be determined by using the "Alignment Chart-Sidesway Uninhibited (Moment Frame)" presented in the 2005 AISC Specification for Structural Steel Buildings. The second approach (Eq. 2) uses the same method as the aforementioned "direct method," which involves the elastic analysis of the first-order interstory drifts due to lateral forces [1,6].

The ASCE/SEI 7-10 Minimum Design Loads for Buildings and Other Structures suggests the following approach for the computation of the sidesway magnification factor for the design of columns in moment frames subjected to the P-Δ effect:

$$\text{magnification factor} = \frac{1}{1 - \frac{p_x}{\left(\frac{V_x h_{sx}}{\delta_{xe} - \delta_{(x-1)e}} \right)}} \quad (3)$$

where P_x = the total vertical design load at and above level x; V_x = the shear force acting between levels x and x-1; h_{sx} = the story height below level x; δ_{xe} = the displacement at level x by a first-order elastic analysis; and $\delta_{(x-1)e}$ = the displacement at level x-1 by a first-order elastic analysis.

This approach (Eq. 3) uses the same method as the aforementioned "direct method," which involves the computation of the first-order interstory drifts due to lateral forces. Note that the only difference between Eqs. 2 and 3 is that Eq. 2 considers the lateral stiffness modification coefficient, R_M, while Eq. 3 does not.

The 2010 AISC Specification for Structural Steel Buildings suggests the following approach (Eq. 4) for the computation of the sidesway amplifier value (B_2) for the design of columns in moment frames subjected to the P-Δ effect:

$$B_2 = \frac{1}{1 - \dfrac{\alpha P_{story}}{R_M \dfrac{HL}{\Delta_H}}} \geq 1 \qquad (4)$$

where α = 1.00 for the Load and Resistance Factor Design (LRFD); P_{story} = the total vertical load supported by the story; $R_M = 1 - 0.15\,(P_{mf}/P_{story})$; P_{mf} = the total vertical load in columns in the story that are part of moment frames; L = the story height; H = the story shear produced by the lateral forces used to compute Δ_H; and Δ_H = the first-order interstory drift resulting from lateral forces.

Note that for a building in which lateral stiffness is provided entirely by moment frames, $P_{mf} = P_{story}$, which in turn results in $R_M = 0.85$. Therefore, Eqs. 2 and 4 are identical.

2. EFFECTIVE LENGTH FACTORS FOR COLUMNS IN SWAY FRAMES

The effective length factor (K) for columns in a sway frame can be determined by using the alignment chart for uninhibited sidesway (presented in Chapter C – Stability Analysis and Design in the 2005 AISC Specification for Structural Steel Buildings) or by using the following equation [2]:

$$\frac{G_A G_B (\pi / K)^2 - 36}{6(G_A + G_B)} - \frac{(\pi/K)}{\tan(\pi / K)} = 0$$

where G = the restraint factor at the column end (the subscripts A and B refer to the joints at the top and bottom of the column being considered) = $\sum(I_c/L_c) / \sum(I_b/L_b)$

The approximate K value can be obtained by using the following equation [7]:

$$K = \sqrt{\frac{1.6 G_A G_B + 4.0(G_A + G_B) + 7.5}{G_A + G_B + 7.5}} \qquad (5)$$

For a column with a complete fixity at its base, $G_B = 0$, Eq. 5 becomes

$$K = \sqrt{\frac{4.0 G_A + 7.5}{G_A + 7.5}} \qquad (6)$$

For a column with a true friction-free pinned base, $G_B = \infty$, Eq. 5 becomes

$$K = \sqrt{1.6 G_A + 4.0} \qquad (7)$$

The 2005 AISC Specification, however, suggests that if the column end is rigidly attached to a properly designed footing, G_B may be taken as 1.0. Smaller values may be used if justified by analysis. The reader is referred to the AISC "Steel Design Guide 1 – Base Plate and Anchor Rod Design" [8] for the design of column base plates with moments. The AISC Specification also suggests that if the column base is not rigidly connected to a footing or foundation, G_B may be taken as 10 for practical designs. G_B is theoretically infinity if the column base is designed as a true friction-free pin.

3. STORY DRIFTS OF MOMENT FRAMES UNDER LATERAL LOADS

Referring to the frame shown in Figure 1, the column sizes are identical and both columns have a fixed base connection. The horizontal load, H, is acting at joint 1. Using the stiffness method, the following equation can be derived [9]:

$$\begin{bmatrix} 2(k_{1-3}+k_{1-2}) & k_{1-2} & 3k_{1-3} \\ k_{1-2} & 2(k_{1-2}+k_{2-4}) & 3k_{2-4} \\ 3k_{1-3} & 3k_{2-4} & 6(k_{1-3}+k_{2-4}) \end{bmatrix} \begin{bmatrix} \theta_1 \\ \theta_2 \\ -R \end{bmatrix} = \begin{bmatrix} 0 \\ 0 \\ HL_c \end{bmatrix} \tag{8}$$

where $k_{i-j} = 2E_{i-j}I_{i-j}/L_{i-j}$; θ_i = rotation at joint i; $R = \Delta_H/L_c$.

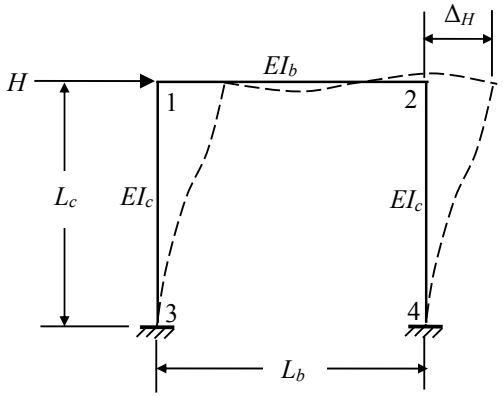

Notes:
I_c = moment of inertia of column
I_b = moment of inertia of beam
L_c = column length
L_b = beam length
E = modulus of elasticity, constant for all members
Δ_H = story drift resulting from lateral force H

Figure 1. Typical Moment Frame with Ideal Fixed-Base Connections

Since the sizes and lengths of the two columns are identical, $k_{1-3} = k_{2-4} = 2EI_c/L_c$. Setting $\lambda = (I_b/L_b) / (I_c/L_c)$, Eq. 8 can be rewritten as

$$\frac{2EI_c}{L_c}\begin{bmatrix} 2(\lambda+1) & \lambda & 3 \\ \lambda & 2(\lambda+1) & 3 \\ 3 & 3 & 12 \end{bmatrix} \begin{bmatrix} \theta_1 \\ \theta_2 \\ -R \end{bmatrix} = \begin{bmatrix} 0 \\ 0 \\ HL_c \end{bmatrix} \tag{9}$$

From Eq. 9,

$$R = \frac{HL_c^2}{8EI_c}\left(\frac{1}{3}+\frac{1}{6\lambda+1}\right)$$

Since $R = \Delta_H/L_c$,

$$\Delta_H = \frac{HL_c^3}{8EI_c}\left(\frac{1}{3}+\frac{1}{6\lambda+1}\right) \tag{10}$$

Eq. 10 is to be used for the computation of the story drift for the fixed-base frame loaded under a lateral force H, as shown in Figure 1. Note that this equation considers the flexural deflections of the members only. Axial and shear deformations of the members have been neglected.

Similar to the derivation of Eq. 8 from the moment frame with fixed-base connections shown in Figure 1, Eq. 11 can be derived from the moment frame with pinned-base connections shown in Figure 2:

$$\begin{bmatrix} 2k_{1-2}+1.5k_{1-3} & k_{1-2} & 1.5k_{1-3} \\ k_{1-2} & 2k_{1-2}+1.5k_{2-4} & 1.5k_{2-4} \\ 1.5k_{1-3} & 1.5k_{2-4} & 1.5(k_{1-3}+k_{2-4}) \end{bmatrix} \begin{bmatrix} \theta_1 \\ \theta_2 \\ -R \end{bmatrix} = \begin{bmatrix} 0 \\ 0 \\ HL_c \end{bmatrix} \tag{11}$$

where $k_{i-j} = 2E_{i-j}I_{i-j}/L_{i-j}$; θ_i = rotation at joint i; $R = \Delta_H/L_c$.

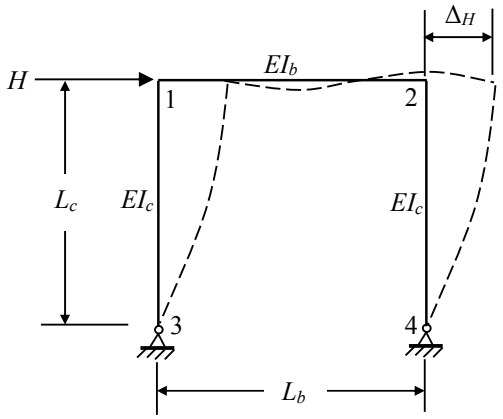

Notes:
I_c = moment of inertia of column
I_b = moment of inertia of beam
L_c = column length
L_b = beam length
E = modulus of elasticity, constant for all members
Δ_H = story drift resulting from lateral force H

Figure 2. Typical Moment Frame with Ideal Pinned-Base Connections

Since the sizes and lengths of the two columns are identical, $k_{1\text{-}3} = k_{2\text{-}4} = 2EI_c/L_c$. Setting $\lambda = (I_b/L_b) / (I_c/L_c)$, Eq. 11 can be rewritten as

$$\frac{2EI_c}{L_c}\begin{bmatrix} 2\lambda+1.5 & \lambda & 1.5 \\ \lambda & 2\lambda+1.5 & 1.5 \\ 1.5 & 1.5 & 3 \end{bmatrix} \begin{bmatrix} \theta_1 \\ \theta_2 \\ -R \end{bmatrix} = \begin{bmatrix} 0 \\ 0 \\ HL_c \end{bmatrix} \tag{12}$$

From Eq. 12,

$$R = \frac{HL_c^2}{6EI_c}\left(1+\frac{1}{2\lambda}\right)$$

Since $R = \Delta_H/L_c$,

$$\Delta_H = \frac{HL_c^3}{6EI_c}\left(1+\frac{1}{2\lambda}\right) \tag{13}$$

Eq. 13 is to be used for the computation of the story drift for the pinned-base frame loaded under a lateral force H, as shown in Figure 2. Also note that this equation considers the flexural deflections of the members only. Axial and shear deformations of the members have been neglected.

4. EFFECTIVE LENGTH AND DIRECT ANALYSIS METHODS

The 2010 AISC Specification addresses two major methods, the Effective Length and Direct Analysis Methods, for the calculation of the required strengths for the stability design of members and connections.

The Effective Length Method is valid so long as the ratio of second-order deflection to first-order deflection in all stories is equal to or less than 1.5 (that is: $B_2 = \Delta_{\text{second-order}}/\Delta_{\text{first-order}} \leq 1.5$).

The Direct Analysis Method has the advantage of not having to calculate the effective length factor, K. This means that in designing compression members, the effective length factor is taken as 1.0. To accomplish this the Specification requires that a reduced axial and flexural stiffness shall be used for all elements contributing to the lateral load resistance of the structure to account for the influence of inelasticity and residual stresses on second-order effects. Note that the computation of the first-order interstory drift, Δ_H, in $R_M \dfrac{\sum HL}{\Delta_H}$, and, $(\delta_{xe} - \delta_{(x-1)e})$, in $\dfrac{V_x h_{sx}}{\delta_{xe} - \delta_{(x-1)e}}$, respectively, in Section 5 uses the Effective Length Method. Therefore, the reduced axial and flexural stiffness in the members of the structure have been ignored.

However, the analysis using both methods shall consider flexural, shear and axial member deformations and all other component and connection deformations that contribute to displacements of the structure.

5. COMPARISON OF EQUATIONS 1, 2, AND 3

This section addresses the comparison of the $\sum \dfrac{\pi^2 EI}{(K_2 L)^2}$, $R_M \dfrac{\sum HL}{\Delta_H}$, and $\dfrac{V_x h_{sx}}{\delta_{xe} - \delta_{(x-1)e}}$ values in Eqs. 1, 2, and 3, respectively, for various column base conditions, which include the ideal fixed-base (a complete fixity, $G_B = 0$) condition, the ideal pinned-base (a true friction-free pin, $G_B = \infty$) condition, the practical fixed-base ($G_B = 1.0$) condition, and the practical pinned-base ($G_B = 10$) condition. In this paper, $(P_e)_1$, $(P_e)_2$, and $(P_e)_3$ represent the $\sum \dfrac{\pi^2 EI}{(K_2 L)^2}$, $R_M \dfrac{\sum HL}{\Delta_H}$, and $\dfrac{V_x h_{sx}}{\delta_{xe} - \delta_{(x-1)e}}$ values in Eqs. 1, 2, and 3, respectively.

5.1 Ideal Fixed-Base Condition ($G_B = 0$)

Consider the frame shown in Figure 3(a) for the condition where $G_A = (I_c/L_c) / (I_b/L_b) = 1.333$. From Eq. 6, one has $K_2 = 1.205$. Therefore, the $(P_e)_1$ value in Eq. 1 can be computed as

$$(P_e)_1 = 2\frac{\pi^2 EI_c}{(1.205L_c)^2} = 13.59\frac{EI_c}{L_c^2} = 13.59\frac{(29{,}000\,\text{ksi})(999\,\text{in.}^4)}{(180\,\text{in.})^2} = 12{,}150\ \text{kips}\ (54\,040\ \text{kN})$$

Note that the moment of inertia about the x-axis for W14×90, $I_x = 999$ in.^{4} (41 580 cm^4) [10].

Since $G_A = 1.333$, $\lambda = (I_b/L_b) / (I_c/L_c) = 1/G_A = 0.75$. From Eq. 10,

$$\Delta_H = \frac{HL_c^3}{8EI_c}\left(\frac{1}{3} + \frac{1}{4.5+1}\right) = 0.0644\left(\frac{HL_c^3}{EI_c}\right)$$

From which the $(P_e)_2$ value in Eq. 2 can be computed as

$$(P_e)_2 = R_M\frac{\sum HL_c}{\Delta_H} = 0.85\left[\frac{HL_c}{0.0644\left(\frac{HL_c^3}{EI_c}\right)}\right] = 13.2\frac{EI_c}{L_c^2} = 11{,}800\ \text{kips}\ (52\,490\ \text{kN})$$

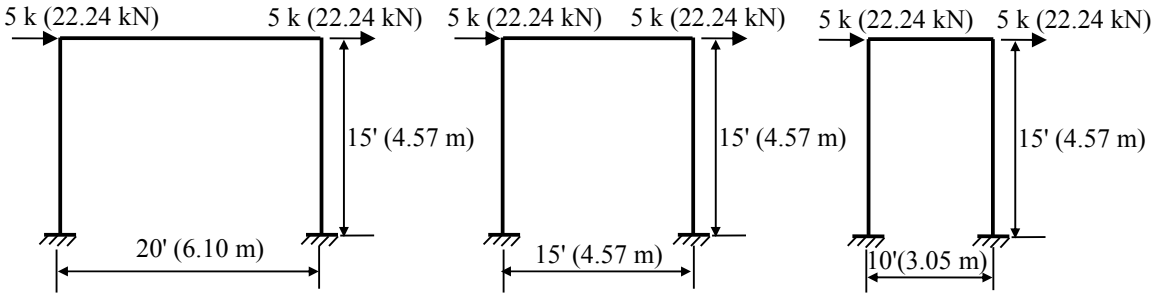

(a) $G_A = 1.333$ (b) $G_A = 1.0$ (c) $G_A = 0.6667$

Notes: (1) All members are W14×90.
(2) All members are bent about their x-axes due to the

Figure 3. Moment Frames with Ideal Fixed-Base Connections ($G_B = 0$)

Table 1 summarizes and compares the computed $(P_e)_1$ and $(P_e)_2$ values in Eqs. 1 and 2 for $G_A = 1.333$, 1, and 0.6667 for the laterally loaded frames shown in Figure 3 for ideal fixed-base connections ($G_B = 0$). The results shown in Table 1 indicate that the computed $(P_e)_1$ values for Eq. 1 closely agree with the computed $(P_e)_2$ values for Eq. 2. The differences between the $(P_e)_1$ and $(P_e)_2$ values vary from 1% for $G_A = 0.6667$ to 3% for $G_A = 1.333$. Note that the Δ_H values shown in Table 1 are derived from Eq. 10, which considers the flexural deflections of the members only. Axial and shear deformations of the members have been neglected.

Table 2 also summarizes and compares the computed $(P_e)_1$ and $(P_e)_2$ values in Eqs. 1 and 2 for $G_A = 1.333$, 1, and 0.6667 for the laterally loaded frames shown in Figure 3 for ideal fixed-base connections ($G_B = 0$). However, the Δ_H values shown in Table 2 are obtained by using the computer software SAP2000 [11], which considers the flexural deflections, as well as the axial and shear deformations, of the members. The results shown in Table 2 indicate that the computed $(P_e)_1$ values for Eq. 1 are all quite larger than the computed $(P_e)_2$ values for Eq. 2. The differences between the $(P_e)_1$ and $(P_e)_2$ values vary from 16% for $G_A = 1.333$ to 22% for $G_A = 0.6667$.

Table 1. Comparison of $(P_e)_1$ and $(P_e)_2$ for the Laterally Loaded Frames Shown in Figure 3 (Ideal fixed-base connections, $G_B = 0$)

Figure	G_A	K_2	$(P_e)_1$ [a]	Δ_H [b]	$(P_e)_2$ [c]	$(P_e)_1$ vs. $(P_e)_2$
3(a)	1.333	1.205	$13.59\frac{EI_c}{L_c^2}$ =12,150 kips (54 040 kN)	$\frac{HL_c^3}{8EI_c}\left(\frac{1}{3}+\frac{1}{5.5}\right)$ = 0.130 in. (0.330 cm)	$13.20\frac{EI_c}{L_c^2}$ =11,800 kips (52 490 kN)	$(P_e)_1 > (P_e)_2$ by 3%
3(b)	1.0	1.163	$14.59\frac{EI_c}{L_c^2}$ =13,050 kips (58 040 kN)	$\frac{HL_c^3}{8EI_c}\left(\frac{1}{3}+\frac{1}{7}\right)$ = 0.120 in. (0.305 cm)	$14.28\frac{EI_c}{L_c^2}$ =12,770 kips (56 800 kN)	$(P_e)_1 > (P_e)_2$ by 2%
3(c)	0.6667	1.116	$15.86\frac{EI_c}{L_c^2}$ =14,180 kips (63 070 kN)	$\frac{HL_c^3}{8EI_c}\left(\frac{1}{3}+\frac{1}{10}\right)$ = 0.109 in. (0.277 cm)	$15.69\frac{EI_c}{L_c^2}$ =14,030 kips (62 410 kN)	$(P_e)_1 > (P_e)_2$ by 1%

[a] $(P_e)_1 = \sum \frac{\pi^2 EI}{(K_2 L)^2}$ as shown in Eq. 1.

[b] Only the flexural deflections of the members are considered for the computation of Δ_H.

[c] $(P_e)_2 = R_M \frac{\sum HL}{\Delta_H}$ as shown in Eq. 2.

Table 2. Comparison of $(P_e)_1$ and $(P_e)_2$ for the Laterally Loaded Frames Shown in Figure 3 (Ideal fixed-base connections, $G_B = 0$)

Figure	G_A	K_2	$(P_e)_1$ [a]	Δ_H [b]	$(P_e)_2$ [c]	$(P_e)_1$ vs. $(P_e)_2$
3(a)	1.333	1.205	12,150 kips (54 040 kN)	0.146 in. (0.371 cm)	10,480 kips (46 620 kN)	$(P_e)_1 > (P_e)_2$ by 16 %
3(b)	1.0	1.163	13,050 kips (58 040 kN)	0.138 in. (0.351 cm)	11,090 kips (49 330 kN)	$(P_e)_1 > (P_e)_2$ by 18 %
3(c)	0.6667	1.116	14,180 kips (63 070 kN)	0.132 in. (0.335 cm)	11,590 kips (51 550 kN)	$(P_e)_1 > (P_e)_2$ by 22 %

[a] $(P_e)_1 = \sum \frac{\pi^2 EI}{(K_2 L)^2}$ as shown in Eq. 1.

[b] The flexural deflections, as well as the axial and shear deformations, are considered for the computation of Δ_H.

[c] $(P_e)_2 = R_M \frac{\sum HL}{\Delta_H}$ as shown in Eq. 2.

Table 3 summarizes and compares the computed $(P_e)_1$ and $(P_e)_3$ values in Eqs. 1 and 3 for $G_A = 1.333$, 1, and 0.6667 for the laterally loaded frames shown in Figure 3 for ideal fixed-base connections ($G_B = 0$). The $(\delta_{xe} - \delta_{(x-1)e})$ values shown in Table 3 are obtained by using the computer software SAP2000, which considers the flexural deflections, as well as the axial and shear deformations, of the members. The results shown in Table 3 indicate that the computed $(P_e)_1$ values for Eq. 1 closely agree with the computed $(P_e)_3$ values for Eq. 3. The differences between the $(P_e)_1$ and $(P_e)_3$ values are within 4%.

Table 3. Comparison of $(P_e)_1$ and $(P_e)_3$ for the Laterally Loaded Frames Shown in Figure 3 (Ideal fixed-base connections, $G_B = 0$)

Figure	G_A	K_2	$(P_e)_1$[a]	$(\delta_{xe} - \delta_{(x-1)e})$[b]	$(P_e)_3$[c]	$(P_e)_1$ vs. $(P_e)_3$
3(a)	1.333	1.205	12,150 kips (54 040 kN)	0.146 in. (0.371 cm)	12,330 kips (54 840 kN)	$(P_e)_1 < (P_e)_3$ by 1 %
3(b)	1.0	1.163	13,050 kips (58 040 kN)	0.138 in. (0.351 cm)	13,040 kips (58 000 kN)	$(P_e)_1 \approx (P_e)_3$
3(c)	0.6667	1.116	14,180 kips (63 070 kN)	0.132 in. (0.335 cm)	13,640 kips (60 670 kN)	$(P_e)_1 > (P_e)_3$ by 4 %

[a] $(P_e)_1 = \sum \frac{\pi^2 EI}{(K_2 L)^2}$ as shown in Eq. 1.

[b] The flexural deflections, as well as the axial and shear deformations, are considered for the computation of $(\delta_{xe} - \delta_{(x-1)e})$.

[c] $(P_e)_3 = \frac{V_x h_{sx}}{\delta_{xe} - \delta_{(x-1)e}}$ as shown in Eq. 3.

5.2 Ideal Pinned-Base Condition ($G_B = \infty$)

Table 4 summarizes and compares the computed $(P_e)_1$ and $(P_e)_2$ values in Eqs. 1 and 2 for $G_A = 1.333$, 1, and 0.6667 for the laterally loaded frames shown in Figure 4 for ideal pinned-base connections ($G_B = \infty$). The results shown in Table 4 indicate that the computed $(P_e)_1$ values for Eq. 1 closely agree with the computed $(P_e)_2$ values for Eq. 2. The differences between the values vary from 2% for $G_A = 0.6667$ to 5% for $G_A = 1.333$. Note that the computed Δ_H values shown in Table 4 are derived from Eq. 13, which considers the flexural deflections of the members only. Axial and shear deformations of the members have been neglected.

Table 4. Comparison of $(P_e)_1$ and $(P_e)_2$ for the Laterally Loaded Frames Shown in Figure 4 (Ideal pinned-base connections, $G_B = \infty$)

Figure	G_A	K_2	$(P_e)_1$[a]	Δ_H[b]	$(P_e)_2$[c]	$(P_e)_1$ vs. $(P_e)_2$
4(a)	1.333	2.477	$3.217\frac{EI_c}{L_c^2}$ =2,880 kips (12 810 kN)	$\frac{HL_c^3}{6EI_c}\left(1+\frac{1}{1.5}\right)$ = 0.559 in. (1.420 cm)	$3.060\frac{EI_c}{L_c^2}$ =2,740 kips (12 190 kN)	$(P_e)_1 > (P_e)_2$ by 5%
4(b)	1.0	2.366	$3.526\frac{EI_c}{L_c^2}$ =3,150 kips (14 010 kN)	$\frac{HL_c^3}{6EI_c}\left(1+\frac{1}{2}\right)$ = 0.503 in. (1.278 cm)	$3.400\frac{EI_c}{L_c^2}$ =3,040 kips (13 520 kN)	$(P_e)_1 > (P_e)_2$ by 4%
4(c)	0.6667	2.251	$3.896\frac{EI_c}{L_c^2}$ =3,480 kips (15 480 kN)	$\frac{HL_c^3}{6EI_c}\left(1+\frac{1}{3}\right)$ = 0.447 in. (1.135 cm)	$3.825\frac{EI_c}{L_c^2}$ =3,420 kips (15 210 kN)	$(P_e)_1 > (P_e)_2$ by 2%

[a] $(P_e)_1 = \sum \frac{\pi^2 EI}{(K_2 L)^2}$ as shown in Eq. 1.

[b] Only the flexural deflections of the members are considered for the computation of Δ_H.

[c] $(P_e)_2 = R_M \frac{\sum HL}{\Delta_H}$ as shown in Eq. 2.

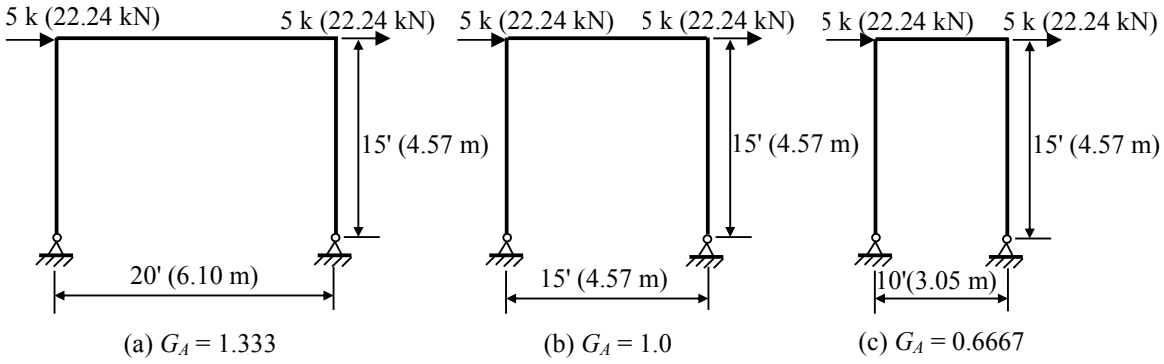

(a) $G_A = 1.333$ (b) $G_A = 1.0$ (c) $G_A = 0.6667$

Notes: (1) All members are W14×90.
(2) All members are bent about their x-axes due to the applied

Figure 4. Moment Frames with Ideal Pinned-Base Connections ($G_B = \infty$)

Table 5 also summarizes and compares the computed $(P_e)_1$ and $(P_e)_2$ values in Eqs. 1 and 2 for $G_A =$ 1.333, 1, and 0.6667 for the laterally loaded frames shown in Figure 4 for ideal pinned-base connections ($G_B = \infty$). However, the Δ_H values shown in Table 5 are obtained by using the computer software SAP2000, which considers the flexural deflections, as well as the axial and shear deformations, of the members. The results shown in Table 5 indicate that the computed $(P_e)_1$ values for Eq. 1 are all quite larger than the computed $(P_e)_2$ values for Eq. 2. The differences between the values vary from 12% for $G_A = 1.333$ to 16% for $G_A = 0.6667$.

Table 5. Comparison of $(P_e)_1$ and $(P_e)_2$ for the Laterally Loaded Frames Shown in Figure 4 (Ideal pinned-base connections, $G_B = \infty$)

Figure	G_A	K_2	$(P_e)_1$ [a]	Δ_H [b]	$(P_e)_2$ [c]	$(P_e)_1$ vs. $(P_e)_2$
4(a)	1.333	2.477	2,880 kips (12 810 kN)	0.595 in. (1.511 cm)	2,570 kips (11 430 kN)	$(P_e)_1 > (P_e)_2$ by 12 %
4(b)	1.0	2.366	3,150 kips (14 010 kN)	0.547 in. (1.389 cm)	2,800 kips (12 450 kN)	$(P_e)_1 > (P_e)_2$ by 13 %
4(c)	0.6667	2.251	3,480 kips (15 480 kN)	0.510 in. (1.295 cm)	3,000 kips (13 340 kN)	$(P_e)_1 > (P_e)_2$ by 16 %

[a] $(P_e)_1 = \sum \frac{\pi^2 EI}{(K_2 L)^2}$ as shown in Eq. 1.

[b] The flexural deflections, as well as the axial and shear deformations, are considered for the computation of Δ_H.

[c] $(P_e)_2 = R_M \frac{\sum HL}{\Delta_H}$ as shown in Eq. 2.

Table 6 summarizes and compares the computed $(P_e)_1$ and $(P_e)_3$ values in Eqs. 1 and 3 for $G_A = 1.333$, 1, and 0.6667 for the laterally loaded frames shown in Figure 4 for ideal pinned-base connections ($G_B = \infty$). The $(\delta_{xe} - \delta_{(x-1)e})$ values shown in Table 6 are obtained by using the computer software SAP2000, which considers the flexural deflections, as well as the axial and shear deformations, of the members. The results shown in Table 6 indicate that the computed $(P_e)_1$ values for Eq. 1 closely agree with the computed $(P_e)_3$ values for Eq. 3. The differences between the values vary from 1% for $G_A =$ 0.6667 to 5% for $G_A = 1.333$.

Table 6. Comparison of $(P_e)_1$ and $(P_e)_3$ for the Laterally Loaded Frames Shown in Figure 4 (Ideal pinned-base connections, $G_B = \infty$)

Figure	G_A	K_2	$(P_e)_1$ [a]	$(\delta_{xe} - \delta_{(x-1)e})$ [b]	$(P_e)_3$ [c]	$(P_e)_1$ vs. $(P_e)_3$
4(a)	1.333	2.477	2,880 kips (12 810 kN)	0.595 in. (1.511 cm)	3,030 kips (13 470 kN)	$(P_e)_1 < (P_e)_3$ by 5 %
4(b)	1.0	2.366	3,150 kips (14 010 kN)	0.547 in. (1.389 cm)	3,290 kips (14 630 kN)	$(P_e)_1 < (P_e)_3$ by 4 %
4(c)	0.6667	2.251	3,480 kips (15 480 kN)	0.510 in. (1.295 cm)	3,530 kips (15 700 kN)	$(P_e)_1 < (P_e)_3$ by 1 %

[a] $(P_e)_1 = \sum \dfrac{\pi^2 EI}{(K_2 L)^2}$ as shown in Eq. 1.

[b] The flexural deflections, as well as the axial and shear deformations, are considered for the computation of $(\delta_{xe} - \delta_{(x-1)e})$.

[c] $(P_e)_3 = \dfrac{V_x h_{sx}}{\delta_{xe} - \delta_{(x-1)e}}$ as shown in Eq. 3.

5.3 Practical Fixed-Base Condition ($G_B = 1$)

In order to achieve the practical fixed-base condition with $G_B = 1$, the computer model of the frame shown in Figure 3(b) is modified to become the frame shown in Figure 5 by adding a base beam W14×90 to connect the bases of the W14×90 columns, as well as by changing the fixed bases to pinned bases. Note that both ends of the added base beam are rigidly connected to the bottom ends of the columns, while the newly added pinned bases are located right below the new rigid connections at the bottom ends of the columns. Referring Figure 5, G_B can be computed as

$$G_B = \frac{\sum(I_c / L_c)}{\sum(I_b / L_b)} = \frac{(999 \text{ in.}^4/180 \text{ in.})}{(999 \text{ in.}^4/180 \text{ in.})} \left[= \frac{(41580 \text{ cm}^4/457 \text{ cm})}{(41580 \text{ cm}^4/457 \text{ cm})} \right] = 1$$

Note that I_b and L_b shown in the above equation are the moment of inertia (about the x-axis) and the length of the base beam, while I_c and L_c are the moment of inertia (about the x-axis) and the length of the column.

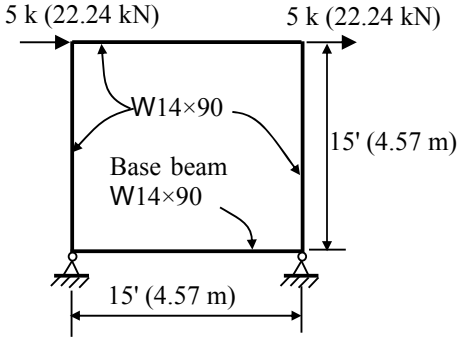

Note: All members are bent about their x-axes due to the applied forces.

Figure 5. Moment Frame with Modified Base Stiffness for the Practical Fixed-Base Condition with $G_B = 1$

Table 7 summarizes and compares the computed $(P_e)_1$ and $(P_e)_2$ values in Eqs. 1 and 2 for the laterally loaded frame with $G_A = 1$ and $G_B = 1$ as shown in Figure 5. Note that the Δ_H value shown in Table 7 is obtained by using the computer software SAP2000, which considers the flexural deflections, as well as the axial and shear deformations, of the members. The results shown in Table 7 indicate that the computed $(P_e)_1$ value for Eq. 1 is about 25% larger than the computed $(P_e)_2$ value for Eq. 2.

Table 7. Comparison of $(P_e)_1$ and $(P_e)_2$ for the Laterally Loaded Frames Shown in Figure 5 (Practical fixed-base connections)

G_A	G_B	K_2	$(P_e)_1$ [a]	Δ_H [b]	$(P_e)_2$ [c]	$(P_e)_1$ vs. $(P_e)_2$
1.0	1.0	1.342	9,800 kips (43 590 kN)	0.196 in. (0.498 cm)	7,810 kips (34 740 kN)	$(P_e)_1 > (P_e)_2$ by 25 %

[a] $(P_e)_1 = \sum \frac{\pi^2 EI}{(K_2 L)^2}$ as shown in Eq. 1.

[b] The flexural deflections, as well as the axial and shear deformations, are considered for the computation of Δ_H.

[c] $(P_e)_2 = R_M \frac{\sum HL}{\Delta_H}$ as shown in Eq. 2.

Table 8 summarizes and compares the computed $(P_e)_1$ and $(P_e)_3$ values in Eqs. 1 and 3 for the laterally loaded frame with $G_A = 1$ and $G_B = 1$ as shown in Figure 5. Note that the $(\delta_{xe} - \delta_{(x-1)e})$ value shown in Table 8 is obtained by using the computer software SAP2000, which considers the flexural deflections, as well as the axial and shear deformations, of the members. The results shown in Table 8 indicate that the computed $(P_e)_1$ value for Eq. 1 is about 7% larger than the computed $(P_e)_3$ value for Eq. 3.

Table 8. Comparison of $(P_e)_1$ and $(P_e)_3$ for the Laterally Loaded Frames Shown in Figure 5 (Practical fixed-base connections)

G_A	G_B	K_2	$(P_e)_1$ [a]	$(\delta_{xe} - \delta_{(x-1)e})$ [b]	$(P_e)_3$ [c]	$(P_e)_1$ vs. $(P_e)_3$
1.0	1.0	1.342	9,800 kips (43 590 kN)	0.196 in. (0.498 cm)	9,180 kips (40 830 kN)	$(P_e)_1 > (P_e)_3$ by 7 %

[a] $(P_e)_1 = \sum \frac{\pi^2 EI}{(K_2 L)^2}$ as shown in Eq. 1.

[b] The flexural deflections, as well as the axial and shear deformations, are considered for the computation of $(\delta_{xe} - \delta_{(x-1)e})$.

[c] $(P_e)_3 = \frac{V_x h_{sx}}{\delta_{xe} - \delta_{(x-1)e}}$ as shown in Eq. 3.

5.4 Practical Pinned-Base Condition ($G_B = 10$)

In order to achieve the practical fixed-base condition with $G_B = 10$, the computer model of the frame shown in Figure 4(b) is modified to become the frame shown in Figure 6 by adding a base beam W8×28 to connect the bases of the W14×90 columns. Note that both ends of the added base beam are rigidly connected to the bottom ends of the columns, while the pinned bases are located right below the new rigid connections at the bottom ends of the columns. Referring Figure 6, the G_B can be computed as

$$G_B = \frac{\sum(I_c / L_c)}{\sum(I_b / L_b)} = \frac{(999 \text{ in.}^4/180 \text{ in.})}{(98 \text{ in.}^4/180 \text{ in.})} \left[= \frac{(41580 \text{ cm}^4/457 \text{ cm})}{(4080 \text{ cm}^4/457 \text{ cm})} \right] \approx 10$$

Note that I_b and L_b shown in the above equation are the moment of inertia (about the x-axis) and the length of the base beam, while I_c and L_c are the moment of inertia (about the x-axis) and the length of the column.

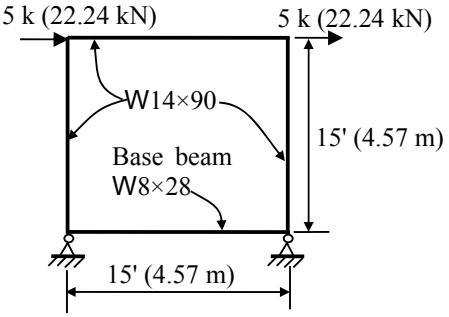

Note: All members are bent about their x-axes due to the applied forces.

Figure 6. Moment Frame with Modified Base Stiffness for the Practical Pinned-Base Condition with $G_B = 10$

Table 9 summarizes and compares the computed $(P_e)_1$ and $(P_e)_2$ values in Eqs. 1 and 2 for the laterally loaded frame with $G_A = 1$ and $G_B = 10$ as shown in Figure 6. Note that the Δ_H value shown in Table 9 is obtained by using the computer software SAP2000, which considers the flexural deflections, as well as the axial and shear deformations, of the members. The results shown in Table 9 indicate that the computed $(P_e)_1$ value for Eq. 1 is about 22% larger than the computed $(P_e)_2$ value for Eq. 2.

Table 9. Comparison of $(P_e)_1$ and $(P_e)_2$ for the Laterally Loaded Frames Shown in Figure 6 (Practical pinned-base connections)

G_A	G_B	K_2	$(P_e)_1$[a]	Δ_H[b]	$(P_e)_2$[c]	$(P_e)_1$ vs. $(P_e)_2$
1.0	10	1.910	4,840 kips (21 530 kN)	0.384 in. (0.975 cm)	3,980 kips (17 700 kN)	$(P_e)_1 > (P_e)_2$ by 22 %

[a] $(P_e)_1 = \sum \frac{\pi^2 EI}{(K_2 L)^2}$ as shown in Eq. 1.

[b] The flexural deflections, as well as the axial and shear deformations, are considered for the computation of Δ_H.

[c] $(P_e)_2 = R_M \frac{\sum HL}{\Delta_H}$ as shown in Eq. 2.

Table 10 summarizes and compares the computed $(P_e)_1$ and $(P_e)_3$ values in Eqs. 1 and 3 for the laterally loaded frame with $G_A = 1$ and $G_B = 10$ as shown in Figure 6. Note that the $(\delta_{xe} - \delta_{(x-1)e})$ value shown in Table 10 is obtained by using the computer software SAP2000, which considers the flexural deflections, as well as the axial and shear deformations, of the members. The results shown in Table 10 indicate that the computed $(P_e)_1$ value for Eq. 1 is about 3% larger than the computed $(P_e)_3$ value for Eq. 3.

Table 10. Comparison of $(P_e)_1$ and $(P_e)_3$ for the Laterally Loaded Frames Shown in Figure 6 (Practical pinned-base connections)

G_A	G_B	K_2	$(P_e)_1$[a]	$(\delta_{xe} - \delta_{(x-1)e})$[b]	$(P_e)_3$[c]	$(P_e)_1$ vs. $(P_e)_3$
1.0	10	1.910	4,840 kips (21 530 kN)	0.384 in. (0.975 cm)	4,690 kips (20 860 kN)	$(P_e)_1 > (P_e)_3$ by 3 %

[a] $(P_e)_1 = \sum \frac{\pi^2 EI}{(K_2 L)^2}$ as shown in Eq. 1.

[b] The flexural deflections, as well as the axial and shear deformations, are considered for the computation of $(\delta_{xe} - \delta_{(x-1)e})$.

[c] $(P_e)_3 = \frac{V_x h_{sx}}{\delta_{xe} - \delta_{(x-1)e}}$ as shown in Eq. 3.

6. DISCUSSION AND CONCLUSION

The approaches that have been commonly used by structural engineers for the computation of the sidesway magnification factor for the design of columns in steel moment frames subjected to the P-Δ effect are the column-lateral-buckling-strength approach (suggested by the 2005 AISC Specification for Structural Steel Buildings), the story-lateral-stiffness approach (suggested by the ASCE/SEI 7-10 Minimum Design Loads for Buildings and Other Structures), and the modified-story-lateral-stiffness approach (suggested by the 2005 and 2010 AISC Specification for Structural Steel Buildings). The column-lateral-buckling-strength approach involves the computation of the elastic story sidesway buckling resistance, the story-lateral-stiffness approach involves the computation of the elastic analysis of the first-order interstory drift due to lateral forces, and the modified-story-lateral-stiffness approach involves the computation of the first-order interstory drift using the lateral stiffness modification coefficient, R_M, for moment-frame systems.

The story-lateral-stiffness approach has been recognized as an accurate approach for low- or medium-rise rigid frames, while the column-lateral-buckling-strength approach has been classified as a very approximate approach. Nevertheless, the results of the study conducted in this paper are that (1) the sidesway magnification factor derived from the column-lateral-buckling-strength approach closely agrees with that derived from the modified story-lateral-stiffness approach if only the flexural deflections are considered in the frame analysis for the computation of the interstory drifts of the frame and (2) the sidesway magnification factor derived from the column-lateral-buckling-strength approach closely agrees with that derived from the story-lateral-stiffness approach if the flexural deflections, as well as the shear and axial deformations, are considered in the frame analysis for the computation of the interstory drifts of the frame.

Since the column-lateral-buckling-strength approach is a hand-calculated approach, it can be used rapidly and practically to confirm the accuracy and validity of the results derived from the story-lateral-stiffness approach, which is usually carried out with computer software for the computation of sidesway magnification factors for steel moment frames subjected to the P-Δ effect.

NOTATION

The following symbols are used in this paper:

B_2 = sidesway amplifier
E = the modulus of elasticity of steel, 29,000 ksi (200 000 MPa)

G = the restraint factor at the column end
H = the story shear produced by the lateral forces used to compute Δ_H
$\sum H$ = the story shear produced by the lateral forces used to compute Δ_H
h_{sx} = the story height below level x
I = the moment of inertia in the plane of bending
I_b = moment of inertia of beam
I_c = moment of inertia of column
K_2 = the effective length factor in the plane of bending, based on sidesway buckling
L = the story height
L_b = the beam length
L_c = the column length
P_{mf} = the total vertical load in columns in the story that are part of moment frames
$\sum P_{nt}$ = the total vertical load supported by the story
P_{story} = the total vertical load supported by the story
P_x = the total vertical design load at and above level x
R_M = 0.85 for moment-frame systems
V_x = the shear force acting between levels x and x-1
α = 1.00 for LRFD
Δ_H = the first-order interstory drift resulting from lateral forces
δ_{xe} = the displacement at level x by a first-order elastic analysis
$\delta_{(x-1)e}$ = the displacement at level x-1 by a first-order elastic analysis
θ_i = rotation at joint i

REFERENCES

[1] Gaiotti, R. and Smith, B.S., "P-delta Analysis for Building Structures", Journal of Structural Engineering, ASCE, 1989, Vol. 115, No. 4, pp. 755-770.

[2] AISC, "Specification for Structural Steel buildings", American Institute of Steel Construction, Inc., Chicago, IL., 2005.

[3] ASCE, "ASCE/SEI 7-10 Minimum Design Loads for Buildings and Other Structures", American Society of Civil Engineers, Reston, Virginia, 2010.

[4] AISC, "Specification for Structural Steel Buildings", American Institute of Steel Construction, Inc., Chicago, IL., 2010.

[5] Timoshenko, S.P. and Gere, J.M., "Theory of Elastic Stability", 2nd Ed., McGraw-Hill Book Co., New York, N.Y., 1961.

[6] Salmon, C.G., Johnson, J.E. and Malhas, F.A., "Steel Structures, Design and Behavior", 5th Ed., Pearson Prentice Hall, Upper Saddle River, N.J., 2009.

[7] Dumonteil, P., "Simple Equations for Effective Length Factors", Engineering Journal, AISC, 3rd quarter, 1992, pp. 111-115.

[8] AISC, "Steel Design Guide 1 – Base Plate and Anchor Rod Design", 2nd Ed., American Institute of Steel Construction, Chicago, IL., 2010.

[9] Hsiao, J.K., "Computation of Fundamental Periods for Moment Frames Using a Hand-calculated Approach", Electronic Journal of Structural Engineering, 2009, Vol. 9, pp. 16-28.

[10] AISC, "Steel Construction Manual", 14th Ed., American Institute of Steel Construction, Inc., Chicago, IL. 2011.

[11] SAP2000 Educational, "SAP2000 Manuals", Computers and Structures, Inc., Berkeley, CA., 1997.

COMPRESSION BEHAVIOR OF DOUBLER-PLATE REINFORCED SQUARE HOLLOW SECTION T-JOINTS

Hongfei Chang[1,2*], Junwu Xia[1,2], Fengjie Zhang[2,3] and Hong Chang[2,3]

[1] *JiangSu Key Laboratory of Environmental Impact and Structural Safety in Engineering, China University of Mining and Technology, Xuzhou, China*
[2] *Key Laboratory of Deep Geotechnical and Underground Engineering, China University of Mining and Technology, Xuzhou, China*
[3] *School of Mechanics and Civil Engineering, China University of Mining and Technology, Xuzhou, China*
**(Corresponding author: E-mail: honfee@126.com)*

Received: 23 February 2013; Revised: 15 May 2013; Accepted: 39 June 2013

ABSTRACT: The doubler-plate is widely used to improve the behavior of truss joints, and it has been proven to be effective in increasing the load carrying capacity of circle or square hollow section joints, yet the current design approach for doubler-plate reinforced joints is elementary. This study investigates the behavior of doubler-plate reinforced square hollow section (DPR-SHS) T-joints under brace compression, by experimental tests and finite element analysis (FEA). Details of the test arrangement were summarized, and the behaviors of failure modes, strain distribution and deformation characteristics of the specimens were analyzed. After confirming the accuracy of the finite element model with the test evidence, the reinforcement mechanism of doubler-plate was analyzed by parametric study. Both the experimental and FEA results shown the compression strength of the joint is significantly improved by welding a doubler-plate on the surface of the chord. The reinforcement efficiency of the doubler-plate increased with the increase of doubler-plate width and length, yet decreased with the increase of doubler-plate thickness and yielding strength. The thickness of doubler-plate influences the strength of the joint more than the width or length. Given a proper thickness, the reinforcement mechanism of the doubler-plate was yielding together with the chord flange. Finally, design formulas for DPR-SHS T-joints were proposed using yielding line method, which agree well with the experimental and FEA results. Yet the formula of Eurocode3-1-8 seems to oversimplify the design of DPR-SHS joint, which may lead to inaccurate estimation of the compression strength of the joint.

Keywords: Square hollow section, reinforced T-joints, doubler-plate, compression behavior, experiment, finite element, yielding line

1. INTRODUCTION

Tubular steel members are widely used in large span structures all around the world (Wardenier [1], Lesani [2]), for their structural efficiency as well as aesthetic quality. However, the hollow section members are known as weak in resisting the radial loading for thin wall (Packer [3], Shao [4]). On the other hand, the direct welded members often suffer high stress concentration at the connection zone (Nazari [5], Soh [6]), increasing the damage risk for the integral structure. As a result, joint reinforcement is always essential (Packer [3], Shao [4], Nazari [5], Soh [6], Lee [7]).

During the last decades, several reinforcing measures have been recommended to improve the behavior of tubular joints (Packer [3]). In general, these measures can be classified as internal reinforcement (Packer [3], Lee [7]) and external reinforcement (Hoon [8], Choo [9], Van [10], Fung [11], Choo [12], Feng [13], Korol [14], Korol [15], Soh [16]). The internal reinforcement such as stiffened ring, diaphragms, grout or horizontal stiffener, as well as chord wall local thickening (Yang [17]), has been proved efficient to increase the strength of the joint, while has little influence on the joint appearance (Packer [3], Lee [7]). However, the construction for internal reinforcement was not easy, for the tubular section is closed. In this regard, external reinforcement (Packer [3], CIDECT [21]) such as brace plate stiffeners, haunch stiffeners, truncated pyramid stiffeners, doubler or collar plate, FRP plate (Lesani [18]), through wall bolts (Jose [19]), were more appreciated for their reinforcement efficiency as well as fabrication convenience. Among

these reinforcement measures, the use of doubler-plate is widespread. For a doubler-plate reinforced tubular joint (Figure 1), the doubler-plate is welded onto the chord surface by using filet weld, and then the brace is welded to the doubler-plate. This reinforcement is easy to fabricate and has little influence on the joint aesthetics, it can also improve the strength of the joint efficiently (Hoon [8], Choo [9], Van [10], Fung [11], Choo [12], Feng [13], Korol [14], Korol [15], Soh [16]).

Various references can be found related to doubler-plate reinforced joints (Hoon [8], Choo [9], Van [10], Fung [11], Choo [12], Feng [13], Korol [14], Korol [15], Soh [16]). The ultimate strength of doubler-plate reinforced circle hollow section (DPR-CHS) joints was investigated by experiment (Hoon [8], Choo [9]) or FE method （Van [10], Fung [11], Choo [12], Feng [13]）, and the reinforcement mechanism as well as design recommendations for doubler-plate was put forward. However, note the load carrying mechanism of DPR-SHS joint is different from that of DPR-CHS ones （Korol [14]）. Korol [14, 15] has proposed the flexural and compressive strength formulas of DPR-SHS joint using yield line theory, and verified the theory formulas by a set of laboratory test of DPR-SHS joints under brace bending [15]. Soh [16] has reported their test results on a DPR-SHS T-joint, and analyzed the ultimate strength of DPR-SHS joints using FE method. The influence of three geometric parameters such as the chord length (α), brace to chord diameter (β) and chord diameter to thickness ratio (γ) were investigated, and an equation was proposed by regression analysis. Soh [6] also compared the stress concentration factors (SCF) of DPR-SHS joints with unreinforced ones, and found that the doubler-plate can improve the fatigue performance of the joint.

Although there is no lack of experimental data for DPR-CHS joints (Hoon [8], Choo [9], Van [10], Fung [11], Choo [12]), little relevant experimental information is currently available for DPR-SHS joints subjected to brace compression load (Soh [16]). Because of the lack of test evidence, the current design approach for axially loaded DPR-SHS joints is elementary (EC3 [20], CIDECT [21]). To date, the configuration of doubler-plate for SHS joints proposed by Korol [14] is widely adopted by many standards or guidelines (CIDECT [21]) around the world. However, the applicability of these configurations should be re-examined. On the other hand, the design formula for DPR-SHS joints under compression is seldom available. The formula of Eurocode3-1-8 (EC3 [20]) seems oversimplify the design of DPR-SHS joint, which may misestimate the compression strength of the joint.

Thus, to investigate the compression behavior of DPR-SHS T-joints, a set of experimental tests were conducted. The design of specimens and arrangement of tests were described, and behaviors such as the failure modes, strain distribution and deformation characteristics of the specimens were discussed. Then, a finite element (FE) model was established and corroborated for further study. After confirming the accuracy of the FE model with the test evidence, the reinforcement mechanism of doubler-plate was analyzed by an extensive parametric study, and design formulas or recommendations for DPR-SHS T-joints under brace compression were proposed.

2. EXPERIMENTAL INVESTIGATIONS

2.1 Details of Specimens

For a DPR joint, the strength of the joint is improved by welding a doubler-plate onto the surface of the chord. This reinforcement is applicable to tubular joints governs by chord surface yielding (EC3 [20]). Figure 1 shows the configuration of a square tubular T-joint with doubler-plate reinforcement. In addition, some geometric parameters are also indicated in the same figure, and the quantities of specific parameters are listed in Table 1. Coupon tests were conducted before the

experimental test, and the measured yield stresses of the steel materials are also tabulated in Table 1. For convenience, any quantity with a subscript "0", "1" or "2" denotes a geometric or mechanical parameter of the chord, the brace and the doubler-plate respectively.

A total of two T-joints without any reinforcement and two T-joints reinforced with doubler-plate were designed for experimental test. In the design of the four specimens, the square tubular joints had different values of one critical geometric parameter, namely β. For comparison purpose, the unreinforced T-joints and the reinforced ones had the same geometric dimensions for the chord and the brace. For brevity, the doubler-plate was designed to have same thickness, while the length and the width of the plate were different. Therefore, the four specimens were classified as two groups as tabulated in Table 1. Each group includes one unreinforced specimen (namely: URT) and one corresponding specimen with doubler-plate reinforcement (namely: DPT).

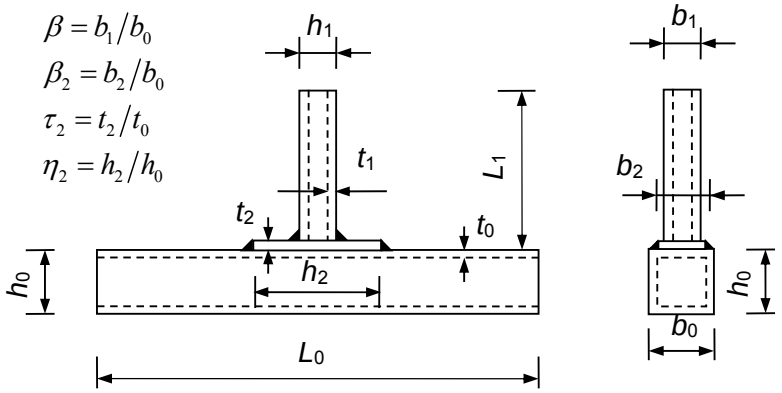

Figure 1. Details of Doubler-plate Reinforced Square Tubular T-joint

Table 1. Geometry and Material Properties of the Specimens

No	Chord					Brace					Doubler-plate			
	b_0	h_0	t_0	L_0	f_{y0}	b_1	h_1	t_1	L_1	f_{y1}	b_2	h_2	t_2	f_{y2}
URT-40	100	100	5	650	356	40	40	4	300	372	—			
DPT-40	100	100	5	650	356	40	40	4	300	372	70	75	7	285
URT--80	100	100	5	650	356	80	80	4	300	265	—			
DPT-80	100	100	5	650	356	80	80	4	300	265	88	160	7	285

Note: All geometry parameters are in *mm*, f_{y0}, f_{y1} and f_{y2} is the yielding strength of the chord, the brace and the doubler-plate steel in $N \cdot mm^{-2}$ respectively.

2.2 Test Arrangement

As shown in Figure 2, the specimens were fixed at both ends of the chord (Wu [22], Chang [23]), and the monotonic loading was applied at the brace end by an electro-hydraulic servo actuator with a maximum capacity of 1000 kN. To control the large deformation may occur in the stage of plastic flow, a vertical displacement at the brace end was used in the loading program. Once the displacement was applied at the brace end, the required axial loading can be measured automatically by the machine.

For each specimen, the instrumentation included transducers to measure the displacements and strain distribution at selected points. Figure 2 (a) shows the general arrangement of the displacement transducers, with six of these (namely DT1, DT2, DT3 and DT6, DT7, DT8) symmetrically arranged on the surface of the chord measuring the displacements of the chord, and

one transducer (namely: DT4) measuring the displacement of the brace end. In addition, another transducer (namely: DT5) was placed under the chord at the center of the T-joint, monitoring the vertical displacement of the chord bottom surface. Figure 2 (b) shows the general arrangement of the strain gauges on the surface of the chord. The strain gauges were located 15 mm away from the brace-to-chord weld toe for unreinforced joints, and 15 mm away from the plate-to-chord weld toe for DPR-SHS joints. Three groups of strain gauges (namely SG1, SG2 and SG3) were arranged near the brace-to-chord intersection for each specimen. For each group, there were three strain gauges, located on the angle of 0, 45 and 90 degree respectively.

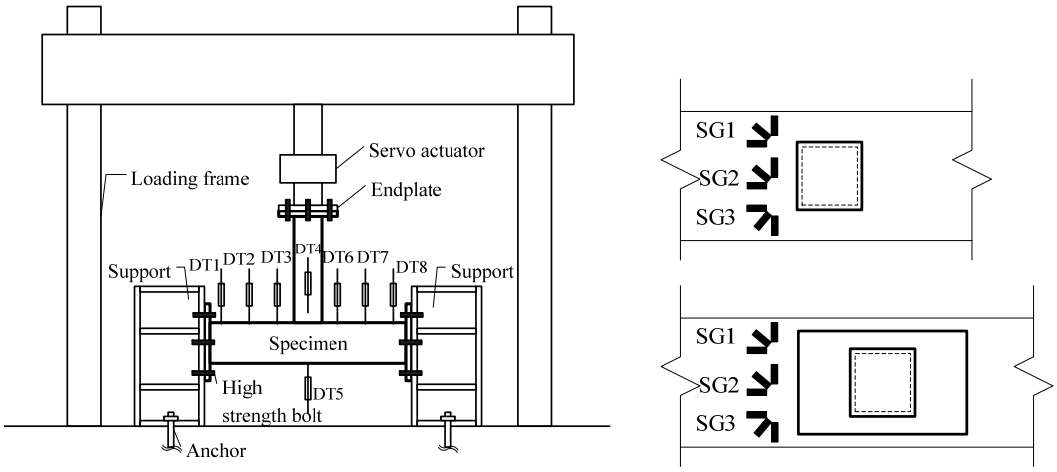

(a) (b)

Figure 2. Arrangement of Test Specimen and Instruments:
(a) Front View; (b) Strain Gauges Layout

2.3 Observations from Experimental Test

For unreinforced square tubular T-joints, two kinds of failure modes namely chord surface yielding or chord web buckling are frequently occurred (EC3 [20], CIDECT [21]). As to the unreinforced specimen URT-40, indentation of the chord surface appeared under a small brace compression. With the growth of brace compression load, the indentation increased and the up fillet of the chord yielded. Finally, the test terminated after the indentation of the chord surface was about 15 mm. Figure 3 (a) shows the chord surface yielding failure of the unreinforced specimen URT-40. The brace-to-chord width ratio of specimen URT-80 was 0.8, little indentation of the chord surface was observed. However, the chord web buckled suddenly when the brace load reached at 200 kN, and the strength of the joint decreased slightly. The failure mode of specimen URT-80 was chord web buckling and surface yielding, as shown in Figure 3 (b).

For reinforced specimen DPT-40, indentation of the chord surface was invisible until the load reached about 140 kN. With the growth of brace compression load, the indentation increased and the doubler-plate bent. The test terminated after the compression of the brace reached at 200 kN, which leading to overall bending of the chord. Figure 3 (c) shows the yielding of chord surface and doubler-plate for DPT-40. For specimen DPT-80, no indentation of the chord surface appeared even before 300 kN. As the load reached about 380 kN, the brace buckled suddenly and the compression strength of the joint decreased rapidly. The failure of specimen DPT-80 is brace buckling as shown in Figure 3 (d).

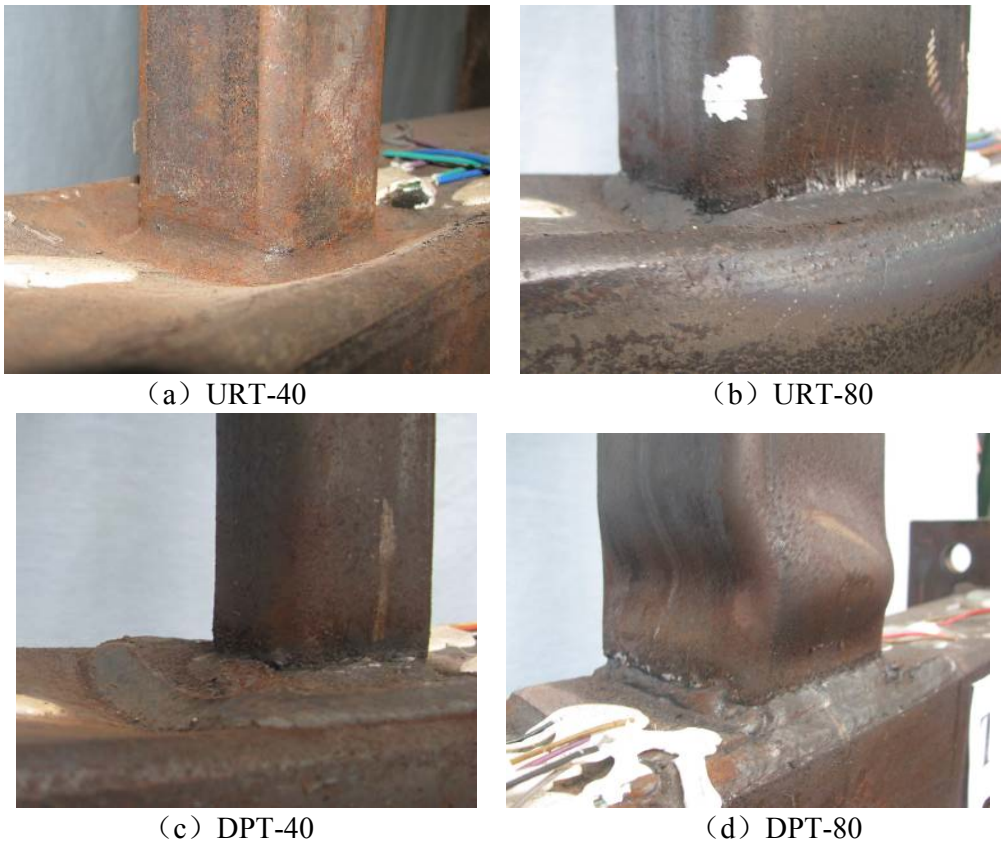

（a）URT-40 （b）URT-80

（c）DPT-40 （d）DPT-80

Figure 3. Failure Modes of the Joints

2.4 Strain Distribution of the Chord

Figure 4 presents the load-strain curve for each of the four tested specimens. For unreinforced specimen URT-40, strain of the chord surface increased obviously as the brace compression exceed about 60 kN, demonstrating a local yielding of the joint occurred. The load-strain curves of specimen URT-80 almost remained a linear growth even before the failure of the joint. The strength of the joint kept unchanged as the load reached about 200 kN, for the buckling of the chord web occurred. The buckling of the web also leading to the bending of the flange, and the strain of the chord surface increased rapidly.

For the joint with doubler-plate reinforcement, the strain distribution law of the chord surface was almost the same to the unreinforced ones. For specimen DPT-40, strain of the chord surface increased slowly before 160 kN, then increased rapidly after 160 kN. The strain of specimen DPT-80 was small before the compression load of the brace reached about 350 kN. Although the strain of the chord surface increased after the load of 350 kN, a sudden drop of the load appeared because the buckling of the brace.

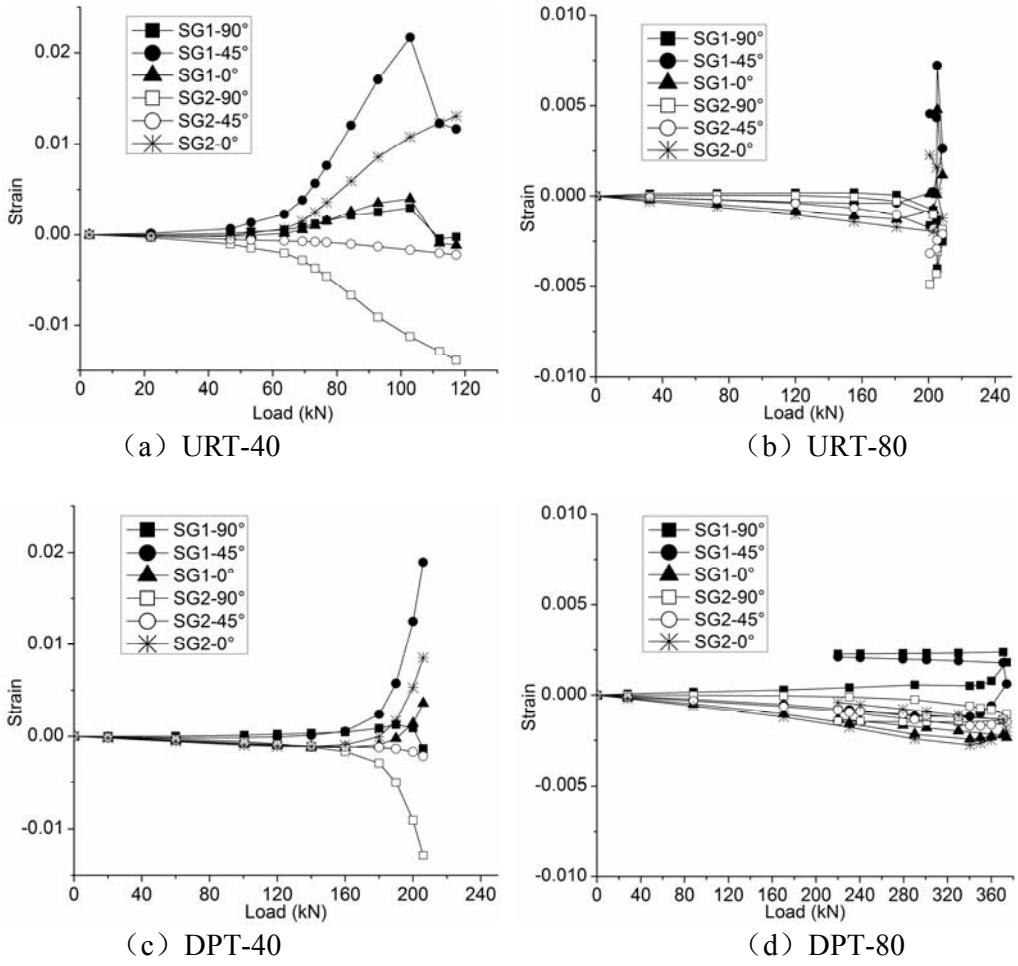

（a）URT-40 （b）URT-80

（c）DPT-40 （d）DPT-80

Figure 4. Load-strain Curves of Chord Flange

2.5 Deformation of the Chord

In this section, the deformation data of the chord obtained from the experiments are presented and evaluated. First, the displacement readings under a certain brace compression of all the eight transducers are shown in Figure 5. The displacement of DT1~3 and DT5~8 displayed the overall bending of the chord, and DT4 shown the deformation of the brace-chord intersection. As a result, the local deformation of the brace-chord intersection can be obtained from the difference between DT4 and DT5. It can be seen the overall bending of the chord occurred before the load of 60, 200, 160 and 378 kN for specimen URT-40, URT-80, DPT-40 and DPT-80 respectively, as the difference between DT4 and DT5 is small. This agrees well with the findings of the chord surface strain distribution.

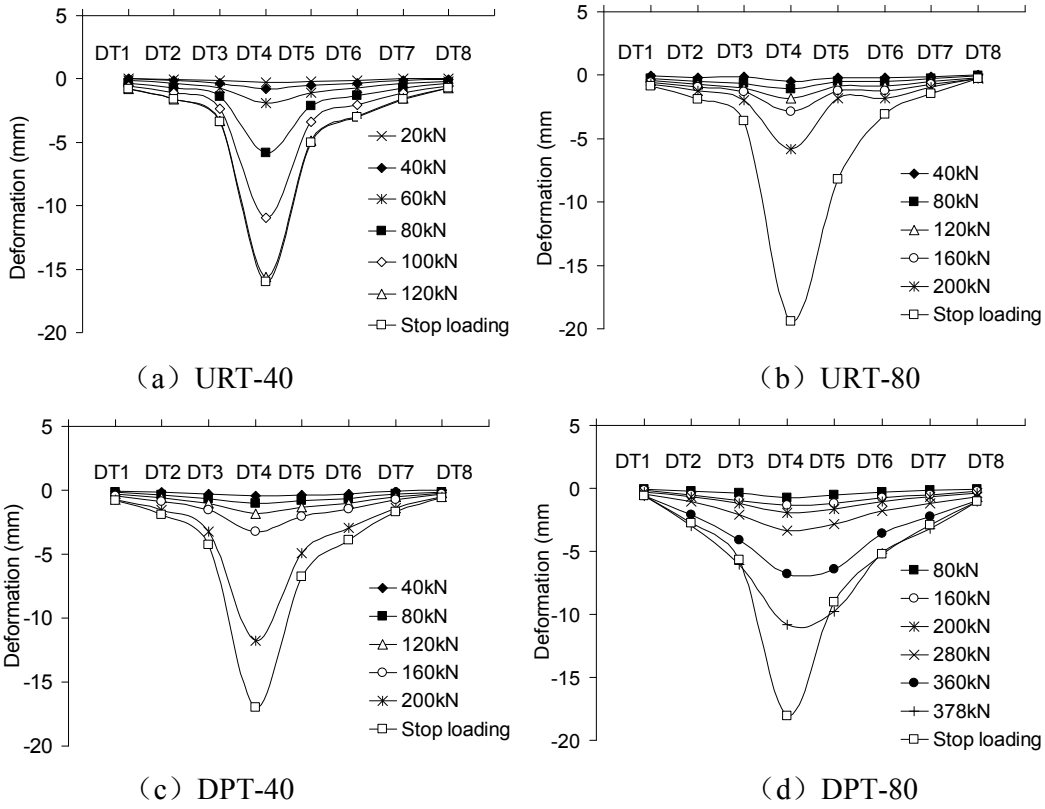

Figure 5. Deformation Details of the Chord

2.6 Strength of the Joints

For the strength evaluation of a tubular joint, the load-deformation curve is widely used (Lu [24], Zhao [25]). Lu [24] has proposed a general deformation limit based on the load-deformation curve, to cover all types of welded hot-rolled section tubular joints. Then Zhao [25] confirmed the applicability of the proposed deformation limit for welded T-joints in cold-formed rectangle hollow sections. Zhao [25] investigated the test results of web buckling failure and chord flange failure, and suggested the deformation limit for cold-formed rectangle hollow section T-joints should be $3\%b_0$ for $0.6\leq\beta\leq0.8$ or $2\gamma\leq 15$ and $1\%b_0$ for $0.3\leq\beta<0.6$ and $2\gamma> 15$.

The load-deformation curves of the tested specimen are shown in Figure 6. For DPR-SHS T-joints, the load-deformation curves were above the curves for the unreinforced ones. The deformation refers to the displacement of the chord cross section at the center of the T-joint, which was calculated by subtracting the average value of the two transducer readings at the chord ends (namely: DT1 and DT8), from the transducer reading near the chord–brace intersection (namely: DT4).

By using Zhao's [25] method, the compression strength of each specimen was determined and listed in Table 2. It is found from Table 2 the doubler-plate reinforced joint is "stronger" than the unreinforced joint and hence exhibits a larger ultimate strength. For specimen DPT-40, the strength improvement is up to 136% compared to the unreinforced one. However, the increase of DPT-80 is only 56% because of the over-reinforcement of the joint, which leading to the buckling of the brace occurred unexpectedly. Table 2 also lists the ultimate strength determined by EC3 [20], which agree well with the test results with a mean ratio of 0.875 and a coefficient of variation (COV) of

0.009. However, the EC3 [20] underestimates the strength of DPT-40, yet overestimates the strength of DPT-80.

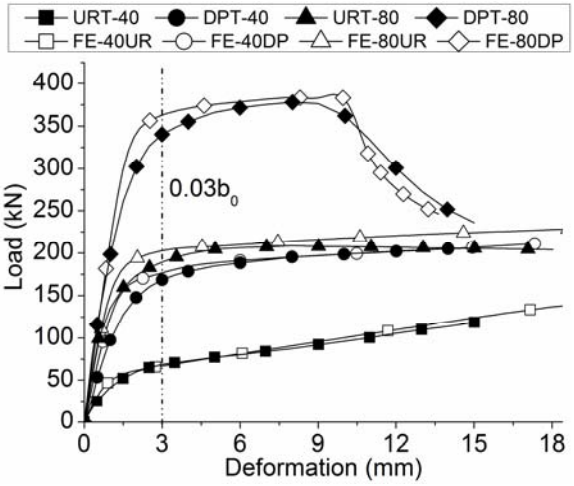

Figure 6. Load-deformation Curves of Specimens

Table 2. Compression Strength of the Specimens

Specimens	Failure mode	$P_{1\%}$ /(kN)	$P_{3\%}$ /(kN)	$P_{3\%}/P_{1\%}$	P_{max} /(kN)	P_{ult} /(kN)	P_{DPT}/P_{URT}	P_{EC3} /(kN)	P_{EC3}/P_{ult}
URT-40	FY	41.6	68.8	1.65	119.2	62.4	1.0	57.8	0.93
DPT-40	FY+DPY	98.4	168.4	1.71	207.2	147.6	2.36	113.3	0.77
URT-80	FY+WB	135.2	189	1.4	208.4	189	1.0	150.8	0.80
DPT-80	BB	197	340.4	1.73	378	295.5	1.56	295.6	1.0
MEAN									0.875
COV									0.009

Note: (1) FY: chord flange yielding, DPY: doubler-plate yielding, WB: chord web buckling, BB: brace buckling
(2) $P_{1\%}$ and $P_{3\%}$ = load when the brace deformation was $1\%b_0$ and $3\%b_0$; P_{max} = maximum load of the test; P_{ult} = ultimate strength of the joint; P_{EC3} = ultimate strength determined by EC3 [20].

3. PARAMETRIC STUDY

3.1 Finite Element Strategy

Because of the high costs of laboratory tests, the FE packages were widely used to offer an attractive and cheaper alternative to generate reliable additional data, provided the accuracy of the FE model was first verified with the test evidence. There are many publications related to the numerical simulation of unreinforced or doubler-plate reinforced T-joints (Van [10], Fung [11], Choo [12], Feng [13], Soh [16]). The behaviors of DPR-CHS T-joints (Van [10], Fung [11]); X-joints (Choo [12]); Y-joints (Feng [13]) as well as DPR-SHS T-joints (Soh [16]) were investigated.

In the current study, a numerical model was developed to simulate the 4 experimental specimens. Because the doubler-plate configurations require the definition of contact between the various components, the joints were modeled using 20-noded solid elements (Van [10], Soh [16]). The contact between the doubler-plate and the chord surface was modeled using surface-to-surface contact element. In the FE model, the material property was the same as the test, and a bilinear stress–strain relationship was assumed. The elastic modulus was 200 GPa, and the hardening modulus was 1/100th of the elastic modulus (Shao [4]). The chord was fixed on the ends, and a displacement controlled compression loading was applied on the end of the brace until the failure of the joint. For each FE model, the element size varied in such a way that smaller elements were used where the stress gradient was more critical. Therefore the mesh density decreases from the vicinity of the intersection to the end of the brace or chord. Preliminary FE analyzes showed that such mesh density was able to produce results with good accuracy. A linear search algorithm was adopted to solve the problem, and the auto time stepping was activated to decrease the iteration. To decrease the computational time, a quarter of the T-joint was modeled. The meshing detail of the model is pictured in Figure 7.

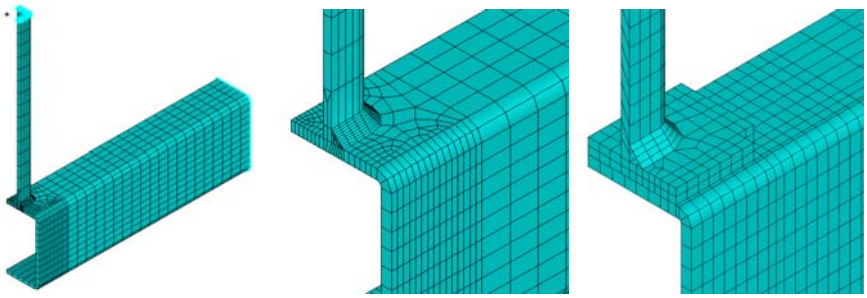

（a）FE model, （b）unreinforced joint, （c）doubler-plate reinforced joint

Figure 7**.** Finite Element Models of the Test Specimens

3.2 Comparison between Experimental and Numerical Results

Because the plastic cumulative damage and crack development of the steel or weld was ignored in the FE model, the maximum displacement of the brace end was determined as 20mm. Nevertheless, the good agreement between the experiments and numerical results of failure modes can be observed in Figure 8, where the specimen FE40-UR and FE40-DP failure by yielding of chord surface or doubler-plate; FE80-UR by buckling of chord web and FE80-DP by buckling of the brace.

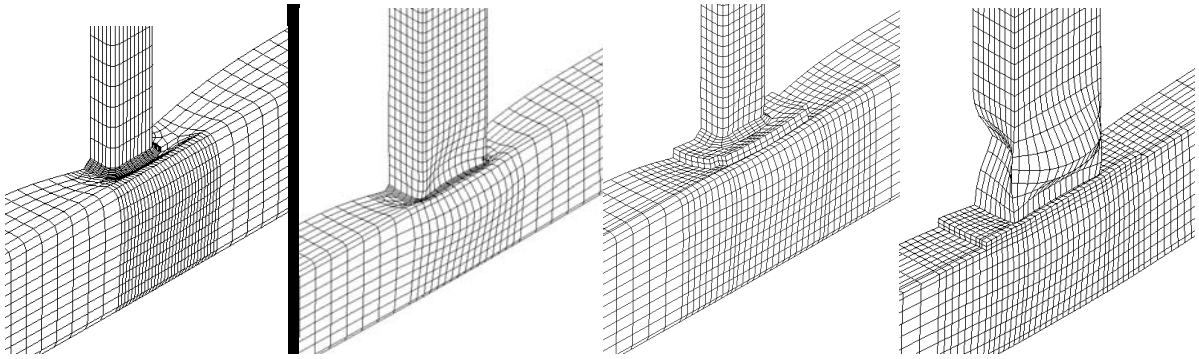

（a）FE40-UR; （b）FE80-UR; （c）FE40-DP; （d）FE80-DP

Figure 8. FEA Failure Modes

The numerically determined load-deformation curves are presented in Figure 6, together with the solid lines of experimental curves. The FEA determined ultimate strength of the joint is summarized in Table 3. As can be observed from Figure 8 and Table 3, the numerical and experimental results matched well, the average ultimate strength of FEA was 10% above that of the test with a COV of 0.003. This discrepancy was not surprising since the current FE models ignored the geometry negative deviation of the chord or brace, as well as the thermal effect of welding. Anyway, the accuracy of the FE model was satisfactory for the strength evaluation of the unreinforced or DPR-SHS T-joints under brace compression.

Table 3. Ultimate Strength of the FE Simulation

Specimen	Failure mode	$P_{1\%}$ /(kN)	$P_{3\%}$ /(kN)	$P_{3\%}/P_{1\%}$	P_{FE} /(kN)	P_{ult} /(kN)	P_{FE}/P_{ult}
FE40-UR	FY	48.3	66.8	1.38	66.8	62.4	1.07
FE40-DP	FY+DPY	120.4	176.3	1.46	176.3	147.6	1.19
FE80-UR	FY+WB	146.3	201.8	1.38	201.8	189	1.07
FE80-DP	BB	210.4	362.1	1.72	315.6	295.5	1.07
MEAN							1.1
COV							0.003

Note: (1) FY: chord flange yielding; DPY: doubler-plate yielding; WB: chord web buckling; BB: brace buckling;
(2) $P_{1\%}$ and $P_{3\%}$ = load when the brace deformation was $1\%b_0$ and $3\%b_0$; P_{FE} = ultimate strength determined by FEA, P_{ult} = ultimate strength by test.

3.3 Numerical Research Program

In this section, the behavior of DPR-SHS T-joint is further discussed by numerical parameter study. The geometries of the chord or brace and the finite element strategy were the same as before. However, the material model and the restraint condition were simplified. For example, to eliminate the influence of material nonlinearity, the perfect elastic-plastic material model was used. The yielding strength of the steel for the chord was 345 N/mm^2, and the steel for the brace was determined as 420 N/mm^2 to prevent the unexpected brace buckling as observed in the experiment. In addition, the bottom surface of the chord was continuous supported to eliminate the influence of overall chord bending.

In the parameter study, the effect of the doubler-plate geometry and material on the compression strength of the joint was mainly concerned. At first, three unreinforced T-joints with the brace-to-chord width ratio of 0.4, 0.6 and 0.8 were modeled as benchmark specimens. Then, a large number of DPR joints were simulated by changing the width, the length or the thickness of the doubler-plate. In addition, the yielding strength of doubler-plate was determined as 235 N/mm^2 or 345 N/mm^2 for the joints with the parameter of β_2=0.9. Overall, 3 unreinforced and 120 DPR-SHS T-joints were analyzed, as listed in Table 4.

Table 4. Reinforcement Parameters for FEA

No	$b_0\times h_0\times t_0$	$b_1\times h_1\times t_1$	β	$\beta_2=b_2/b_0$	$\tau_2=t_2/t_0$	$\eta_2=h_2/b_0$
DP40-FE	100×100×5	40×40×4	0.4	0.7; 0.8;0.9*	1.0; 1.4; 2.0	0.8; 1.0; 1.2; 1.6; 2.0
DP60-FE	100×100×5	60×60×4	0.6	0.9*	1.0; 1.4; 2.0	0.8; 1.0; 1.2; 1.6; 2.0
DP80-FE	100×100×5	80×80×4	0.8	0.9*	1.0; 1.4; 2.0	0.9; 1.0; 1.2; 1.6; 2.0

Note: * the yielding strength of the doubler-plate was 235 N/mm^2 or 345 N/mm^2.

3.4 Load-displacement Curves

By picking the displacement and the reaction force at the end of the brace, the load-deformation curves of the simulated joints are shown in Figure 9. It can be seen from Figure 9 the curves of DPR-SHS T-joints are far above the unreinforced ones. The compression strength of the joint increased apparently by increasing the thickness of the doubler-plate. Yet the influence of the doubler-plate width or length was not obvious. For example, the curves almost coincide when the length of the doubler-plate exceeded a certain range (namely: $\eta_2 \geq 1.6$), which indicated the strength of the joint tends unchanged. For the DPR-SHS joints with a small width ratio (namely: $\beta \leq 0.6$), the load-deformation curves did not have a pronounced peak load, demonstrating the yielding of chord flange (Figure 10a) occurred (Zhao [25]). Conversely, the load-deformation curves for joint of β=0.8 had obvious peak load, indicating the failure mode of chord web buckling (Figure 10b) occurred (Zhao [25]).

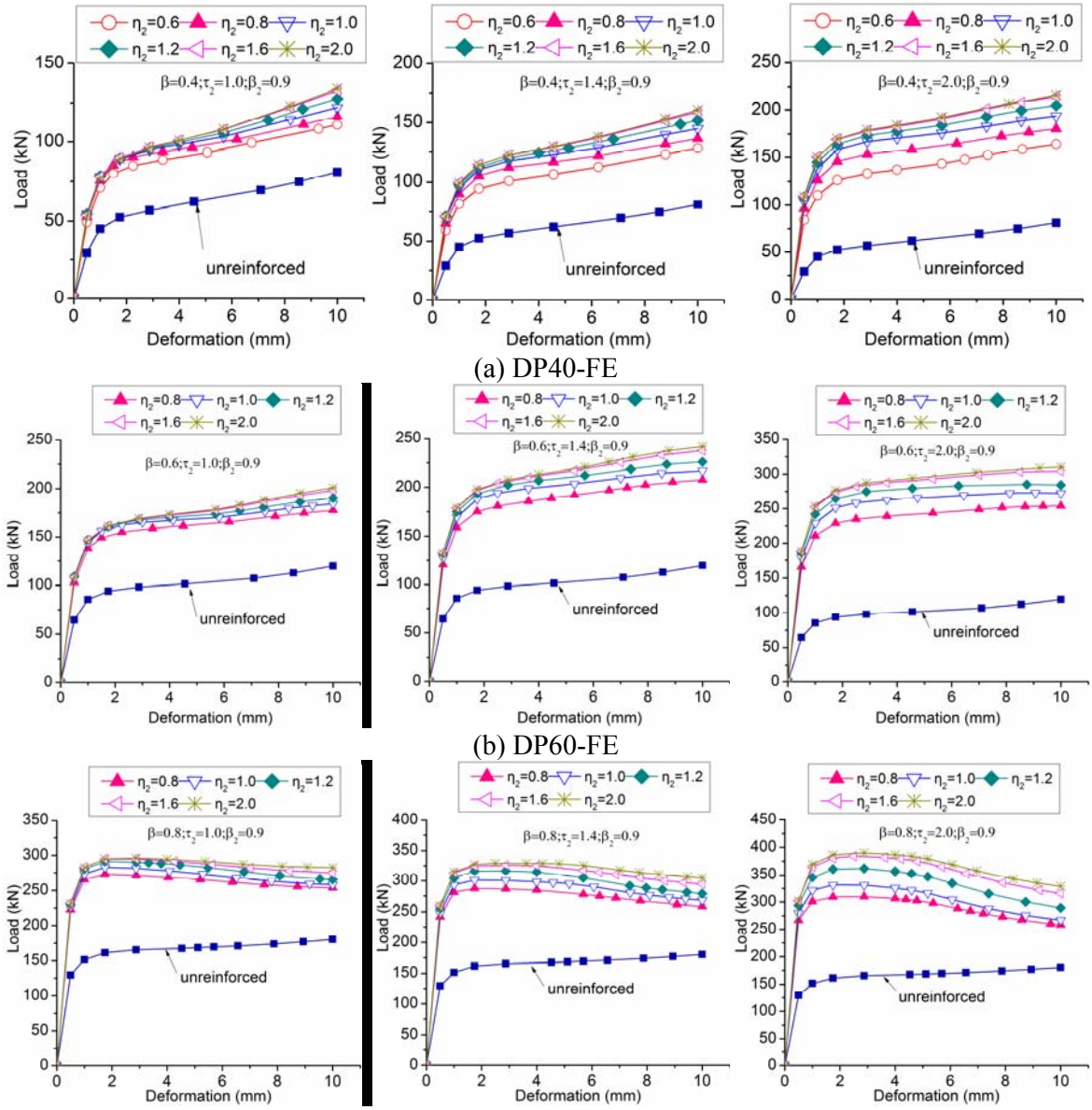

(a) DP40-FE

(b) DP60-FE

(c) DP80-FE

Figure 9. Typical Load-deformation Curves of FE Simulation

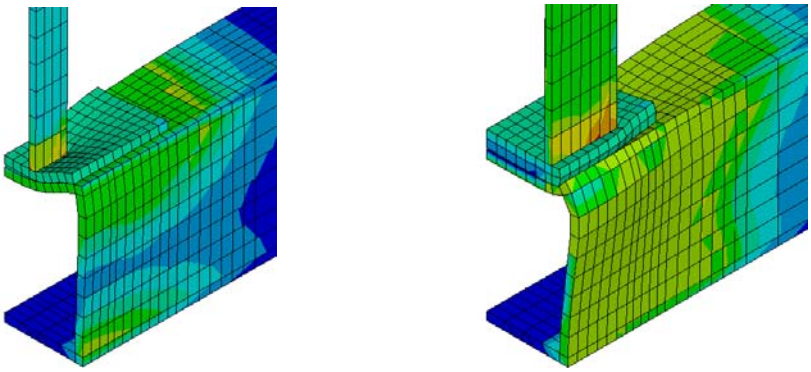

（a）chord flange and doubler-plate yielding （b）chord web buckling

Figure 10. Typical Failure Mode of DPR-SHS Joints

3.5 Sensitivity Analysis

In this section, the influence of doubler-plate geometry or material on the compression strength of DPR T-joint is further analyzed. The compression strength of each simulated specimen is tabulated in Table 5. In the parametric analysis, the reinforcing efficiency of doubler-plate can be investigated by analyzing the effect of one normalized parameter, i.e. R_E, representing the ratio of compression strength incremental for DPR-SHS joint and four times plastic moment per unit length of the doubler-plate.

$$R_E = \frac{P_{dp} - P_{y0}}{f_{y2} t_2^2} \tag{1}$$

In which P_{dp} is the compression strength of the DPR-SHS T-joint, P_{y0} is the compression strength of the unreinforced T-joint, f_{y2} is the yielding strength of the doubler-plate, t_2 is the thickness of the doubler-plate.

Table 5. Compression Strength of the Joints by FEA (kN)

NO	β	β_2	τ_2	η_2				
				0.8	1.0	1.2	1.6	2.0
DP40-FE	0.4	0	0	57.1				
		0.7	1.0	94.3	96.9	97.5	98.1	97.9
		0.7	1.4	110.9	115.8	117.7	119.3	119.6
		0.7	2.0	137.6	146.8	149.8	153.2	154.8
		0.8	1.0	94.5	97.3	98	98.9	98.6
		0.8	1.4	112.3	118	120.3	122.3	122.6
		0.8	2.0	152.5	165.5	171.3	175.5	176.5
		0.9	1.0	92.9	95.6	96.3	97.1	96.9
		0.9	1.4	112.1	117.7	120.3	122.6	122.9
		0.9	2.0	153.4	167.3	173.8	178.7	179.7
		0.9*	1.0	107.2	111.2	112.3	113.3	112.9
		0.9*	1.4	133	142.7	147	150.5	150.8
		0.9*	2.0	187	207.7	218.5	227	228.5
DP60-FE	0.6	β_2	τ_2	η_2				
				0.8	1.0	1.2	1.6	2.0
		0	0	98.3				

		0.9	1.0	157.5	165	167.8	168.8	169.5
		0.9	1.4	182.8	196	202.7	206.7	208.3
		0.9	2.0	236.6	260.2	275.3	284.8	287.9
		0.9*	1.0	179.8	190.8	195.2	196.6	197.1
		0.9*	1.4	214.3	232.8	243.5	249.7	251.6
		0.9*	2.0	280	310.8	330.3	343.2	351.1
DP80-FE	0.8	β_2	τ_2	η_2				
				0.9	1.0	1.2	1.6	2.0
		0	0	165.6				
		0.9	1.0	273.4	282.9	291.2	294.8	296
		0.9	1.4	286.4	300.4	316.1	325.9	329
		0.9	2.0	309.5	330.3	361.4	383.2	389.7
		0.9*	1.0	301.6	314.9	326.9	333.9	334.6
		0.9*	1.4	315.6	336.6	357	372.5	377.1
		0.9*	2.0	333.1	357.6	403.6	432.6	441.7

The influence of doubler-plate geometry and material on the reinforcing efficiency is shown in Figure 11. It can be seen from Figure 11(a) the width of doubler-plate has little influence on the reinforcing efficiency of joint when the thickness of doubler-plate was fewer than 1.4 t_0. However, as the thickness of doubler-plate was 2.0 t_0, the reinforcing efficiency increased with the increase of doubler-plate width. For construction convenience, the width of doubler-plate can be determined equal to the flat width of the chord flange (ie. b_0-4t_0), which was consistent with that proposed by Korol [14] or CIDET [21].

It is common the thicker of the doubler-plate, the stronger of the DPR joint [14]. However, the situation was contrary for reinforcing efficiency, which decreased significantly as the thickness of doubler-plate increased, as shown in Figure 11(b). For example, for the joint with β=0.4, β_2=0.9 and η_2=1.0, as τ_2 increased from 1.0 to 1.4 and 2.0, the reduction of R_E were 19.7% and 28.4%, respectively. Similarly, the reduction were 25.3% and 39.3% for joint with β=0.6, and 41.4% and 64.9% for joint with β=0.8. Thus, the use of large thickness doubler-plate was unnecessary, and a thickness ratio for doubler-plate and chord under 2.0 was appreciated.

From Figure 11 (b), it can also be seen the influence of doubler-plate thickness increased as the width ratio increased. For example, for the joint with τ_2=1.0, β_2=0.9 and η_2=1.0, as β increased from 0.4 to 0.6 and 0.8, the increase of R_E were 73.2% and 204.7%, respectively. However, a width ratio of under 0.8 was more appropriate for the application of doubler-plate reinforcement, for the reason of fabrication convenience.

The reinforcing efficiency increased with the increase of the doubler-plate length, as shown in Figure 11(c). For example, for the joint with β=0.4, β_2=0.9 and τ_2=1.0, as η_2 increased from 0.8 to 1.0, 1.2, 1.6 and 2.0, the increase of R_E were 7.5%, 9.5%, 11.7% and 11.2%, respectively. Similarly, the increase were 12.7%, 17.4%, 19.1% and 20.3% for joint with β=0.6, and 8.9%, 16.5%, 19.9% and 21% for joint with β=0.8. For all the joints analyzed, it was interesting that the increase of R_E trends to be slowdown when η_2 exceed 1.6, demonstrating an optimal range of doubler-plate length existed (Korol [14]).

It can be seen from Table 5 the strength of DPR joint increased with the increase of doubler-plate yielding strength. Nevertheless, the reinforcing efficiency decreased slightly, as shown in Figure 11(d). For example, for the joint with β=0.4, β_2=0.9, η_2=1.0 and τ_2=1.0, as f_{y2} increased from 235 to 345, the reduction of R_E were 7.4%. Similarly, the reduction were 5.5% and 13.3% for joint with

β=0.6 and β=0.8. Therefore, it was unnecessary to use high strength steel for doubler-plate. The yielding strength of the doubler-plate can be the same as or even less than the chord.

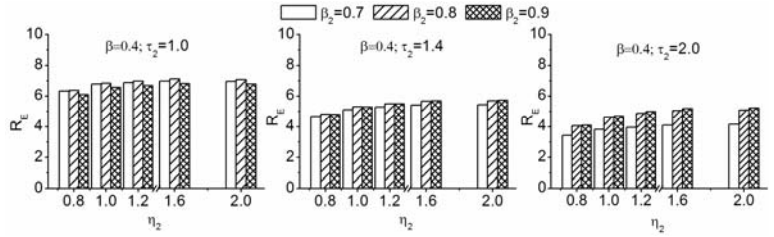

(a) Influence of doubler-plate width on R_E

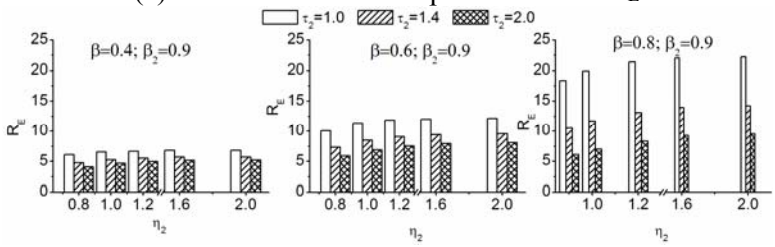

(b) Influence of doubler-plate thickness on R_E

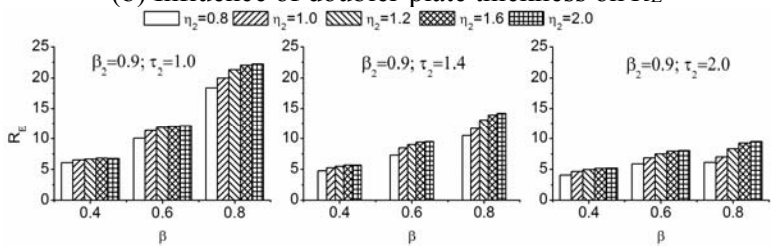

(c) Influence of doubler-plate length on R_E

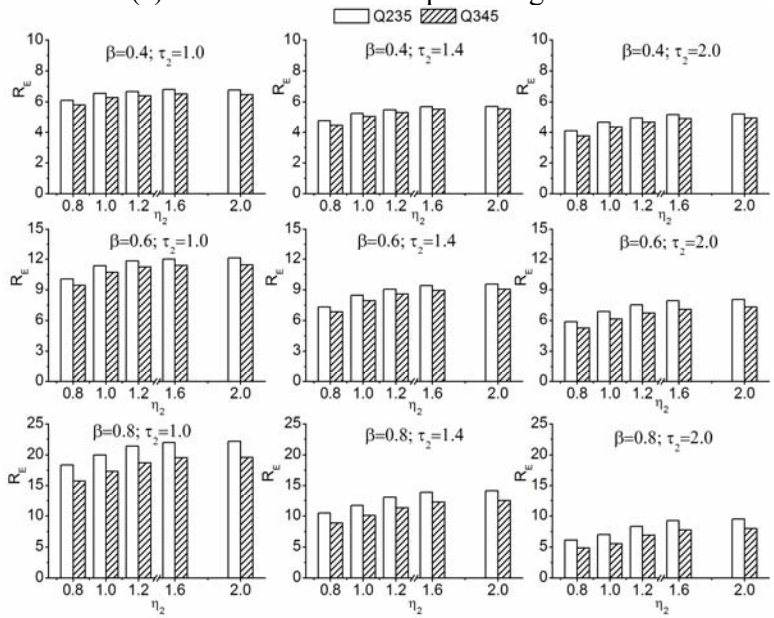

(d) Influence of doubler-plate yielding strength on R_E

Figure 11. Influence of Doubler-plate Parameters on the Reinforcing Efficiency of Joint

4. ANALYTICAL INVESTIGATION ON COMPRESSION STRENGTH OF DPR-SHS T-JOINTS

In this section, the reinforcement mechanism of doubler-plate is analyzed. The stress distribution of the unreinforced or reinforced joints is compared firstly, and then the compression strength of the joint is analyzed with yielding line method.

4.1 Stress Distribution of DPR-SHS Joints

The equivalent Von Mises stress contours of unreinforced or DPR-SHS T-joints are shown in Figure 12. It can be seen the stress distribution of the chord for DPR-SHS joint consistent well with the unreinforced one. The doubler-plate deformed and yielded together with the chord flange under brace compression load, had very little influence on the stress distribution of the chord. Further more, when the displacement of the brace was equal to 3%b_0, the stress distribution along the centerline or edge-line of the chord flange was picked and pictured in Figure 13. The stress distribution of the chord flange for DPR-SHS joints was almost the same as unreinforced ones, and the length of yielding zone on chord flange remained unchanged with the increase of η_2.

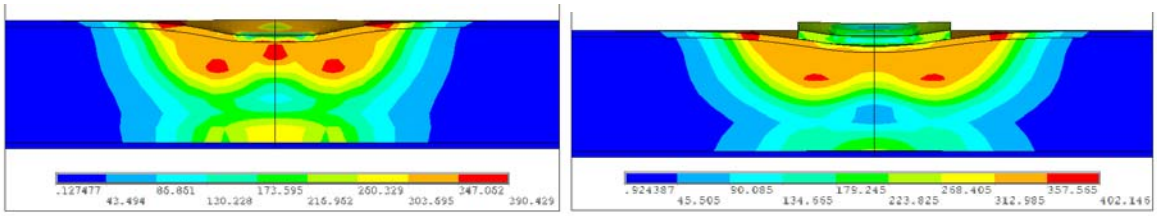

(a) unreinforced joint, (b) DP60-FE (τ_2=1.4; β_2=0.9; η_2=1.2)

Figure 12. Comparison of Equivalent Stress Contours

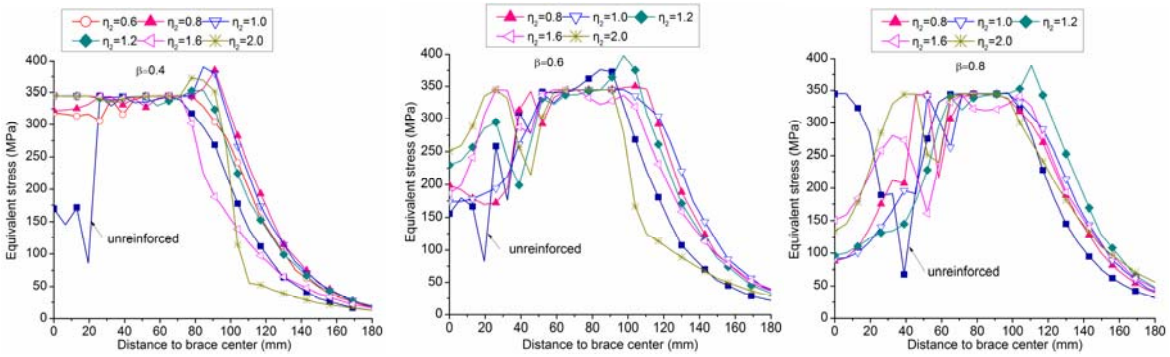

(a) center-line of the chord surface

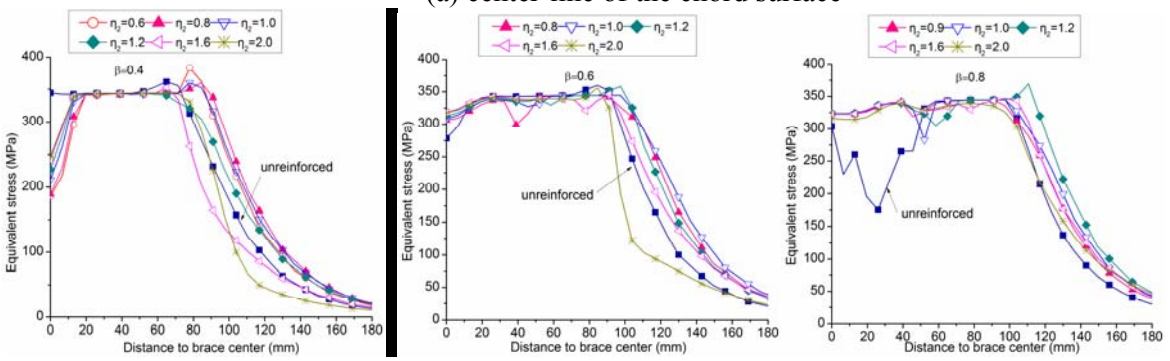

(b) edge-line of the chord surface

Figure 13. Equivalent Stress Distribution of the Chord Surface

4.2 Yielding Line Analysis

Both the experimental tests and finite element simulations indicated the doubler-plate improves the compression strength of the joint obviously, yet does not change the behaviors (namely: failure mode, stress distribution or yielding zone) of the joint. Therefore, the yielding line theory is adopted to estimate the compression strength of the DPR-SHS T-joint in this section. For an unreinforced SHS T-joint under brace compression, a set of yielding lines may develop on the chord flange when the failure of surface yielding controlled, as shown in Figure 14(a). The strength of the joint is (EC3 [20]):

$$P_{y0} = \frac{2 f_{y0} t_0^2}{1-\beta}\left(\frac{h_1}{b_0} + 2\sqrt{1-\beta}\right) \tag{2}$$

In which f_{y0} is the yielding strength of the chord, $\beta=b_0/b_1$ is the width ratio of the brace and the chord. The rest of the symbols are the same as shown in Figure 1.

As discussed before, the doubler-plate improved the compression strength of the joint by deforming and yielding together with the surface of the chord. However, the yielding lines on the doubler-plate may different, when the length of the doubler-plate increased (Korol [14]) progressively as shown in Figure 14 (b)-(d). By assuming the yielding pattern of the chord flange unchanged by the doubler-plate, the yielding lines on the doubler-plate can be drawn as the thick solid lines in Figure 14 (b)-(d). Table 6 lists the length and quantity of each yielding line of the DPR-SHS joint. Then the nominal compression strength of the DPR-SHS T-joint can be expressed as:

$$P_{y-dp1} = P_{y0} + \frac{f_{y2} t_2^2}{(b_0 - b_1)}\left[h_1 + h_2 + (b_1 + b_2)\sqrt{1-\beta} + (h_2 - h_1)(2-\beta)\right] \tag{3}$$

$$P_{y-dp2} = P_{y0} + \frac{f_{y2} t_2^2}{(b_0 - b_1)}\left[h_1 + h_2 + (b_2 + b_1)\sqrt{1-\beta} + \frac{(b_2 - b_1)(2-\beta)}{\sqrt{1-\beta}}\right] \tag{4}$$

$$P_{y-dp3} = P_{y0} + \frac{f_{y2} t_2^2}{(b_0 - b_1)}\left[2h_1 + (b_0 - b_1)/\sqrt{1-\beta} + (b_2 + b_1)\sqrt{1-\beta} + (b_2 - b_1)(2-\beta)/\sqrt{1-\beta}\right] \tag{5}$$

In which P_{y0} is the strength of unreinforced joint, $P_{y\text{-}dp1}$, $P_{y\text{-}dp2}$ and $P_{y\text{-}dp3}$ is the ultimate compression strength corresponds to the situation of b, c and d in Figure 14 respectively, f_{y2} is the yielding strength of the doubler-plate. The rest of the symbols are the same as shown in Figure 1.

Note Eq.3 - Eq. 5 were based on the assumption of chord surface yielding failure mode controlled. However, the chord web buckling or brace buckling may occur when the chord flange was "over-reinforced" by doubler-plate, as has been proved in the laboratory test (Figure 3) and FE simulation (Figure 8). Therefore, the ultimate compression strength of DPR-SHS joints should be checked by the failure strength of chord web buckling and brace buckling.

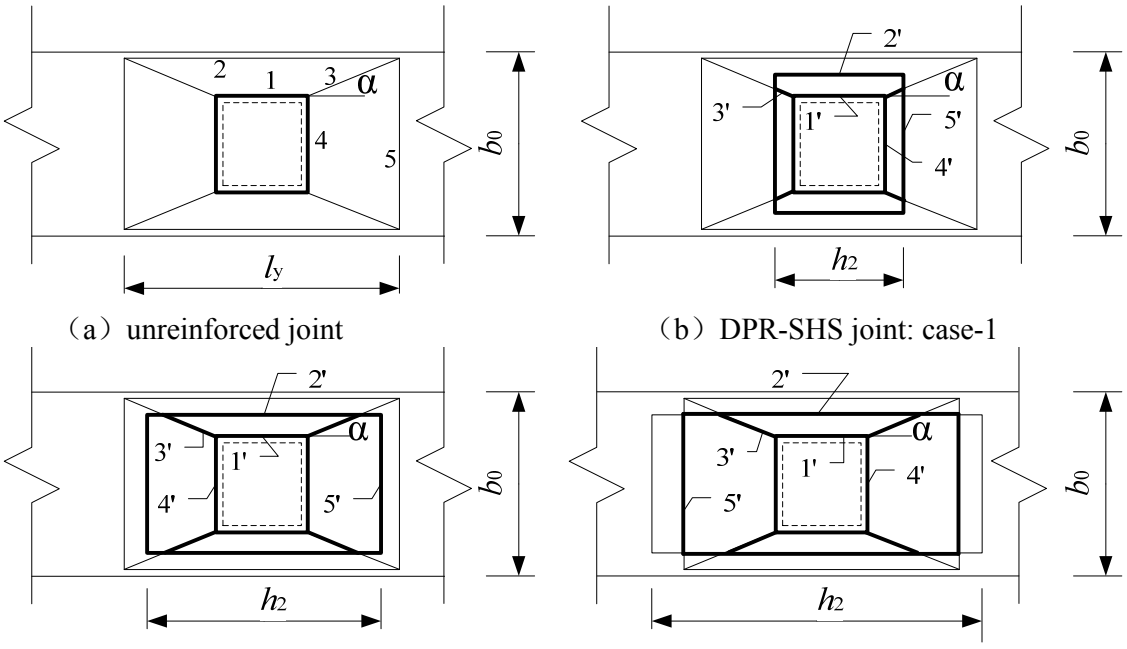

（a）unreinforced joint （b）DPR-SHS joint: case-1

（c）DPR-SHS joint: case-2 （d）DPR-SHS joint: case-3

Figure 14. Yielding Lines of the Chord Surface or Doubler-plate

Table 6. Length and Quantity of Yielding Lines on Doubler plate

No	quantity	Case-1 $h_2 \le h_1 + (b_2 - b_1)\cot\alpha$	Case-2 $h_1 + (b_2 - b_1)\cot\alpha \le h_2 \le h_1 + (b_0 - b_1)\cot\alpha$	Case-3 $h_1 + (b_0 - b_1)\cot\alpha \le h_2$
1’	2	h_1	h_1	h_1
2’	2	h_2	h_2	$h_1 + (b_0 - b_1)\cot\alpha$
3’	4	$\frac{(h_2 - h_1)}{2\cos\alpha}$	$\frac{(b_2 - b_1)}{2\sin\alpha}$	$\frac{(b_2 - b_1)}{2\sin\alpha}$
4’	2	b_1	b_1	b_1
5’	2	b_2	b_2	b_2

To check the accuracy of the proposed formulas, the FEA compression strength of the DPR-SHS T-joints, as well as the formula predicted values are plotted in Figure 15. Meanwhile, the strength calculated by Korol [14], Soh [16] and EC3 [20] are plotted for comparison.

The formulas of Korol [14] were proposed by theoretical derivation, and no verification tests were conducted for DPR-SHS T-joint under brace compression, which seems to have overestimated the compression strength of DPR-SHS T-joint. Soh [16] analyzed the compression strength of doubler-plate reinforced T-joint by experimental test and finite element parametric study, and proposed the strength formula by regression analysis. However, the influence of doubler-plate geometry was not included by Soh [16], which leading to an underestimation of the strength for DPR-SHS T-joint. In contrast, the accuracy of EC3 [20] and Eq. 3 - Eq. 5 was more satisfactory.

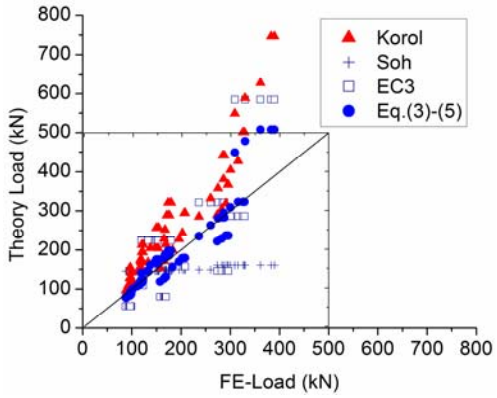

Figure 15. Comparison of Theory and FEA Determined Compression Strength

Furthermore, a detailed comparison between EC3 and Eq. 3 - Eq. 5 is demonstrated in Figure 16. The vertical axes P_{TH}/P_{FE} indicates the ratio of compression strength determined by formulas (EC3 or Eq.3-5) and FEA, the closer of P_{TH}/P_{FE} to 1.0, the more accurate of the formula. Note EC3 [20] determines the compression strength of DPR-SHS joints by replacing t_0 with t_2 in Eq. 2, neglects the influence of the doubler-plate parameters variety. The ratio of P_{TH}/P_{FE} for EC3 is relatively discrete. When the thickness of the doubler-plate is small (namely: τ_2=1.0), the code of EC3 [20] underestimates the compression strength of DPR-SHS joint about 40%-50%. However, an overestimate of 20%-80% by EC3 [20] is demonstrated for the joint with thick doubler-plate (namely: τ_2=2.0) or high width ratio (namely: β=0.8). Overall, the mean ratio of P_{TH}/P_{FE} for EC3 [20] is 0.97 with a COV of 0.15.

The accuracy of Eq. 3- Eq. 5 is more satisfactory, with a mean P_{TH}/P_{FE} ratio of 0.99 and a COV of 0.02. Most of the P_{TH}/P_{FE} ratios range from 0.8 to 1.2, demonstrating a very good convergence. However, the compression strength of the joint may be overestimated when the width ratio of the joint is 0.8. This mainly due to the failure of chord web buckling (Figure 10b) occurred, which prevent the full development of doubler-plate yielding.

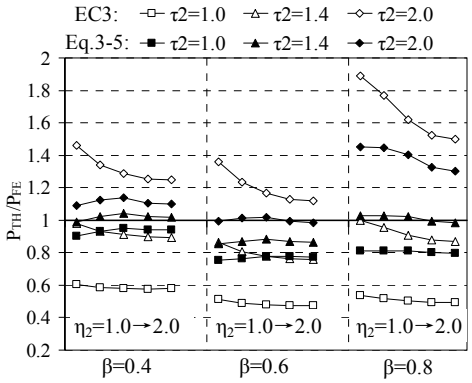

Figure 16. Comparison of EC3 and Eq. 3-5

5. CONCLUSIONS AND RECOMMENDATIONS

Effects of doubler-plate reinforcement on the compression behavior of square tubular T-joint were studied by laboratory tests and finite element analysis. The influence of doubler-plate geometry and material was discussed, and the mechanism of doubler-plate reinforcement was investigated. Finally, an analytical method was proposed to predict the nominal compression strength of DPR-SHS T-joints. Given the results presented in this study, the following conclusions can be drawn:

(1) Welding a doubler-plate on the surface of the chord provides a significant improvement in the compression strength of the SHS joint, yet does not change the stress distribution of the chord flange. Given a proper geometry, the reinforcement mechanism of doubler-plate is yielding together with the chord flange.

(2) The strength of a DPR-SHS joint can be significant improved by increasing the doubler-plate thickness, while insignificant by increasing the width or length of doubler-plate. However, it should be emphasized the failure of web or brace buckling may occur if the thickness exceeds a certain range.

(3) The reinforcement efficiency of the doubler-plate increased with the increase of doubler-plate width (β_2) and length (η_2), yet decreased with the increase of doubler-plate thickness (τ_2) and yielding strength (f_{y2}).

(4) Yielding line method is still valid to develop a theoretical model for the nominal compression strength of DPR-SHS joints, and the theoretical results agree well with the experimental and FE findings. While for design purpose, the theoretical strength should always be checked for possible web buckling or member failure.

For the application of doubler-plate reinforcement under brace compression, a width ratio of $\beta<0.8$ is appropriate, to avoid the problem of "over-reinforcement" as well as "fabricate difficulty". Based on the above analysis, the width, length and thickness of the doubler-plate can be determined as: β_2=1-4 t_0/b_0, $1.5\leq\eta_2\leq2.0$, $1.0\leq\tau_2<2.0$. The yielding strength of doubler-plate can be determined according to the strength requirement of the joint, a high strength doubler-plate was unnecessary.

For the design of DPR-SHS joints, the EC3 [20] seems to have over-simplified the compression strength estimation of DPR-SHS joints. By considering the co-yielding of the doubler-plate and the chord flange, as well as the influence of the doubler-plate parameters variety, the compression strength of DPR-SHS joints was more accurately estimated. However, the recommended formulas should be confirmed with more test or FEM evidences, and the simplification of the formulas is also needed, both of which will complete in the next stage.

ACKNOWLEDGMENTS

Thanks to the financial support of the National Science Foundation (51274192), the Jiangsu Civil Engineering Graduate Center for Innovation and Academic Communication foundation, the Jiangsu Province Science Foundation (BK20140195), the priority academic program development of Jiangsu higher education institutions and the Fundamental Research Funds for the Central Universities (2011QNB17).

REFERENCES

[1] Wardenier J., "Hollow Sections in Structural Application", Delft: Delft University Press; 2001.

[2] Lesani, M., Bahaari, M.R. and Shokrieh, M.M., "Detail Investigation on Un-stiffened T/Y Tubular Joints Behavior under Axial Compressive Loads", J. Const. Steel Res. 2013, Vol. 80, pp. 91–9.

[3] Packer, J.A. and Henderson, J.E., "Hollow Structural Section Connections and Trusses-A Design Guide, 3rd ed.", Toronto: Canadian Institute of Steel Construction; 1997.

[4] Shao, Y.B., Li, T., Lie, S.T. and Chiew, S.P., "Hysteretic Behaviour of Square Tubular T-joints with Chord Reinforcement under Axial Cyclic Loading", J. Constr. Steel Res. 2011, Vol. 67, No. 1, pp. 140-9.

[5] Nazari, A., Guan, Z., Daniel, W.J.T. and Gurgenci, H., "Parametric Study of Hot Spot Stresses Around Tubular Joints with Doubler Plates", Pract. Period Struct. Des. Constr. 2007, Vol. 12, No. 1, pp. 38-47.

[6] Soh, C.K., Chan, T.K., Fung, T.C. and Nakacho, K., "Stress Concentration Factors of Reinforced Square Hollow Section T-joints", Trans. JWRI 2001, Vol. 30, No. 2, pp. 103-08.

[7] Lee, M.M.K. and Llewelyn-Parry, A., "Offshore Tubular T-joints Reinforced with Internal Plain Annular Ring Stiffeners", J. Struct. Eng., 2004, Vol. 130, No. 6, pp. 942-51.

[8] Hoon, K.H., Wong, L.K. and Soh, A.K., "Experimental Investigation of a Doubler-plate Reinforced Tubular T-joint Subjected to Combined Loadings", J. Constr. Steel Res. 2001, Vol. 57, No. 9, pp. 1015–39.

[9] Choo, Y.S., Vegte, G.J., Zettlemoyer, N. and Li, B.H., "Static Strength of T-Joints Reinforced with Doubler or Collar Plates. I: Experimental Investigations", J. Struct. Eng. 2005, Vol. 131, No. 1, pp. 119-28.

[10] van der Vegte, G.J., Choo, Y.S., Liang, J.X., Zettlemoyer, N. and Liew, J.Y.R., "Static Strength of T-Joints Reinforced with Doubler or Collar Plates. II: Numerical Simulations", J. Struct. Eng., 2005, Vol. 131, No. 1, pp. 129-38.

[11] Fung, T.C., Chan, T.K. and Soh, C.K., "Ultimate Capacity of Doubler-plate Reinforced Tubular Joints", J. Struct. Eng. 1999, Vol. 125, No. 8, pp. 891-9.

[12] Choo, Y.S., Liang, J.X., Van Der Vegte, G.J. and et al., "Static Strength of Doubler Plate Reinforced CHS X-joints Loaded by In-plane Bending", J. Const. Steel Res. 2004, Vol. 60, No. 12, pp. 1725-44.

[13] Feng, Q. and Tan, J.H., "The Ultimate Strength of Doubler Plate Reinforced Y-joints under Compression Loading", J. Mar Sci. Appl., 2005, Vol. 4, No. 2, pp. 13-19.

[14] Korol, R.M., El-Zanaty, M. and Brady, F.J., "Unequal Width Connections of Square Hollow Sections in Vierendeel Trusses", Can J. Civ. Eng., 1977, Vol. 4, No. 2, pp. 190-201.

[15] Korol, R.M., Mitri, H. and Mirza, F.A., "Plate Reinforced Square Hollow Section T-joints of Unequal Width", Can J. Civ. Eng., 1982, Vol. 9, No. 2, pp. 143-8.

[16] Soh, C.K., Chan, T.K., Fung, T.C. and Nakacho, K., "Ultimate Capacity of Doubler Plate Reinforced Square Hollow Section T-joints", Trans JWRI 2000, Vol. 29, No. 2, pp. 85-90.

[17] Yang, J., Shao, Y.B. and Chen, C., "Static Strength of Chord Reinforced Tubular Y-joints under Axial Loading", Mar Struct. 2012, Vol. 29, pp. 226-45.

[18] Lesani, M., Bahaari, M.R. and Shokrieh, M.M., "Numerical Investigation of FRP-strengthened Tubular T-joints under Axial Compressive Loads", Comp. Struct. 2013, Vol. 100, pp. 71-8.

[19] Jose, A. and Amir, F., "Retrofitting Tubular Steel T-joints Subjected to Axial Compression in Chord and Brace Members using Bonded FRP Plates or Through-wall Steel Bolts", Eng. Struct., 2013, Vol. 48, pp. 602-10.

[20] European Committee for Standardisation: 2003 European Standard, Design of Steel Structures: Design of Joints.
[21] CIDET: 2009 Design Guide For Rectangular Hollow Section (RHS) Joints Under Predominantly Static Loading.
[22] Wu, Z.Y., Chen, P. and Wang, Y.Y., "Experimental Study on the Hysteretic Behavior of T-type SHS Joints", Chin Civ. Eng. J., 2008, Vol. 41, No. 12, pp. 8-13. (in Chinese)
[23] Chang, H.F., Xia, J.W. and Zhang, F.J., "The Static Performance of Axially Loaded, Square Tubular T-joints", J CUMT 2012, Vol. 41, No. 6, pp. 917-22 (in Chinese)
[24] Lu, L.H., Winkel, G.D., Yu, Y. and Wardenier, J., "Deformation Limit for the Ultimate Strength of Hollow Section Joints" In: Paul Grundy, Alan Holgate editors. Tubular Structures VI. London: Taylor & Francis Group, 1994, pp. 341-7.
[25] Zhao, X.L., "Deformation Limit and Ultimate Strength of Welded T-joints in Cold-formed RHS Sections", J. Constr. Steel Res. 2000, Vol. 53, No. 2, pp. 149-65.

A NUMERICAL STUDY ON THE EFFECT OF CONCRETE INFILL AND INTUMESCENT COATING TO FIRE-RESISTANT BEHAVIOUR OF STUB ELLIPTICAL STEEL HOLLOW SECTIONS UNDER AXIAL COMPRESSION

X.H. Dai [1] and D. Lam [2, *]

[1] *Lecturer, School of Engineering Design and Technology, University of Bradford, Bradford, BD7 1DP, UK*
[2] *Professor, School of Engineering Design and Technology, University of Bradford, Bradford, BD7 1DP, UK*
**(Corresponding author: E-mail: d.lam1@bradford.ac.uk)*

Received: 24 March 2013; Revised: 3 July 2013; Accepted: 24 September 2013

ABSTRACT: This paper presents a numerical study on the effect of concrete infill and intumescent coating to the fire resistant behaviour of stub elliptical concrete filled steel tubular (CFST) columns under standard fire. The selected elliptical steel hollow sections in this research cover the common used elliptical sections in current construction market; from 200 × 100 mm to 500 × 250 mm with wall thicknesses varying from 5 to 12.5 mm. Temperature distribution, critical temperature and fire exposing time of selected stub elliptical columns with concrete infill and other intumescent coating fire protection options under axial compression were extracted from numerical simulations using commercial FE package ABAQUS. Based on the comparison and analysis of the obtained results, the effect of concrete core and external intumescent coating to the thermal and structural fire-resistant behaviour of stub elliptical columns are discussed. Simple formulae are proposed to assess the critical steel temperature and maximum axial compressive load of stub elliptical CFST columns in standard fire.

Keywords: Elliptical hollow section, temperature development, critical temperature, fire exposing time, concrete infill, intumescent coating, numerical modelling

1. INTRODUCTION

There are many forms of fire protection methods which may apply to structural steel and composite structures to promote their fire resistance ability. Applying intumescent coating is one of the commonly used methods although the intumescent coatings themselves do not provide any enhancement to the structural capacity. Due to the inert property of concrete and its poor thermal conductivity, it could be smartly deployed to provide fire resistance to the steel members and offered additional load resistance. When a CFST column is subjected to fire, the concrete core acts as a heat sink and this resulted in a reduction in steel temperature when comparing with an equivalent unfilled steel hollow section subjected to the same fire exposure. Because of the concrete temperature rises much slower than that of the steel tube, the concrete core could provide appropriate load bearing capacity even when the steel tube reached its capacity. In many situations when higher fire resistance period is required, using steel hollow sections even with concrete infill cannot meet the fire resistant requirement; therefore intumescent coating or other forms of external fire protection to the steel members may be used to enhance the fire resistance.

Previous researches carried out on CFST members exposed to fire by experimental studies and numerical methods have provided some important insights into structural fire behaviour of this kind of steel concrete composite members (Tao et al. [1], Han and Lin [2], Han et al. [3], Huo et al. [4], Zha [5], Hong and Varma [6], Espinos et al. [7 – 8]). However for the unprotected CFST columns in standard fire, Dai and Lam [9] showed that the temperature of steel section rises quickly within a short exposure time and reached the critical design temperature, this suggests that additional

measurement such as external fire protection or fire shading is required to improve the fire resistance in practice. Applying intumescent coating is an effective method to reduce the steel temperature development (Corus Construction & Industrial [10]). The intumescent coating provided by different suppliers might be with different properties and performance, such as different dry film thickness and fire protection time etc. Dai et al. [11, 12] investigated the thermal behaviour of steel joint assemblies with a typical intumescent coating (cellulosic solvent based) and the results illustrated that the intumescent coating provided an excellent property in impeding the temperature development of steel members in fire.

In active fire resistance design, the critical temperature and critical exposing duration of a structural member are the most important design parameters. They might be affected by many factors such as building type, occupancy, loading, geometry and material properties etc. For CFST columns with same loading ratio and boundary conditions, the member material properties and geometrical characteristics will dominate these design parameters. The main objective of this research is to investigate the effect of intumescent coating and concrete infill to fire resistance of elliptical stub CFST columns with various elliptical hollow section dimensions and intumescent coating; it focused on comparison and analysis of temperature development, critical temperature and fire exposure time of elliptical stub CFST columns with a fixed load ratio. The critical temperature defined in this paper is defined as the average steel tube temperature in which the steel material reached its yield strength at the prescribed load ratio above which the column will experience a progressive deformation. The prescribed load ratio of elliptical stub columns in fire is assumed to be 0.5 which is closed to the design load ratios (0.47 and 0.66) provided in EN1994-1-2 [13] for CFST columns with circular and rectangular sections. The critical fire exposing time is defined as the fire period when the steel tube reached its critical temperature.

2. ELLIPTICAL SECTIONS AND FIRE PROTECTION OPTIONS

For unprotected CFST members with different sectional shapes, such as circular (CHS), elliptical (EHS), square (SHS) and rectangular (RHS) shapes in standard fire, the temperature distribution in steel cross-section is not uniform. The maximum difference in temperature may be up to 70 ºC when exposed to a standard ISO fire (ISO 834 [14]) for 60 minutes, with the exception for CHS where the temperature difference is less than 4 ºC. The non-uniformity of temperature distribution of steel section changes with the different section shapes and dimensions. The study carried out by Dai and Lam [9] showed that the compressive behaviour of elliptical stub CFST columns in fire is not as good as composite columns with circular sections but better than columns with square and rectangular sections due to the circular hollow sections provide better confinement effect to concrete core and less stress concentration. This research is to investigate the effect of intumescent coating and concrete infill to the fire resistant behaviour of elliptical steel hollow sections without reinforcement in the concrete core.

To investigate the effect of intumescent coating for fire protection to elliptical stub CFST columns, thermal analysis (heat transfer) and stress-strain analysis (both in ambient and elevated temperature) were performed for 9 selected column specimens with 6 fire protection options. These selected stub specimens covered the section sizes ranges from 200×100mm to 500×250mm with various wall thicknesses from 5.0 to 12.5mm. The fire protection options included different intumescent coating dry film thicknesses (0.0, 1.0, 1.5 and 2.0mm). In addition, unfilled elliptical steel hollow sections in fire are also compared with elliptical CFST columns to investigate the effect of the concrete infill.

3. MATERIAL PROPERTIES

It is well understood that the mechanical and thermal properties of steel and concrete are very different in fire design. Steel is recognized as a highly thermal conductive material to concrete although the strength and stiffness of both steel and concrete will reduce as the temperature increases. In this paper, all steel hollow sections are assumed to be hot finished. As aforementioned, the aim of this research is to investigate the effect of intumescent coating and concrete infill to the structural fire-resistant behaviour of CFST columns; therefore, identical steel material properties were adopted for the selected steel hollow sections to eliminate the influence of the steel material properties. In addition, the concrete infill for all the composite columns was assumed to be identical.

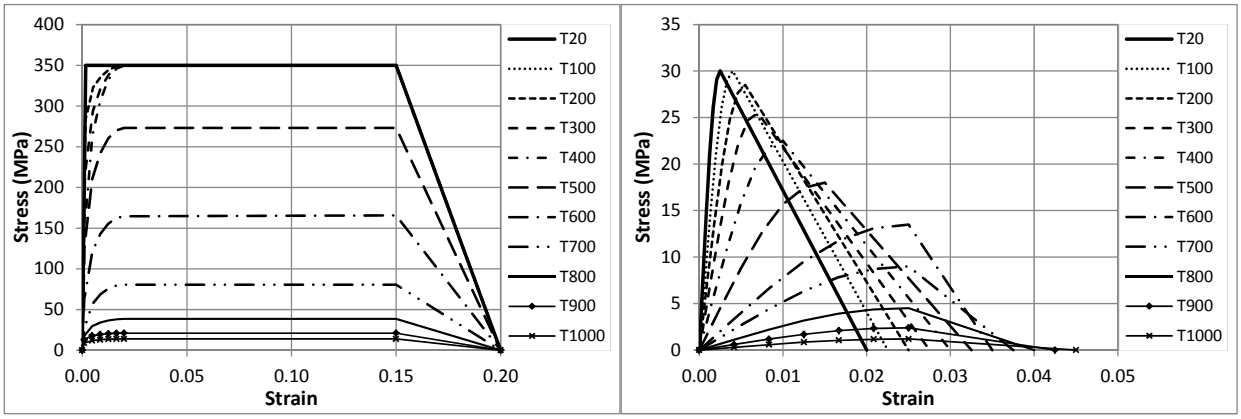

(a). Steel (b). Concrete

Figure 1. Stress-strain Curves of Steel and Concrete at Elevated Temperatures

The stress-strain curve of steel material at room temperature (20 ºC) is defined by T_{20} curve in Figure 1(a). The yield strength, f_y and elastic modulus, E_s was assumed to be 350 N/mm^2 and 210000 N/mm^2 respectively for all the steel hollow sections. The reduction factors for strength and deformation of steel material at elevated temperatures is in accordance to the EN1993-1-2 [15] for carbon steel and as shown in Figure 1(a). The maximum compressive strength of concrete f_c and corresponding strain ε_c was assumed to be 30 N/mm^2 and 0.003 respectively. In Figure 1(b), the T_{20} curve represents the stress-strain relationship of concrete at room temperature. The reduction factors for concrete strength and deformation at elevated temperatures is in accordance to EN1994-1-2 and Figure 1(b) shows the stress-strain curves at all the different temperatures. The thermal properties of both steel and concrete were in accordance to the thermal properties of carbon steel and normal weight concrete given in the EN1993-1-2 and EN1994-1-2 and as shown in Figure 2, the moisture content of the concrete was assumed to be zero. The thermal conductivity of the intumescent coating (Figure 2a) is taken to be the average value of those extracted from the experiments carried out by Dai et al. [12]. The specific heat of the intumescent coating was assumed to be 1000 J/kg/K. The densities of steel, concrete and intumescent were assumed to be 7850kg/m^3, 2400kg/m^3 and 1300kg/m^3 respectively.

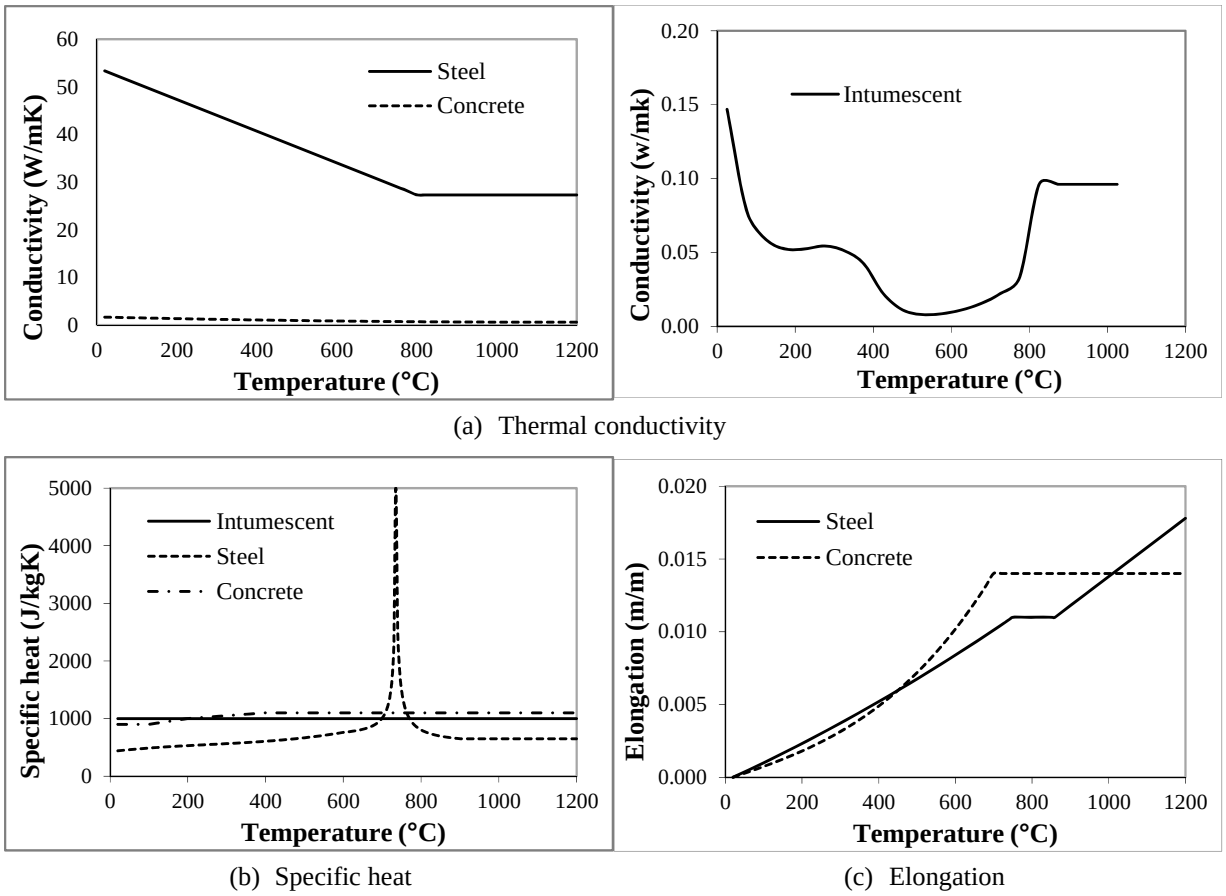

(a) Thermal conductivity

(b) Specific heat

(c) Elongation

Figure 2. Thermal Properties of Steel, Concrete and Intumescent Coating Adopted in this Research

4. NUMERICAL PROCEDURE

When a structural member subjected to fire, the heat flux will transfer through the member surface and increases the member temperature. In simple fire design for steel, the steel temperature is assumed to be uniformly distributed, however this assumption is not appropriate for CFST members due to the temperature difference in steel and concrete, therefore advanced heat transfer analysis is usually performed to determine the temperature distribution.

In the research presented in this paper, a non-linear heat transfer modelling developed using commercial software ABAQUS was used to determine the temperature distribution of each selected composite column under standard ISO fire. During the fire exposure, heat is transferred to the steel tube surface through convection and radiation and into the member through heat conductive mechanisms. In the modelling, the convective coefficient was taken to be $25W/m^2k$ as recommended in EN1991-1-2 [16] and the effective surface emissivity of 0.5 was used. For CFST columns in fire, it is possible that a gap will form between the steel hollow section and concrete core due to their different expansion. Research by Ding and Wang [17] indicated that introducing an air gap will give a higher fire resistance times than without a gap for CFST columns without external fire protection. However, for CFST columns with high degree of external fire protection, introducing an air gap might lead to prediction of lower column fire resistance period but the difference of fire resistance period is very small. In this study, to simplify the heat transfer analysis, the possible air gap between the steel tube and concrete core during fire was not taken into consideration; hence the heat flow may directly conduct from steel tube into the concrete core.

For column sections with intumescent coating, it was assumed that the intumescent coating thickness is uniform and effectively affixed to the steel surface. In the heat transfer analysis, the 3D heat transfer element was used for the intumescent. Due to the highly inert property of intumescent coating, which is very different from the steel material, therefore the element size and contact surface between the steel section and the coating is sensitive to the accuracy of the heat transfer analysis. A sensitivity study was carried out and the comparison is shown in Figure 3. It indicated that for the intumescent coating with dry film thickness less than 2.0mm, if the elements were dividing into 6 layers or more with the concrete and steel element size no more than 50mm, then the influence of element size to the steel and concrete temperature will be less than 10 °C and 5 °C respectively. Therefore, 6 layers of elements with element size of 50mm were adopted in the thermal analysis. The thermal properties of steel, concrete and intumescent shown in Figure 2 were used throughout.

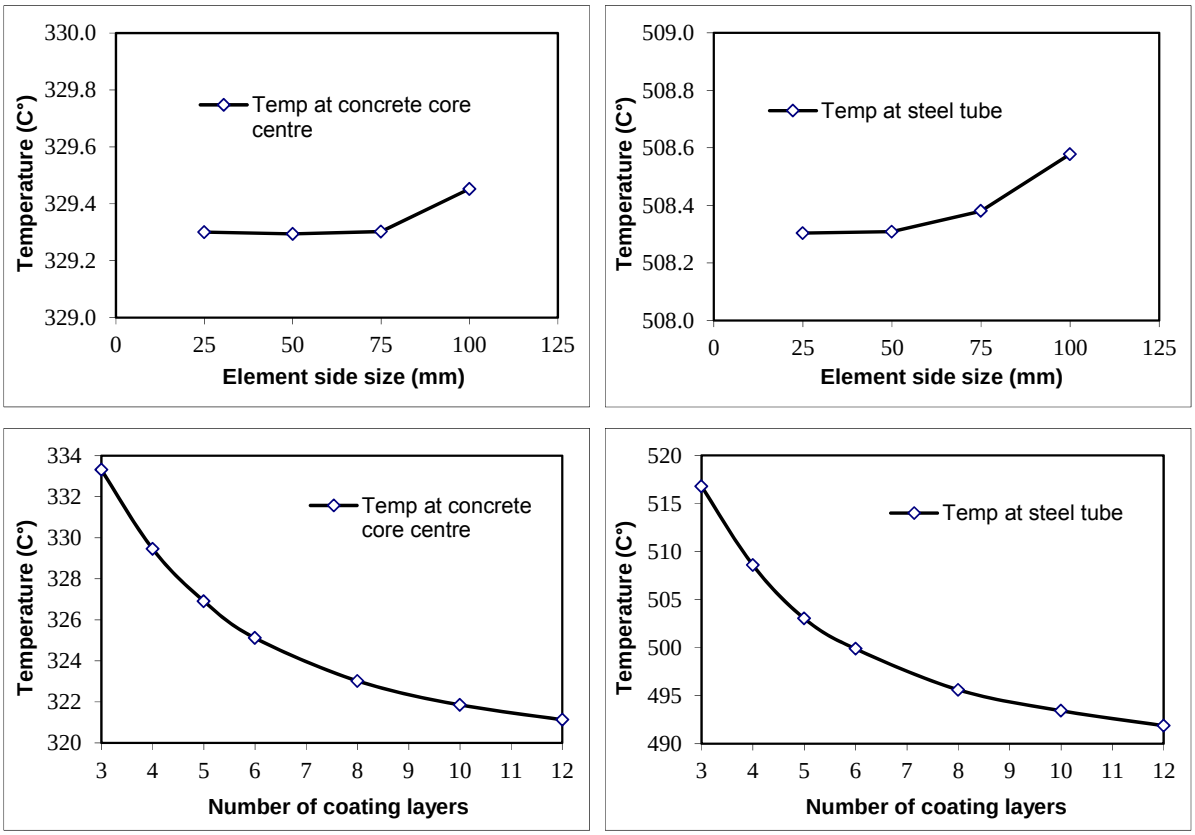

Figure 3. Element Size Sensitivity Comparison

5. TEMPERATURE DEVELOPMENT

The following abbreviations are adopted throughout this paper to specify the member individual features related to concrete infill and intumescent coating of the stub CFST columns:

US: unfilled steel hollow section without intumescent coating,
PS: unfilled steel hollow section with intumescent coating (dry film thickness 1.0 mm),
UP: CFST column without intumescent coating,
PP: CFST column with intumescent coating (dry film thickness 1.0 mm),
PPA: CFST column with intumescent coating (dry film thickness 1.5 mm),
PPB: CFST column with intumescent coating (dry film thickness 2.0 mm),

Figure 4(a) presents an example for temperature development in steel tube of selected columns with steel hollow section 200×100×10mm and different fire protection options mentioned above. It can be observed that with an unfilled steel hollow section without fire protection (US), the steel temperature rose rapidly reaching 600 °C in less than 15 minutes. When an equivalent steel hollow section was filled with concrete but without intumescent coating (UP), the steel temperature development was lower than the unfilled column (US) but higher than the unfilled section with intumescent coating protection (PS), however if the same steel hollow section with both infill concrete and intumescent coating (PP, PPA and PPB), the temperature development in steel tubes reduced significantly and is below 600 °C with the fire exposure time well beyond 60 minutes. Figure 4(b) shows that the temperature at the concrete core centre, it can be observed that the temperature in the centre of core of the composite column without intumescent coating (UP) is much higher than the temperatures in the centre of the CFST columns with intumescent coating (PP, PPA, PPB) owing to the intumescent coating blocking the heat flux to the composite columns.

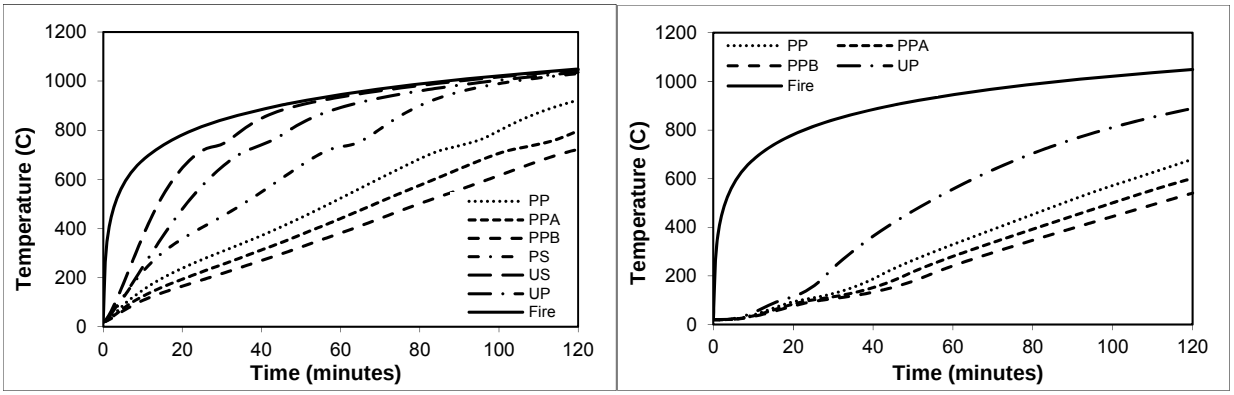

(a) Average temperature at steel tube (b) Temperature at core centre

Figure 4. Effect of Intumescent Coating and Concrete Core on
Temperature Development of Steel Hollow Section EHS200×100×10mm

For the other CFST columns with different wall thicknesses (5.0mm, 6.3mm, 8.0mm and 12.5mm) and different section dimensions (250×125×10mm, 300×150×10mm, 400×200×10mm and 500×250×10mm), similar temperature development curves were also extracted from the numerical modelling. In conclusion, the infill concrete helps to lower the temperature of CFST columns in fire; applying intumescent coating also significantly delay the temperature rise in steel hollow section and CFST columns. Table 1 summarizes the steel and concrete core temperatures for all selected columns at 60 and 120 minutes fire exposure.

From Table 1, these following conclusions may be drawn: (1) with the steel wall thickness increases, the steel temperature reduced and the core temperature increased. For the intumescent coating only steel hollow sections, the steel temperature reduced evidently with the increases in the wall thickness; (2) with the column section dimension increased from 200×100×10mm to 500×250×10mm, the steel temperature decreased slightly for the columns with intumescent coating, but the concrete core temperature reduced significantly.

Table 1. Temperature of Steel Tube and Concrete Core Centre at 60 Minutes and 120 Minutes Fire Exposing for Selected Columns

Fire Exposure time	Monitoring Location	Column section	Composite column conditions and temperature					
			US	PS	UP	PP	PPA	PPB
60 minutes	Steel tube	EHS200×100×5.0	*940*	*898*	*895*	567	474	410
		EHS200×100×6.3	*939*	*841*	*891*	544	464	401
		EHS200×100×8.0	*937*	*765*	*897*	539	452	392
		EHS200×100×10.0	*935*	*733*	*892*	524	440	381
		EHS200×100×12.5	*932*	*697*	*884*	508	427	370
		EHS250×125×10.0	*935*	*731*	*876*	496	417	357
		EHS300×150×10.0	*935*	*730*	*866*	475	397	340
		EHS400×200×10.0	*935*	*729*	*853*	453	376	322
		EHS500×250×10.0	*935*	*731*	*846*	439	365	313
	Concrete core	EHS200×100×5.0	-	-	519	313	267	229
		EHS200×100×6.3	-	-	529	317	270	232
		EHS200×100×8.0	-	-	542	323	275	237
		EHS200×100×10.0	-	-	558	329	280	241
		EHS200×100×12.5	-	-	575	338	287	248
		EHS250×125×10.0	-	-	389	218	177	152
		EHS300×150×10.0	-	-	265	138	124	115
		EHS400×200×10.0	-	-	117	92	84	78
		EHS500×250×10.0	-	-	79	56	52	48
120 minutes	Steel tube	EHS200×100×5.0	1047	1041	1036	955	879	771
		EHS200×100×6.3	1047	1039	1036	948	859	751
		EHS200×100×8.0	1046	1036	1036	938	832	734
		EHS200×100×10.0	1045	1031	1036	922	797	721
		EHS200×100×12.5	1044	1020	1036	900	763	703
		EHS250×125×10.0	1045	1030	1030	882	750	684
		EHS300×150×10.0	1045	1030	1025	842	724	641
		EHS400×200×10.0	1045	1029	1017	792	686	591
		EHS500×250×10.0	1045	1029	1013	773	660	565
	Concrete core	EHS200×100×5.0	-	-	849	675	599	539
		EHS200×100×6.3	-	-	859	677	599	539
		EHS200×100×8.0	-	-	873	678	599	540
		EHS200×100×10.0	-	-	889	679	601	540
		EHS200×100×12.5	-	-	908	682	606	542
		EHS250×125×10.0	-	-	738	532	472	422
		EHS300×150×10.0	-	-	588	411	363	323
		EHS400×200×10.0	-	-	357	226	187	162
		EHS500×250×10.0	-	-	193	123	116	109

6. STRUCTURAL FIRE RESISTANT BEHAVIOUR

After the temperature development curves (temperature vs. fire exposing time) under standard ISO fire were obtained through the thermal response analysis, a two-step stress-strain analysis is subsequently conducted to investigate the compressive behaviour of elliptical CFST stub columns. In the first step, a load corresponding to a load ratio of 0.5 (50% of the sectional capacity at ambient temperature) is applied to the top of the composite column at ambient temperature. This load is maintained during the second step in which the temperature vs. fire exposing time curves previously obtained from the thermal analysis is imported. In the stress-strain analysis, the interaction between the steel hollow section and concrete core in the normal direction followed the ‘‘hard” contact pair mechanism, which allows pressure to be transmitted when the surface pairs are in contact. For the interaction in the tangent direction, a friction coefficient of 0.3 is introduced to consider the composite interaction between the steel tube and the concrete core [7].

Espinos *et al* [7, 8] clearly described the deformation progress of long CFST columns under axial compressive load in fire. The deformation may be divided into four stages. The first stage is characterized by the expansion of the steel tube with the steel hollow section carrying the entire axial load applied to the composite column. The second stage starts when the steel section reached its yield stress at the elevated temperature and with the temperature raises further, the resistance of the steel hollow section decreases. The third stage is characterized by the concrete carrying the entire axial compressive load applied to the composite column due to the steel is yielded. The fourth stage begins with the reduction of the concrete strength due to the elevated temperature and leading to the complete composite column failed in fire. For the CFST stub columns, the four stages described by Espinos *et al.* were not clearly visible due to the expansion of stub column is relatively small. Therefore it would appear only two stages are observed for the stub column tests: expansion of the steel section followed by complete crushing at high temperature.

6.1 Critical Steel Temperature and Critical Fire Exposure Time

In this paper, the critical steel temperature is defined as the average steel temperature when the column experience progressive deformation and at which the steel material also reached its yield stress. The critical fire exposure time is the fire exposure time when the steel tube temperature reached the above mentioned critical steel temperature.

Figure 5 shows the typical relationships of axial shortening vs. fire exposing time and axial shortening vs. steel temperature for 200×100×10 EHS with various fire protection options. It can be observed from the curves, the critical fire exposure times are evidently different although the critical steel temperatures are close. Obviously, the critical fire time of steel hollow section (US) without intumescent coating and concrete infill is the shortest followed by the CFST column without intumescent coating (UP). Although the critical fire time of the intumescent coating protected steel hollow section column (PS) is much longer than the critical fire time of unprotected hollow steel hollow section columns (US and UP), it is much shorter comparing with the critical fire exposing times of intumescent coating protected CFST columns (PP, PPA and PPB). As expected, the thicker the intumescent coating, the longer the critical fire exposing time.

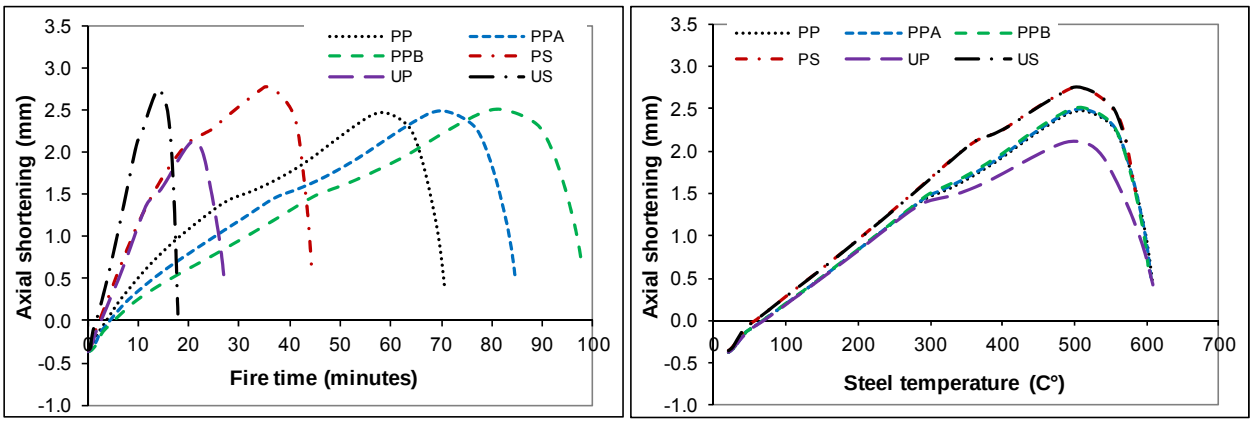

Figure 5. Relationships of Axial Shortening vs. Fire Exposing Time and Steel Tube Temperature for EHS200×100×10mm Hollow Sections with Different Intumescent Coating Thicknesses

Figures 6 and 7 present the effect of hollow section wall thickness and dimension to the critical fire exposing time and critical steel temperature. It can be seen in Figure 6 that with the steel wall thickness increases (A_s/A_c increase) but column outer dimension did not change, the critical fire time increases evidently but critical steel temperature remains unchanged. When the column section dimension increases (A_c/A_s increase), the critical fire exposing time increases evidently, but the critical steel temperatures remain the same. This indicates the merit of concrete infill and intumescent coating fire protection on structural fire behaviour of concrete filled steel stub columns under axial compression.

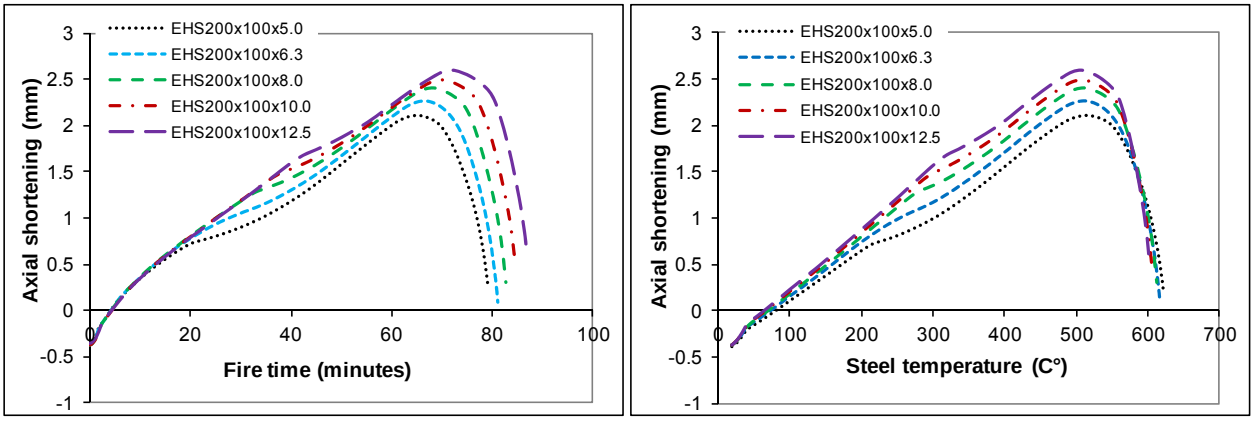

Figure 6. Relationships of Axial Shortening vs. Fire Exposing Time and Steel Tube Temperature of CFST Columns with 1.5mm Intumescent Coating and Different Wall Thickness

Table 2 summarizes the critical fire exposure time and critical steel temperature for all the selected columns, concrete infill and intumescent coating increases the critical fire exposing time and promotes steel critical temperature. From this study, with the wall thickness increased from 5.0 mm to 12.5 mm, the critical fire exposure time increased by up to 9%, with the exception of the unfilled steel hollow sections with or without intumescent coating (US, PS) where the increased of the critical fire duration is up to 59% due to the increases in the wall thickness. For CFST columns with or without intumescent coating (UP, PP, PPA and PPB), with the tube wall thickness increased, the critical steel temperature decreased, but for steel hollow section without the concrete infill (US, PS), the critical steel temperature increased with the wall thickness increased.

The critical fire exposing duration increased with the column major diameter changed from 200mm

to 500mm for concrete filled columns (UP, PP, PPA and PPB). However, for the unfilled steel hollow sections (US, PS), the increase of both critical fire exposing time and critical steel temperature were not evident. The comparison clearly indicated that the merit of application of concrete infilling and intumescent coating fire protection for composite members in fire.

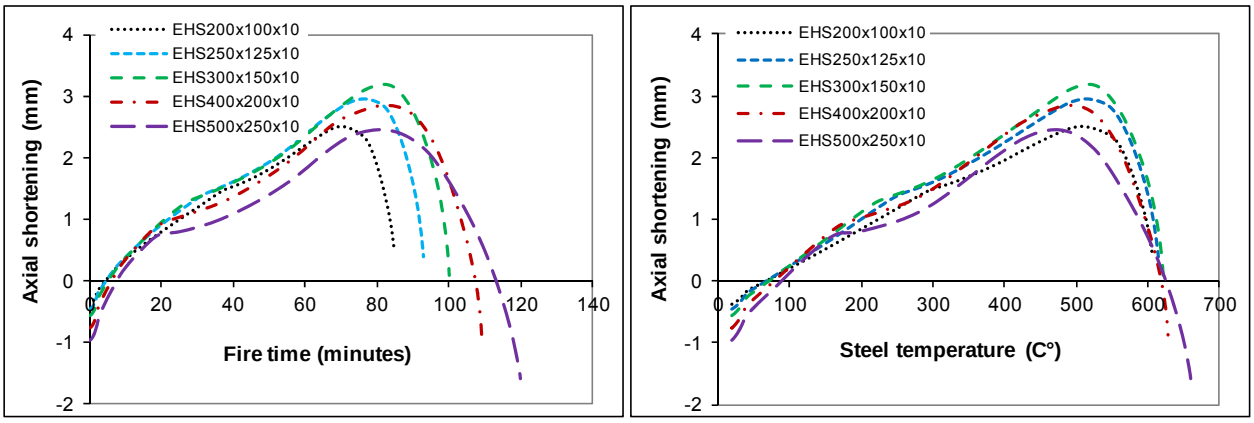

Figure 7. Relationships of Axial Shortening vs. Fire Exposing Time and Steel Tube Temperature for CFST Elliptical Columns with 1.5mm Intumescent Coating and Different Section Sizes

Table 2. Summary of Critical Fire Exposing Time and Steel Tube Temperatures for Selected Hollow Sections with Different Intumescent Coating and Concrete Infill Options

Hollow sections	US		PS		UP		PP		PPA		PPB	
	Time (min)	Temp (ºC)	Time (min)	Temp (ºC)	Time (min)	Temp (ºC)	Time (min)	Temp (ºC)	Time (min)	Temp (ºC)	Time (min)	Temp (ºC)
EHS200×100×5.0	11.6	563	30.4	572	25.5	638	65.9	622	79.2	620	91.9	617
EHS200×100×6.3	12.7	566	34.1	574	26.0	629	67.1	616	80.8	616	93.6	613
EHS200×100×8.0	14.5	566	38.4	577	26.4	617	68.6	611	82.6	611	95.5	607
EHS200×100×10.0	16.3	569	42.2	580	26.9	605	70.3	607	84.5	605	97.7	602
EHS200×100×12.5	18.5	573	48.2	587	28	599	72.3	603	86.9	602	100.4	598
EHS250×125×10.0	16.4	567	42.4	578	28.7	615	76.3	614	92.9	614	107.5	613
EHS300×150×10.0	16.5	568	42.6	578	29.8	615	81.4	619	99.7	619	115.9	619
EHS400×200×10.0	16.6	567	42.8	577	31.5	626	88.4	630	109.0	629	127.6	627
EHS500×250×10.0	16.6	566	43.0	577	38.0	688	98.1	666	119.9	660	141.0	658

6.2 Assessment of Critical Steel Temperature of Elliptical CFST Stub Column Under Axial Compression

Critical temperature is a very important parameter in the structural fire design and analysis. Based on the numerical research presented in this paper, the critical steel temperature changed with different wall thickness and sectional dimension as shown in Figure 8, therefore developing a simple formula to assess the critical steel temperature will be very useful for the structural engineers in their preliminary design. Due to the concrete infill, the critical steel temperature of an elliptical CFST column is higher than an identical unfilled elliptical hollow section column. Based on the numerical analyses conducted in this study, a simple method was developed for elliptical concrete filled stub columns with typical hot-rolled steel and normal weight concrete and a load ratio of 0.5. Equations (1) and (2) may be used to assess the critical steel temperature of elliptical CFST columns and elliptical hollow section columns respectively. Figure 8 compares the critical

steel temperature of columns with various wall thickness, section dimensions and fire protection options and good agreement is obtained.

$$T_{Cr,CFST} = 595 + \left(\frac{a+b}{150}\right)^{1.8}\left(\frac{100}{t}\right)^{1.1} \quad (1)$$

$$T_{Cr,HS} = 560 + \left(1 - \frac{a+b}{1000}\right)t^{1.25} \quad (2)$$

where,

t: tube steel wall thickness (mm);
a: longer outer radius of elliptical hollow section (mm);
b: shorter outer radius of elliptical hollow section (mm);
$T_{Cr,CFST:}$ critical steel temperature of CFST column (°C);
$T_{Cr,HS:}$ critical steel temperature of empty hollow section column (°C).

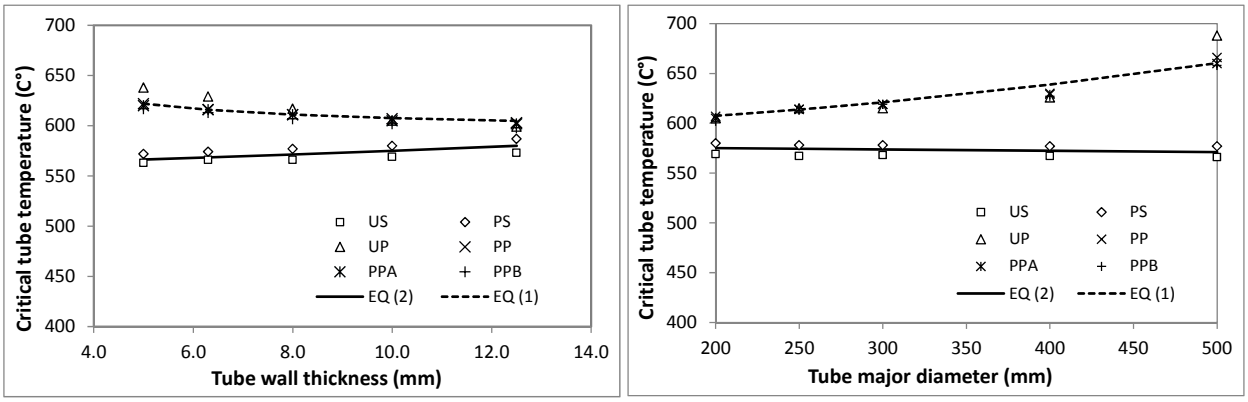

Figure 8. Comparison of Critical Steel Temperature obtained from Simple Method Equations (1) and (2) and FE Modelling Prediction

6.3 Prediction of Maximum Axial Capacity Using a Simplified Method

For CFST stub columns with typical cross-sectional shapes exposed to standard fire, the authors proposed a simple method to calculate the ultimate axial compressive load capacity by section strengths as shown in equation (3). However, in the previous research by Dai and Lam [9], the maximum dimensions of CFST columns were limited to 200mm and without any fire protection. The research results presented in this section could justify the suitability of equation (3) for stub elliptical CFST columns with section dimension above 200 mm and with intumescent coating as additional fire protection.

$$N_{y,f} = A_s f_{y,\theta s} + A_c f_{c,\theta c} \quad (3)$$

where,
A_s: steel tube cross sectional area (mm^2);
A_c: concrete core cross sectional area (mm^2);
$N_{y,f}$*:* sectional strength of CFST column in standard fire (kN) .
$f_{y,\theta s:}$ the yield strength of steel material at temperature θ_s, (N/mm^2).
$f_{c,\theta c}$ the concrete compressive strength at temperature θ_c, (N/mm^2).

Based on the previous study by Dai and Lam [9], equation (3) might be used to assess the maximum axial load capacity of a CFST stub column at elevated temperature. $f_{y,\theta s}$ is the reduced steel strength according to EN1993-1-2 for the steel at elevated temperature. The temperature of concrete core is related to the steel temperature with the coefficient varying with different sectional shapes. The proposed coefficients were: $\theta_c = 0.7\theta_s$ for CFST columns with circular section, $\theta_c = 0.6\theta_s$ for CFST columns with elliptical section and $\theta_c = 0.45\theta_s$ for CFST columns with square and rectangular sections. Due to all the selected CFST stub columns in this paper were elliptical sections, therefore, $\theta_c = 0.6\theta_s$ was used. $f_{c,\theta c}$ is the reduced concrete strength in accordance to the concrete core temperature, θ_c as given in EN1994-1-2.

Figure 9 shows the comparison of maximum axial compressive load of the elliptical CFST columns with various cross sectional dimensions, fire protection options at critical steel temperatures, obtained from numerical analysis and equation (3). It shows that stub elliptical CFST columns without any fire protection (UP) and with intumescent coating (PP, PPA, PPB), the maximum axial compressive load predicted by equation (3), $N_{c,Eq}$ is very close to the maximum axial compressive load predicted by FE model, $N_{c,FE}$ for column sectional dimensions up to 400×200mm. For the column section dimension larger than 400×200 mm, equation (3) would appear to under-estimate the maximum axial compressive load however on the conservative side. For the unfilled elliptical hollow section columns (US and PS) under standard ISO fire, regardless of the intumescent coating fire protection, the maximum axial compressive load predicted by FE modelling is lower than the section strength calculated using equation (3) by ignoring the concrete term ($A_c f_{c,\theta c} = 0$). This is because the maximum load obtained from the FE model considered the effect of local buckling of elliptical hollow section and this was ignored by the simplified method. However, as shown in Figure 9, for empty elliptical hollow section stub columns with different section dimensions, the reduction of maximum load by local buckling was similar and can be corrected by multiplying a constant coefficient of 0.77.

The comparison in this section has shown that the simplified method could be used to predict the maximum axial capacity for stub elliptical CFST columns with different sectional dimensions and intumescent coating fire protection. In addition, an important merit from the concrete core has emerged that the concrete core not only provide substantial enhancement to the axial compressive capacity of the composite columns, but also contribute to the development of full steel sectional strength by delaying or eliminating the local buckling of steel sections in fire.

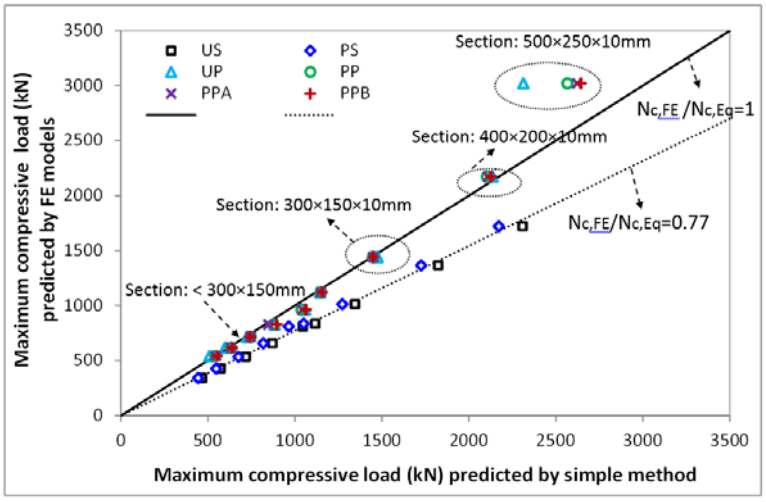

Figure 9. Comparison of Critical Loads obtained from Simple Method Prediction and FE Prediction

7. CONCLUSIONS

The research presented in this paper discussed the effect of concrete infill and intumescent coating to the temperature development and structural fire behaviour of elliptical CFST stub columns under axial compression. The following conclusions could be drawn:

(1) Concrete core reduced steel temperature of elliptical CFST column, however for the commonly used steel elliptical hollow sections (sections range from 200×100×5mm to 200×100x12.5mm and 200×100×10mm to 500×250×10mm adopted in this paper), the concrete core was unable to limit the steel temperature to 550°C for 60 minutes under standard ISO fire exposure. Only by applying intumescent coating to the CFST columns, the steel temperature may be limited to below 550°C.

(2) For elliptical CFST stub columns with identical outer sectional dimensions, it appears that as the steel tube wall thickness increases, the steel temperature reduced and the core centre temperature increased. However if the wall thickness was kept constant (say 10 mm) with the column section dimension increasing from 200×100×10mm to 500×250×10mm, the steel temperature decreased slightly for the columns with intumescent coating, and the concrete core centre temperature reduced significantly due to the increases of the heat flux conducting distance.

(3) When identical elliptical stub columns under a constant axial compressive load ratio and standard ISO fire, the unprotected and unfilled hollow section (US) has the shortest critical fire exposing time, followed by the unprotected concrete filled hollow section (UP). Although the critical fire time of the intumescent coating protected hollow section (PS) is much longer than the critical fire time of unprotected hollow sections (US and UP), it is shorter than the critical fire exposing time of intumescent coating protected CFST columns (PP, PPA and PPB). As expected for stub columns with different steel hollow sections (various wall thickness and various outer sectional dimensions), the critical fire exposing time change agreed with the above conclusions and the thicker the intumescent coating, the longer the critical fire period.

(4) For elliptical CFST stub columns with identical sectional outer dimensions subjected to the same axial compressive load ratio and standard ISO fire, it appears that as the wall thickness increases, the critical fire exposing time increased significantly except for the unprotected concrete filled steel hollow section (UP), the increases of the critical fire exposing time was not evident. The effect of wall thickness to critical steel temperature is different from critical fire exposing time, in which the critical temperature decreased with the increases in wall thickness although for unfilled steel hollow sections (US, PS), the critical steel temperature shows an increasing trend.

(5) As expected, the critical fire exposing time increased with the outer sectional dimension of the elliptical CFST stub columns increasing from 200×100×10mm to 500×250×10mm. In addition, the critical tube steel temperature of concrete filled stub columns (UP, PP, PPA and PPB) increased following the outer sectional dimension increasing, but the critical steel temperatures and critical fire exposure time of unfilled steel hollow sections (US, PS) had little change.

(6) The proposed equations might be used to assess the critical temperatures of stub elliptical CFST columns under axial compression (load ratio of 0.5) at elevated temperature regardless of the existence of intumescent coating fire protection.

(7) The research presented in this paper demonstrates the merits of concrete filled steel hollow sections and intumescent coating fire protection over unfilled steel hollow sections in fire resistance design and application. This information supports the combined application of concrete infill and intumescent coating in fire-resistant structural design.

(8) The proposed equations (1) and (2) are numerically verified by a limited range of the specimens, i.e. elliptical cross sections stub columns with a load ratio of 0.5. Further experimental study is required to validate the accuracy of these equations for CFST columns with different sectional shapes, load ratios and slenderness.

ACKNOWLEDGEMENT

The research reported in this paper is funded by the research grant from the Engineering and Physical Science Research Council (EP/G002126/1) in the UK who are gratefully acknowledged.

REFERENCES

[1] Tao, Z., Han, L.H., Uy, B. and Chen, X., “Post-fire Bond between the Steel Tube and Concrete in Concrete-filled Steel Tubular Columns”, Journal of Constructional Steel Research 2011, Vol. 67, No. 3, pp. 484-496.

[2] Han, L.H. and Lin, X.K., “Tests on Cyclic Behavior of Concrete-Filled Hollow Structural Steel Columns after Exposure to the ISO-834 Standard Fire”, ASCE Journal of Structural Engineering, 2004, Vol. 130, No. 11, pp. 1807-1819.

[3] Han, L.H., Lin, X.K. and Yang, Y.F., “Cyclic Performance of Concrete Filled Steel Tubular Columns after Exposure to Fire: Analysis and Simplified Model”, Advances in Structural Engineering, 2008, Vol. 11, No. 4, pp. 455-473.

[4] Huo, J., Huang, G. and Xiao, Y., “Effects of Sustained Axial Load and Cooling Phase on Post-fire Behaviour of Concrete-filled Steel Tubular Stub Columns”, Journal of Constructional Steel Research, 2009, Vol. 65, No. 8-9, pp. 1664-1676.

[5] Zha, X.X., “FE Analysis of Fire Resistance of Concrete Filled CHS Columns”, Journal of Constructional Steel Research, 2003, Vol. 59, No. 6, pp. 769–779.

[6] Hong, S. and Varma, A.H., “Analytical Modelling of the Standard Fire Behavior of Loaded CFT Columns”, Journal of Constructional Steel Research, 2009, Vol. 65, No. 1, pp. 54-69.

[7] Espinos, A., Romero, M.L. and Hospitaler, A., “Advanced Model for Predicting the Fire Response of Concrete Filled Tubular Columns”, Journal of Constructional Steel Research 2010, Vol. 66, No. 8-9, pp. 1030–1046.

[8] Espinos, A., Gardner, L., Romero, M.L. and Hospitaler, A., “Fire Behaviour of Concrete Filled Elliptical Steel Columns”, Thin-Walled Structures, 2011, Vol. 49, No. 2, pp. 239–255.

[9] Dai, X.H. and Lam, D., “Shape Effect on the Behaviour of Axially Loaded Concrete Filled Steel Tubular Stub Columns at Elevated Temperature” Journal of Constructional Steel Research, 2012, Vol. 73, No. 6, pp. 117-127.

[10] Corus Construction & Industrial, Fire Resistance of Steel-framed Building, 2006 Edition (online).

[11] Dai, X.H., Wang, Y.C. and Bailey, C.G., “Effects of Partial Fire Protection on Temperature Developments in Steel Joints Protected by Intumescent Coating”, Fire Safety Journal 2009, Vol. 44, pp. 376-86.

[12] Dai, X.H., Wang, Y.C. and Bailey, C.G., “A Simple Method to Predict Temperatures in Steel Joints with Partial Intumescent Coating Fire Protection”, Fire Technology Journal 2010, Vol. 46, pp. 19-35.

[13] BS EN 1994-1-2, Eurocode 4: Design of Composite Steel and Concrete Structures, Part 1-2: General Rules-Structural Fire Design, British Standards Institution, London, 2005.

[14] ISO 834, Fire Resistance Tests, Elements of Building Construction. International Organization for Standardization, Geneva 1975.

[15] BS EN 1993-1-2, Eurocode 3: Design of Steel Structures, Part 1.2: General Rules-Structural Fire Design, British Standards Institution, London 2005.

[16] BS EN 1991-1-2, Eurocode 1: Actions on Structures, Part 1-2: General Actions-Actions on Structures Exposed to Fire, British Standards Institution, London 2002.

[17] Ding, J. and Wang, Y.C., “Realistic Modelling of Thermal and Structural Behaviour of Unprotected Concrete Filled Tubular Columns in Fire”, Journal of Constructional Steel Research, 2008, Vol. 64, pp. 1086-1102.

ULTIMATE CAPACITY ASSESSMENT OF WEB PLATE BEAMS WITH PITTING CORROSION SUBJECTED TO PATCH LOADING BY ARTIFICIAL NEURAL NETWORKS

Yasser Sharifi* and Sajjad Tohidi

Department of Civil Engineering
Vali-e-Asr University of Rafsanjan, Rafsanjan, Iran
**(Corresponding author: E-mail: yasser_sharifi@yahoo.com or y.sharifi@vru.ac.ir or)*

Received: 17 May 2013; Revised: 19 October 2013; Accepted: 22 October 2013

ABSTRACT: Corrosion is an unavoidable phenomenon in ship hull structures and thickness loss of the structural members due to corrosion is a great concern when the integrity of hull structures is considered. It is well known that pitting corrosion occurring on coated hold frames will surely result in a significant degradation of the ultimate strength of these members. Extensive study on the effect of pitting corrosion on structural strength under a wide variety of loading conditions is necessary to assess the relationship between pitting corrosion intensity and residual strength precisely. The aim of the present study is to investigate the ultimate strength characteristics of steel beams with pit and uniform corrosions wastage. Then pitted member will predict with a member that its thickness decreases uniformly in terms of ultimate strength. A series of ABAQUS nonlinear elastic-plastic analyses by Finite Element Method (FEM) has been carried out on I-shape section steel models, varying the degree of pit corrosion intensity. Load-carrying capacity of deteriorated steel beam models with different pit corrosion under patch loading has been estimated using Artificial Neural Network (ANN) method using FE results. The ultimate strength reduction factor due to web pitting corrosion of steel beams is empirically derived by ANNs of the computed results as a function of DOP. Hence, the results of this study can be used for better prediction of the failure of deteriorated steel beams by practice engineers.

Keywords: Pitting corrosion, steel structures, nonlinear FE analyses, patch loading, artificial neural networks

1. INTRODUCTION

Steel structures such as ships, offshore platforms, and land-based structures are prone to suffer various types of damage while service. Carbon steel is one of the most widely used materials in these structures. A typical characteristic of deterioration of carbon steel structures exposed to aggressive chloride environments is corrosion. Corrosion can affect the structural performance in several ways. Corrosion wastage in steel beams can reduce their ultimate strength. It is of vital importance to estimate the residual strength of damaged structures for many reasons. For instance, it is essential to seek rational standards for the structural integrity of aging structures without economic penalties with respect to the repair and maintenance schemes are normally applied for that purpose. Within the scheme of ultimate limit state based risk or reliability assessment for aging structures, closed-form expressions for predicting the ultimate strength of structural members taking account of the effect of structural damage are required. In addition improperly maintained ageing ship structure could finally lead to disastrous casualties in rough seas and heavy weather. Thus, it is important to assess the residual strength of ageing ship structure properly either with corrosion or with other type of defects in order to reflect vessel's inspection and maintenance programme (Nakai et al. [1-3]; Paik et al. [4-5]; 2006; Sharifi and Paik [6-7]; Sharifi [8]; Sharifi and Tohidi [9]). Despite a large number of procedures to keep steel structures from corrosion attack such as painting and galvanizing, there are numerous existing structures which have not preserved so far. Beside this, in several points these preservations such as painting break down and the corrosive environment attack to the pure steel and make it damaged. Therefore, assessment the residual strength of these structures is an important issue to keep them in a reliable and safe utilization. Totally, corrosion divided into two principal types, that is, general and localized

corrosions in the land-based structures, marine, offshore and industry structures. Pitting corrosion which is considered in this study is categorized as a form of localized corrosion (Nakai et al. [1-3]). For general corrosion, which uniformly reduces plate thickness, the plate ultimate strength calculations are typically carried out excluding the thickness loss due to corrosion. For localized corrosion such as pitting or grooving, the strength calculation procedure can be more complex, and for a simplified pessimistic treatment, the corroded plates have been idealized using an equivalent general corrosion. However, this treatment is not always relevant since it is not straightforward to define the equivalent general corrosion properly. Therefore, In the case of the members with pitting corrosion the evaluation of residual strength is considered to be more difficult compared to members with uniform corrosion (Nakai et al. [1-3]; Paik et al. [4-5]; 2006; Sharifi and Paik [6-7]; Sharifi [8]). When beam strength is considered, in general, collapse strength (no buckling), lateral-distortional buckling strength, local buckling strength, shear strength of web plates and web crippling strength under concentrated loading are important factors (Nethercot [10]). Therefore, it is obvious that there is a need for further research to investigate the effect of pitting corrosion on each mentioned factor. Patch load action on steel girders are frequently encountered in marine structures and civil engineering practice. This type of loading can be found in ship or crane girders, secondary beams reaction acting over the primary girder system and other structural problem. In addition for bridge girders, the major problem concerning the load carrying capacity due to concentrated forces occurs during launching. During this operation, the launching rollers or plates introduce concentrated forces through the bottom flange into the girder web, a load case usually called patch loading. FEA method has now become the most common, powerful and flexible tool in rational structural analysis and makes it possible to predict the strength of complex structures more accurately than existing classical theoretical methods. Over last decades there has been significant development of computer hardware and FEA software. Although finite-element method can be used, in principle, to predict buckling and post buckling strengths, it still requires quite much computational time and cost. For this reason and above-mentioned reasons some useful empirical formulae to assess structural integrity during the initial design, inspection and maintenance are always necessary for effective and on-site decisions. ANN method recently have been introduced in structural engineering problems. ANN represents a useful of the biologic neural structures of 326the central nervous system. Attempts to use ANN in structural engineering problems are introduced by several researchers (Adeli and Hung [11]; Fonseca et al. [12]; Jang [13]; Hagan and Menhaj [14]; Guzelbey et al. [15]).

In this paper, a series of ABAQUS nonlinear elastic-plastic analyses by FEM has been carried out on I-shape section steel models, varying the degree of pit corrosion intensity. In these models, artificial pitting with different intensities was made on the web plates and two equal concentrated loads have been applied vertically at the one third points of the simply supported models as shown in Figure 1. Meanwhile, load-carrying capacity of deteriorated models with different uniform thickness loss on the web has been also developed. Then, the ANN method has been employed to derive new empirical formulae for load carrying capacity of damaged models in terms of DOP. Based on the results, the ultimate strength of the web plates with different pitting corrosion intensities has been predicted with a uniform loss thickness; therefore, formulae for estimating the average loss thickness and hence load-carrying capacity have been also developed here.

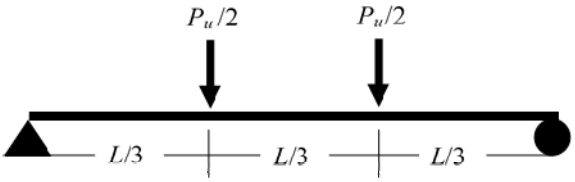

Figure 1. Loading Condition

2. IDEALIZATION OF CORROSION DAMAGE

Figure 2 shows some of the more important types of corrosion related damages which affect the strength of steel structures. 'General' corrosion (also called 'uniform' corrosion) uniformly reduces the thickness of structural members as shown in Figure 2(a), while localized corrosion (e.g., pitting or grooving) causes degradation in local regions as shown in Figure 2(b). Sometimes fatigue cracks may arise from localized corrosion, as shown in Figure 2(c). The corrosion damage of steel structures is influenced by many factors, including the corrosion protection system and various operational parameters. In general, the corrosion protection systems employed for ships or offshore platforms are coatings (paint) and anodes. The operational parameters include maintenance, repair, percentage of time in ballast, frequency of tank cleaning, temperature profiles, use of heating coils, humidity conditions, water and sludge accumulation, microbial contamination, composition of inert gas and so on. To date, basic work to understand the effects of many of these factors and their interactions is lacking in the case of marine structures (Paik et al. [4-5]; 2006; Sharifi and Paik [6-7]; Sharifi [8]).

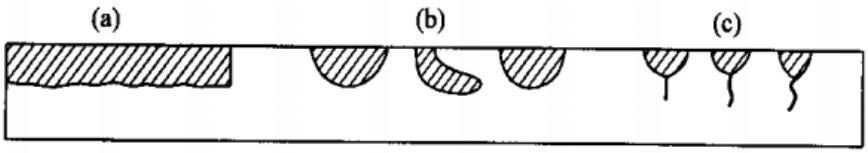

Figure 2. Typical Modes of Corrosion Damage: (A) General (Uniform) Corrosion; (B) Localized Corrosion; (C) Fatigue Cracks Arising from Localized Corrosion

Pitting corrosion as the principal factor for deteriorated structures in corrosive environments has been used here. To assess the scale of breakdown due to pit corrosion, a parameter denoted DOP (degree of pit corrosion intensity) is often used, where DOP is defined as the ratio percentage of the corroded volume to the original plate volume, namely,

$$DOP = \sum_{i=1}^{n} \frac{V_{pi}}{abt} \times 100(\%) \tag{1}$$

where n is the number of pits, V_{pi} is the volume of the *ith* pit, a is the plate length, b is the plate breadth and t is the plate thickness.

Figure 3 shows pit shape and typical sample of pit corrosion damage distribution in web plates. Although the distribution of the pit corrosion on the plates is scattered, it can be seen that the shape of the corrosion is typically cylindrical. Our investigation of the web girder plate assumes that both sides of it will corrode in a localized manner. It is also assumed that pitting corrosion, which is uniformly distributed, affects the strength of the following plates by the different degrees of intensity shown in Figure 3. Finally, it is assumed that the pit diameter to the depth is 8, and the distance between the adjacent pits centers is constant.

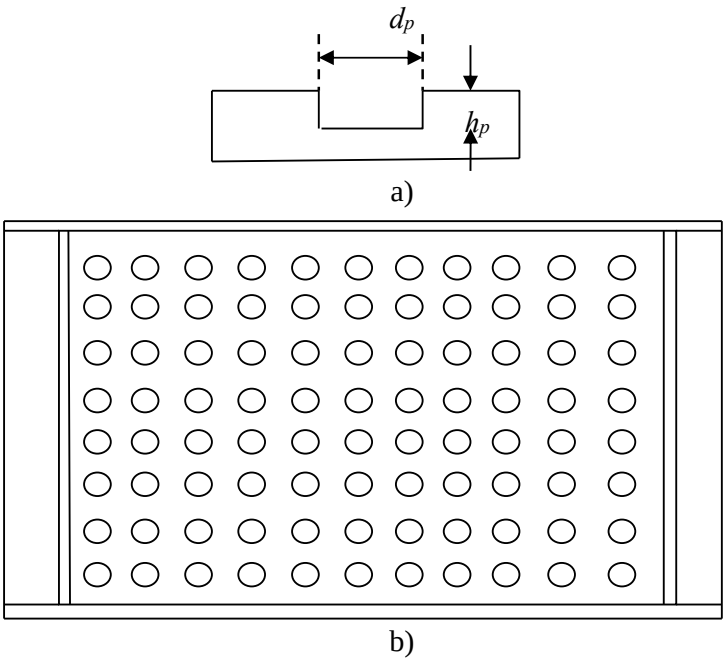

Figure 3. Pit Shape (A), and Pit Distribution (B) on the Beam Web

3. PATCH LOADING REVIEW

Patch loading is a significant phenomenon for steel beam and girders. Steel beams or girders are often subjected to concentrated loads commonly named as patch loading which directly determines the proportioning of the section. The failure mode of unstiffened webs subjected to patch loading is very local, and a buckle appears under the compression flange. To a large extent the size of the buckle depends on the dimensions of the loaded flange. Patch load action on steel girders are frequently encountered in marine structures and civil engineering practice. This type of loading can be found in bridge, ship and crane girders, secondary beams reaction acting over the primary girder system and other structural problem. For bridge girders, the major problem concerning the load carrying capacity due to concentrated forces occurs during launching. During this operation, the launching rollers or plates introduce concentrated forces through the bottom flange into the girder web, a load case usually called patch loading. The collapse strength of an unstiffened web subjected to patch (transverse) loads applied through a plate girder flange is governed by one of the following three failure mode (EN 1993-1-1 [16]):

1- crushing of the web close to the flange, accompanied by plastic deformation of the flange;
2- crippling of the web in the form of localized buckling and crushing of the web close to the flange, accompanied by plastic deformation of the flange; and
3- buckling of the web over most of the depth of the plate girder.

Two types of load application are normally considered: (1) forces applied through one flange and resisted by shear forces in the web; or (2) forces applied to one flange and transferred through the web directly to the other flange. For load type (1), the capacity of the web to lateral forces may be determined as the smaller value of the two strengths due to crushing and crippling. For load type (2), the web capacity may be taken as the smaller value of the two strengths due to crushing and buckling. The crippling strength of a web with intermediate transverse stiffeners is similar to that of an

unstiffened web, with the increase due to stiffeners (Paik and Thayamballi, [17]). Dogaki et al. [18] studied the ultimate strength of longitudinally stiffened plate girders under patch loading. They concluded that the optimum location of the longitudinal stiffener close to the plate girder flange under patch loading is about $b_w = 0.15h_w$. Dogaki et al. [19] then proposed an empirical expression of the ultimate strength, P_u, of plate girder under patch loading by curve fitting based on their own test results, as follows:

$$\frac{P_u}{2V_P} = \frac{0.594}{\lambda} + 0.069 \tag{2}$$

For plate girder without longitudinal stiffeners under patch loading, Takimoto [20] proposed a closed-form expression of the ultimate strength, P_u, as follows:

$$P_u = \left(25t_w^2\sigma_{Yw} + 4t_w t_f \sigma_{Yf}\right)\left(1 + \frac{S_s + 2t_f}{2h_w}\right) \tag{3}$$

where the plastic shear strength is $V_P = h_w t_w \tau_Y$, $\tau_Y = \frac{\sigma_{Yw}}{\sqrt{3}}$ is the shear yield strength, σ_{Yw} is the web yield strength, h_w is the high of the web plate, t_w is the web thickness, $\lambda = \sqrt{\frac{2V_P}{P_E}}$ is buckling parameter, and P_E is elastic buckling strength of plate girder web under patch loading, taking into account the effects of flexural and torsional rigidities of the flange (Paik and Thayamballi, [17]).
Roberts and Rockey [21] investigated the collapse loads of slender plate girders when subjected to in-plane patch loading. They proposed a solution for the ultimate capacity of unstiffened plate girders with slender webs subjected to concentrated loading based on a yield line mechanism composed of four plastic hinges in the flange and three yield lines in the web. Bergfelt [22] has treated the problem of patch loading on a slender web-influence of horizontal and vertical web stiffeners on the load carrying capacity. He proposed a formula for predicting the ultimate resistance of plate girders under patch loading.

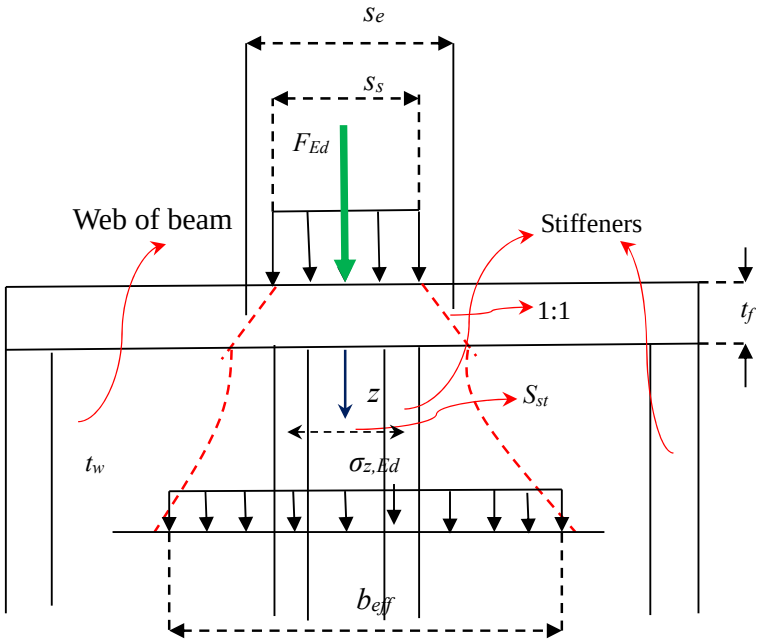

Figure 4. In-Plane Load Introduction

For a stiffened or unstiffened girder web with infinite depth the maximum elastic stress due to the local introduction of in-plane forces (patch loads) at a distance z below the patch load is shown in Figure 4. The elastic stress ($\sigma_{z,Ed}$) was given by (EN 1993-1-5, [23]):

$$\sigma_{z,Ed} = \frac{F_{Ed}}{b_{eff}(t_w + a_{st,l})} \tag{4}$$

where

$$b_{eff} = s_e\sqrt{1+\left(\frac{z}{s_e n}\right)^2},$$

$$n = 0.636\sqrt{1+\frac{0.878a_{st,l}}{t_w}},$$

$$s_e = s_s + 2t_f.$$

where,

$a_{st,l}$ is the gross cross-sectional area of the stiffeners smeared over the length s_e. This may be taken, conservatively, as the area of the stiffeners divided by the spacing s_{st}; t_w is the web thickness; t_f is the flange thickness; z is the distance to flange; and s_s is the length of patch load can be seen in Figure 4. It should be noted that the equation (4) is valid when $\frac{s_{st}}{s_e} \le 0.5$, otherwise the contribution of stiffeners should be neglected.

Lagerqvist and Johansson [24] investigated the resistance of I-girders to concentrated loads. They presented the design model for the patch loading resistance of unstiffened plate girders. Those model was based on the post-critical strength of the plate girders by the use of stability checks using buckling curves for the patch loading resistance. This model was the basis for the formula in EN 1993-1-5 [23] in which the patch loading resistance for unstiffened plate girders F_{Rd} is given by:

$$F_{Rd} = \frac{f_{yw} L_{eff} t_w}{\gamma_{M1}} \tag{5}$$

where f_{yw} is the yield strength of the web;

EN 1993-1-1 [16] recommends a value γ_{M1}=1.0 and in these equations, L_{eff} is the effective length for resistance to transverse forces given by:

$$L_{eff} = \chi_F l_y \tag{6}$$

where l_y is the effective loaded length appropriate to the length of stiff bearing s_s, χ_F is the reduction factor due to local buckling and can be obtained as following:

$$\chi_F = \frac{0.5}{\bar{\lambda}_F} \le 1.0 \tag{7}$$

where $\bar{\lambda}_F = \sqrt{\frac{l_y t_w f_{yw}}{F_{cr}}}$,

in which the effective loaded length given by:

$$l_y = \begin{cases} s_s + 2t_f\left(1+\sqrt{m_1+m_2}\right) \le \text{distance between adjacent transverse stiffeners} \\ \min\left\{ l_e + t_f\sqrt{\frac{m_1}{2}\left(\frac{l_e}{t_f}\right)^2 + m_2}, l_e + t_f\sqrt{m_1+m_2} \right\} \end{cases} \quad (8)$$

where t_f is thickness of flange and the dimensionless parameters l_e, m_1 and m_2 are

$$l_e = \frac{k_F E t_w^2}{2 f_{yw} h_w} \le s_s + c \quad (9)$$

$$m_1 = \frac{f_{yf} b_f}{f_{yw} t_f} \quad (10)$$

$$m_2 = \begin{cases} 0.02\left(\frac{h_w}{t_f}\right)^2 & if \quad \bar{\lambda}_F > 0.5 \\ 0 & if \quad \bar{\lambda}_F \le 0.5 \end{cases} \quad (11)$$

where f_{yf}, b_f and t_f are yield stress, width and thickness of flange beam, E is the modulus of elasticity of beam steel, and h_w is depth of web panel. It should be noted that m_2 should be taken as zero for welded girders if $\bar{\lambda}_F < 0.5$ in which $\bar{\lambda}_F$ is the slenderness parameter.
F_{cr} is the buckling load which is expressed as:

$$F_{cr} = 0.9 k_F E \frac{t_w^2}{h_w} \quad (12)$$

As shown in Figure 5 the buckling coefficient k_F is given by:

$$k_F = \begin{cases} 6 + 2\left(\frac{h_w}{a}\right)^2 & \text{For type (a)} \\ 3.5 + 2\left(\frac{h_w}{a}\right)^2 & \text{For type (b)} \\ 2 + 6\left(\frac{s_s + c}{h_w}\right) \le 6 & \text{For type (c)} \end{cases} \quad (13)$$

Where a and c have been shown in Figure 5.

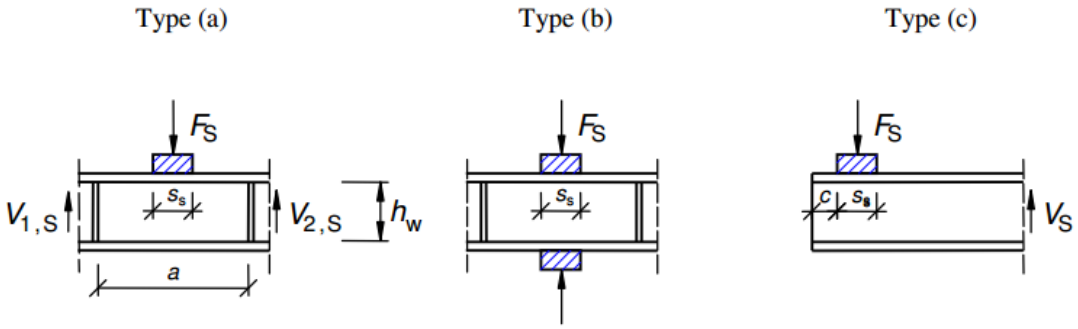

Figure 5. Buckling Coefficients for Different Types of Load Application

4. FINITE ELEMENT MODEL SIMULATION

As mentioned, in the present study it has been decided to demonstrate the ultimate strength reduction characteristics of a beam web plate with pit corrosion and under patch loading by ABAQUS nonlinear FE analysis [25]. The strength of pitted web plates is determined by nonlinear finite element analysis, changing geometrical features of pits, which allows for identification of the effect of the pitting corrosion on ultimate strength of web plate beams. An elasto-plastic analysis has been conducted to simulate the effect of corrosion pit on ultimate strength behavior. Moreover, in order to verification of simulation an experimental or correct FE results is needed. Therefore, it was decided to compare current FE results with Nakai et al. [1] experimental work which consider a model shown in Figure 6a. As it can be seen from Figure 7b our modeling and boundary conditions match with this model.

For initial geometric imperfection of the models, the average level of maximum deflection is approximately taken as *Wo*/10 according to the measured data (Nakai et al. [1]). The deformation is consistent with the buckling mode by eigenvalue analysis. Based on previous studies such as one by Nakai et al [1], effect of welding residual stress is not remarkable and has no effect on the results in case of assessment of ultimate strength of web plate. Moreover, a primary concern in the present analysis is the ultimate strength reduction characteristics due to pit corrosion, i.e., the ultimate strength ratio of the corroded web plate beam to the perfect (un-corroded) (control specimen) ones. Therefore, in the present study the effect of welding residual stress has been neglected.

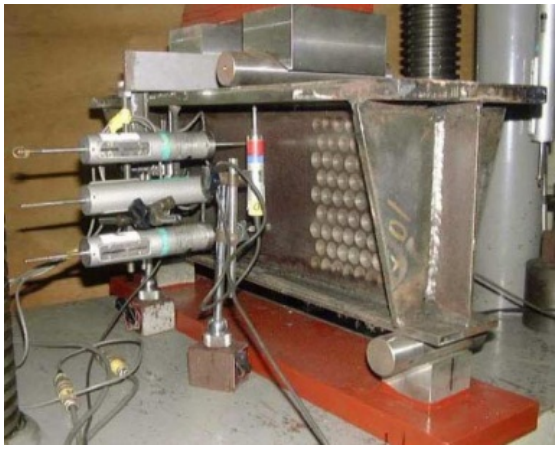

a) (Nakai et al. [1])

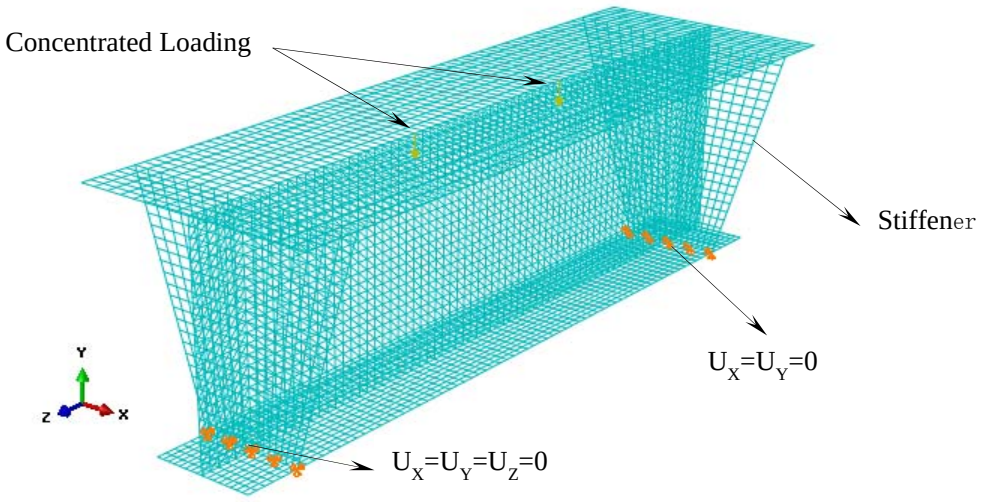

b)

Figure 6. Model and Boundary Condition of Beam Web Plate

5. VALIDATION OF THE MODELING TECHNIQUE

To validate the finite element analysis, a simply supported beam under patch loading (A4-1) which is similar to the model of Nakai et al. [1] was analyzed. The material of web plates and flanges in steel beam structures are given in Table 1. Thickness of the plates is 6, 10 and 19 *mm*. The Young modulus and Poisson ratio are E = 205800 *MPa* and υ =0.3, respectively. The geometrical model and load direction used in the FE analysis is as same of Reference [1]. The load-vertical deflection and load-lateral deflection from Nakai et al [1] and the current results are shown in Figurs 7, where the curves in both cases present a consistent tendency and the ultimate strength of beams match excellently. The maximum load obtained by FEA was 773.8 *kN*, which is about 5% lower than the experimental test specimen (778 *kN*). This comparison has the objective of validating the present results with other published results so as to provide confidence that the FEM simulation in the current work can predict accurately the decreased ultimate strength of beams subjected to pitting corrosion.

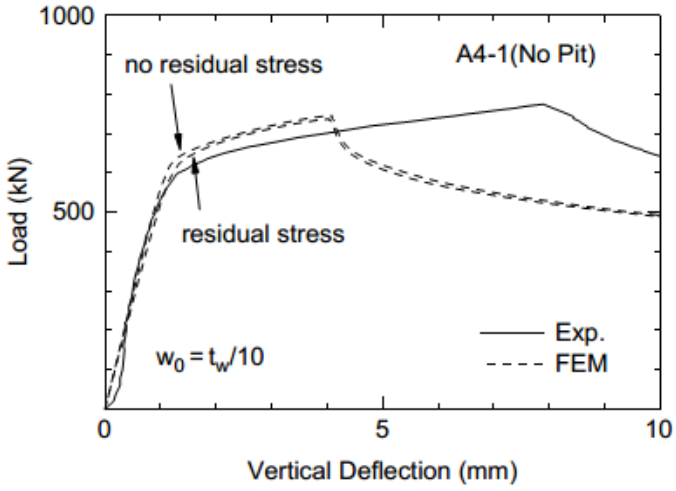

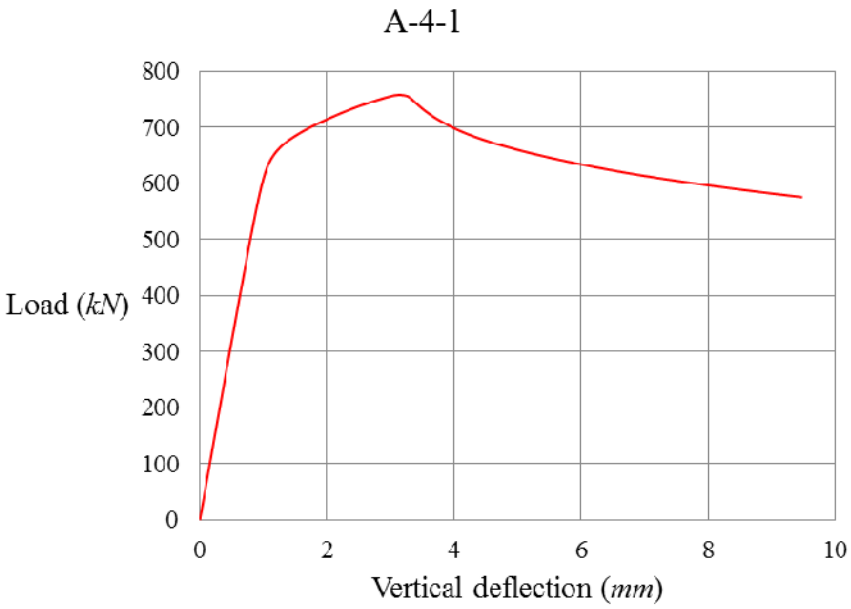

Figure 7a. Load – Vertical Deflection Curves under Patch Loading of Beams (Top from Ref. [1], bottom is result of present work)

Table 1. Mechanical Properties of Tested YP32 Steel

t (*mm*)	*Y.P* (*MPa*)	*T.S* (*MPa*)	*EI.* (%)
6	421	544	30
10	352	516	33
19	331	508	33

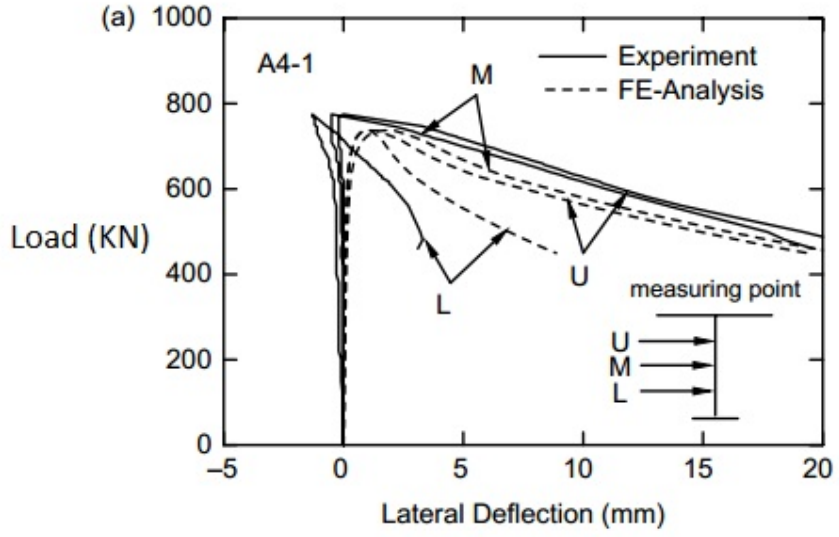

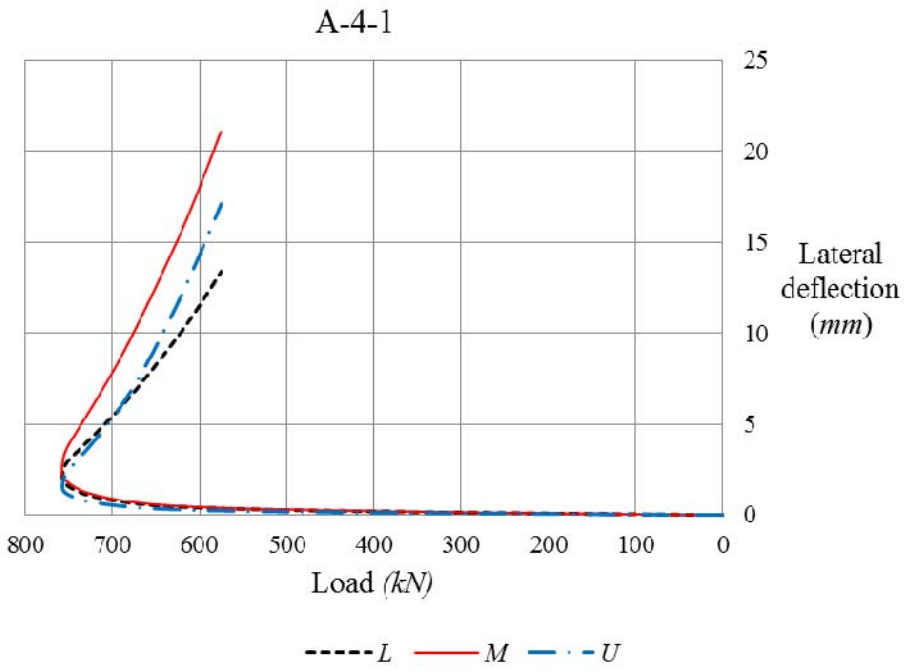

Figure 7b. Load – Lateral Deflection Curves under Patch Loading of Beams
(Top from Ref. [1], bottom is result of present work)

6. NON-LINEAR FEM ANALYSIS AND DISCUSSION

In the following part, the effect of double side distributed pits on the ultimate capacity of beam plates with corroded web is investigated. Several research results (Saad-Eldeen et al. [26-27]) have shown that the material properties of corroded steel may change. But as mentioned before, since the load-carrying capacity ratio of corroded specimens to control specimen is investigated here, this has no effect on the present results. Therefore, the effect of corrosion on material properties has not been taken into account in this study. Figure 8 shows a typical steel web plate between flanges in an I-beam structure subjected to patch loading. The web plate and flanges length, breadth and thickness denotations are shown also in Figure 8. The geometric and material properties of the plate are as follows:

– (L_1) =500 *mm*
– Plate breadth (L_2) = 450 *mm*
– Plate height (h_w) = 300 *mm*
– Plate thickness (t) = 10 *mm*
– Flange breadth (b_f) = 150 *mm*
– Flange thickness (t_f) = 25 *mm*
– Shape of pit corrosion= cylindrical
– Elastic modulus (E) = 205.8 *GPa*
– Poisson's ratio (υ) = 0.3
– Material yield stress (σ_y) = 421 *MPa*

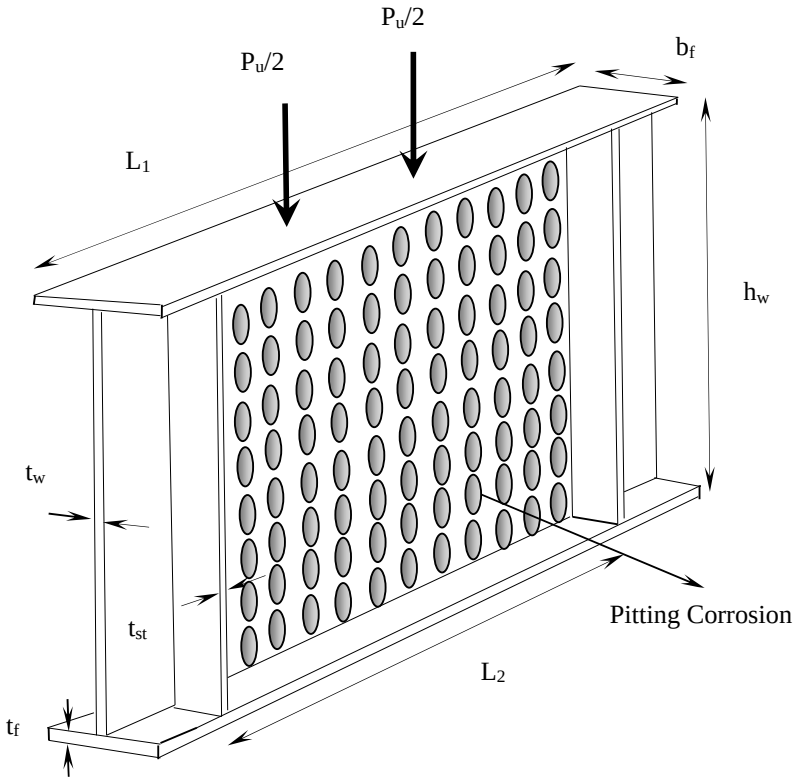

Figure 8. A Typical Model of Beam Web Plate

As stated previously, a series of nonlinear FE analyses have been conducted using ABAQUS software. The arc length method is applied to accomplish the procedure. The boundary conditions of this steel beam are as same of Figure 6b. In order to have exact simulation, shell element has been chosen. This type of element is completely suitable to simulate the real pit shape. There are several literatures that report the strain hardening has a negligible effect on the ultimate strength of steel structures (Paik et al. [4-5]). Nevertheless to simulate precisely, here steel is modeled as a J2 material with bilinear isotropic hardening and a stress–strain curve that consists of an elastic region and a strain hardening region is assumed. It has been supposed a uniform distribution pits on both sides of the web plate as can be seen from Figure 8. The shape of pit corrosion is supposed cylindrical with ratio of pit diameter to its depth 8. The pit corrosion characteristics have been shown in Table 2. As can be seen from this Table, the range of DOP is between 0 - 59.72 %. It should be mentioned here that by employing the ratio of pit diameter to its depth as 8, the maximum DOP will be 59.72%.

Figures 9 show deflected shapes of beam web plates with various pit corrosion intensities immediately after the ultimate strength is reached. The loads in ultimate state have been summarized in Table 3. The load-carrying capacitates of damaged steel beams for each DOP has been also shown in this Table. As it was expected, the capacity with increasing DOP is decreased. It should be noted here that, this trend is not similar for maximum axial shortening and lateral deflection. This is attributed to the fact that the localized plasticity develops in different increments due to the unevenness behavior of pit corrosion elements. Figures 10 and 11 show the patch loads versus vertical deflection and maximum lateral deflections curves for all beams with different damaged corrosion intensities. It is obvious that ultimate load and deformation behaviors are strongly affected by pit corrosion intensities. As the analyses increments have been kept constant during the nonlinear evaluations by software, it can be found from Figures 10 and 11 that the specimens with higher DOP give more deformability compare to specimens with lower DOP.

Table 2. Artificial Pitting in Structural Models

Model No.	Pit diameter (*mm*)	Pit depth (*mm*)	Number of pits	Ratio of pit diameter to depth (d_p/h_p)
Dop=0.00% (Intact)	0	0	0	0
Dop=0.66%	8	1	88	8
Dop=5.24%	16	2	88	8
Dop=10.24	20	2.5	88	8
Dop=17.69	24	3	88	8
Dop=28.1	28	3.5	88	8
Dop=34.56	30	3.75	88	8
Dop=41.94	32	4	88	8
Dop=50.31	34	4.25	88	8
Dop=59.72	36	4.5	88	8

d_p = Pit diameter
h_p =Pit depth

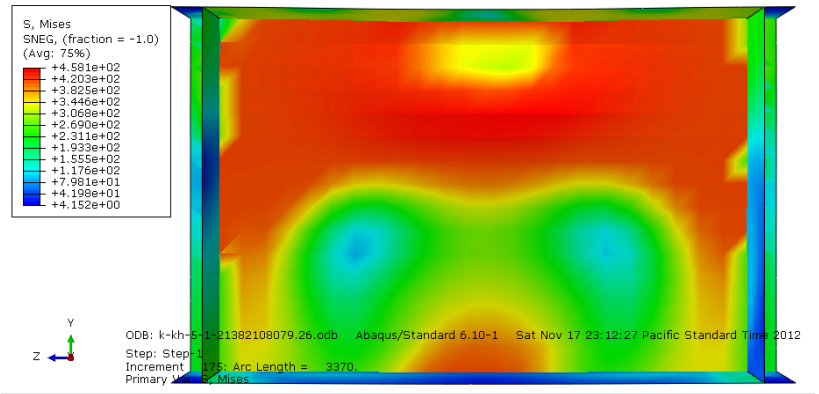

a)

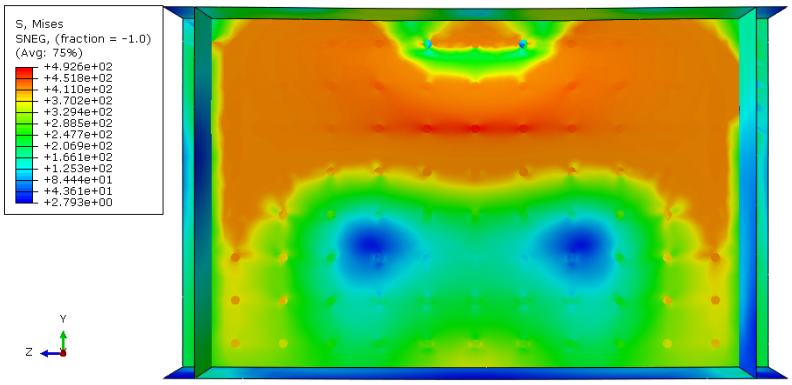

b)

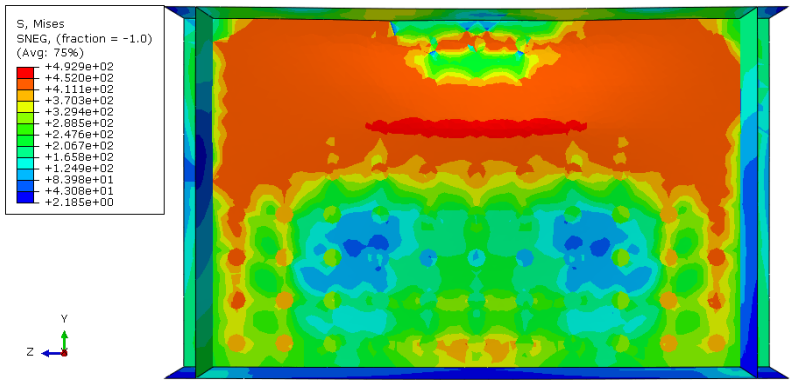
S, Mises
SNEG, (fraction = -1.0)
(Avg: 75%)
+4.929e+02
+4.520e+02
+4.111e+02
+3.703e+02
+3.294e+02
+2.885e+02
+2.476e+02
+2.067e+02
+1.658e+02
+1.249e+02
+8.398e+01
+4.308e+01
+2.185e+00
Y
Z

c)

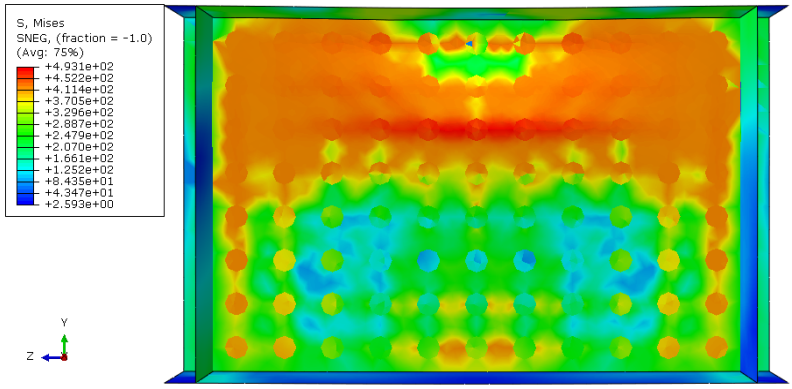
S, Mises
SNEG, (fraction = -1.0)
(Avg: 75%)
+4.931e+02
+4.522e+02
+4.114e+02
+3.705e+02
+3.296e+02
+2.887e+02
+2.479e+02
+2.070e+02
+1.661e+02
+1.252e+02
+8.435e+01
+4.347e+01
+2.593e+00
Y
Z

d)

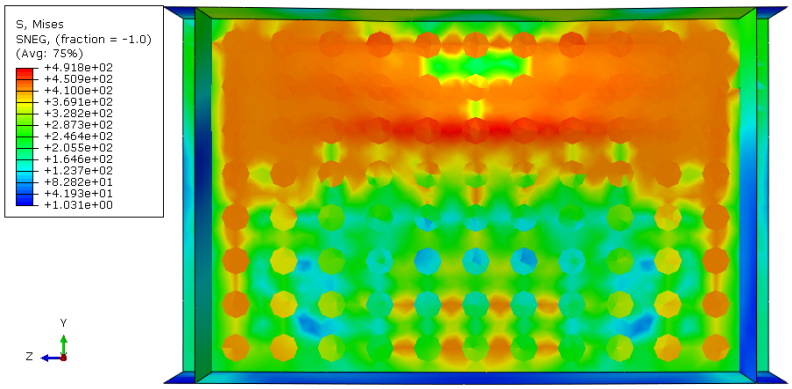
S, Mises
SNEG, (fraction = -1.0)
(Avg: 75%)
+4.918e+02
+4.509e+02
+4.100e+02
+3.691e+02
+3.282e+02
+2.873e+02
+2.464e+02
+2.055e+02
+1.646e+02
+1.237e+02
+8.282e+01
+4.193e+01
+1.031e+00
Y
Z

e)

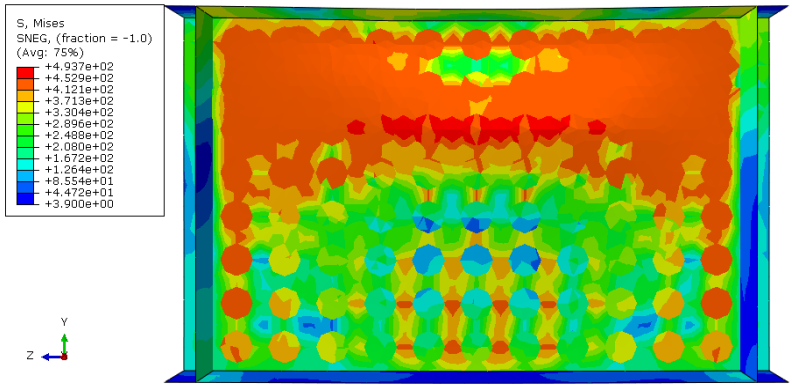
S, Mises
SNEG, (fraction = -1.0)
(Avg: 75%)
+4.937e+02
+4.529e+02
+4.121e+02
+3.713e+02
+3.304e+02
+2.896e+02
+2.488e+02
+2.080e+02
+1.672e+02
+1.264e+02
+8.554e+01
+4.472e+01
+3.900e+00
Y
Z

f)

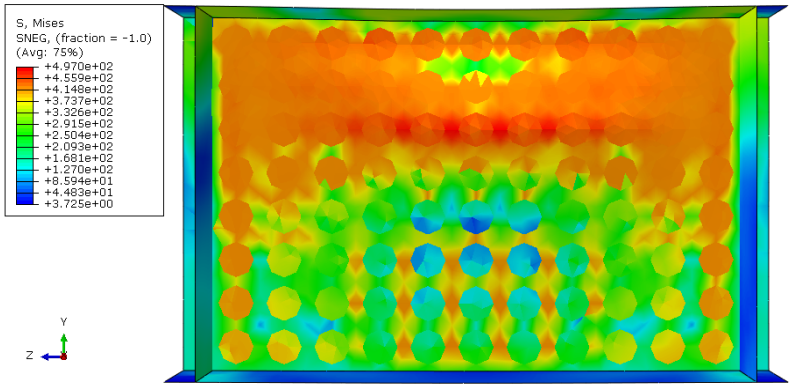
S, Mises
SNEG, (fraction = -1.0)
(Avg: 75%)
+4.970e+02
+4.559e+02
+4.148e+02
+3.737e+02
+3.326e+02
+2.915e+02
+2.504e+02
+2.093e+02
+1.681e+02
+1.270e+02
+8.594e+01
+4.483e+01
+3.725e+00
Y
Z

g)

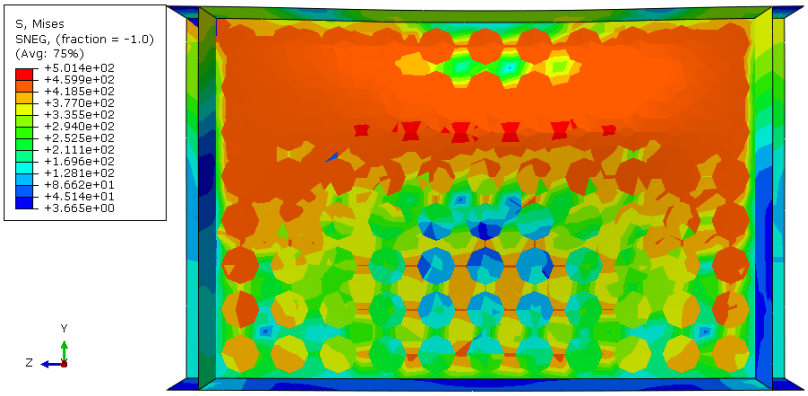
S, Mises
SNEG, (fraction = -1.0)
(Avg: 75%)
+5.014e+02
+4.599e+02
+4.185e+02
+3.770e+02
+3.355e+02
+2.940e+02
+2.525e+02
+2.111e+02
+1.696e+02
+1.281e+02
+8.662e+01
+4.514e+01
+3.665e+00
Y
Z

h)

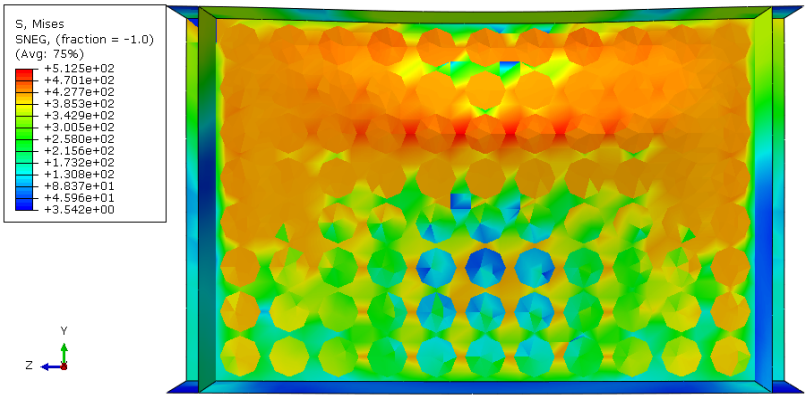

i)

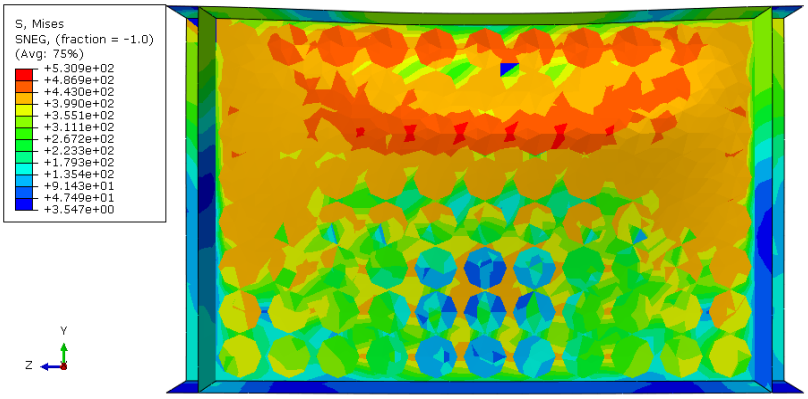

j)

Figure 9. Deformation and the Von Mises Stress Distribution on Mid-Surface of a Pitted Beam Web Plate under Patch Loading, with Varying Level Of DOP at the Ultimate Strength, as Obtained by ABAQUS: (a) Intact; (b) DOP 0.66%; (c) DOP 5.24%; (d) DOP 10.24%; (e) DOP 17.69%; (f) DOP 28.1%; (g) DOP 34.56%; (h) 41.94%; (i) DOP 50.31%; (j) DOP 59.72%.

Table 3. FE Ultimate Strength Results of Models

Model No.	P_u	P_u / P_{u0}
Dop=0.00% (Intact)	1377.062	1
Dop=0.66%	1362.77	0.99
Dop=5.24%	1256.87	0.91
Dop=10.24	1156.72	0.84
Dop=17.69	1029.94	0.75
Dop=28.1	880.7	0.64
Dop=34.56	803.07	0.58
Dop=41.94	734.87	0.53
Dop=50.31	656.97	0.48
Dop=59.72	573.36	0.42

P_{uo} = Ultimate strength of intact model
P_u = Ultimate strength of corroded models

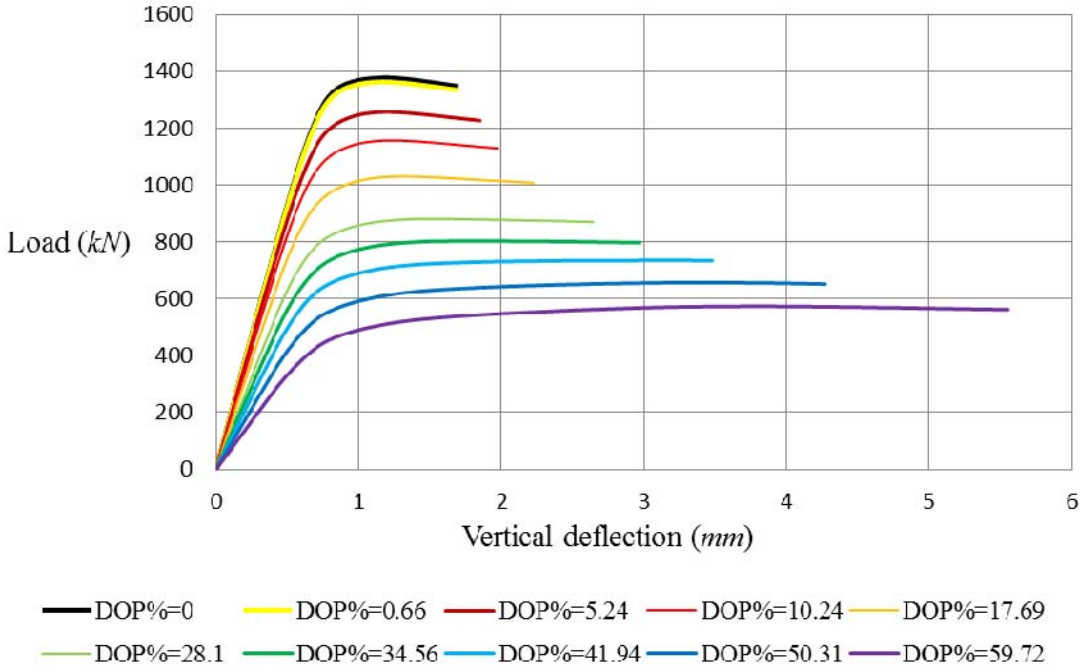

Figure 10. Load – Vertical Deflection Curves for Specimens with Different Corrosion Intensities

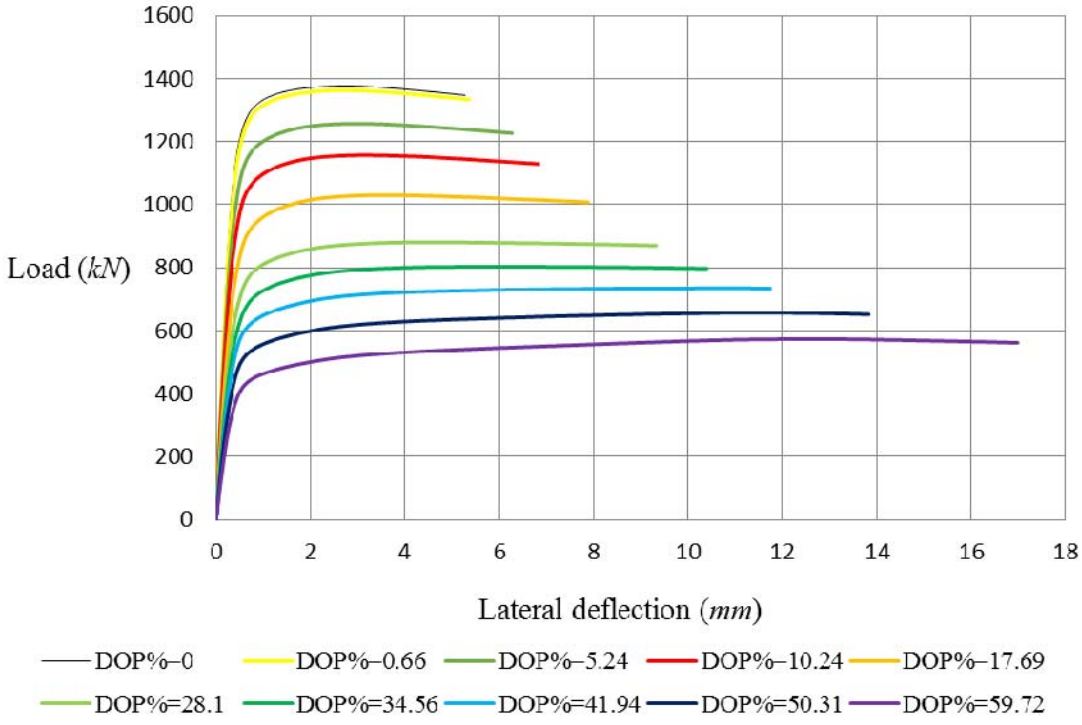

Figure 11. Load – Maximum Lateral Deflection Curves for Specimens with Different Corrosion Intensities

7. ULTIMATE STRENGTH FORMULAE

In case of members with pitting corrosion, which has large unevenness on the surface the evaluation of residual strength is considered to be difficult. In the above-mentioned analyses, rather a complicated method of modeling pitted members is employed. For a practical purpose, a simpler method is desired. In practical application it is desirable to predict a pitted corrosion surface by a surface that is corroded uniformly. This is for the reason that all rules and regulations concerning strength of corroded based-plate structures are based on uniform thickness reduction, and there are several formulations to estimate the ultimate strength of a shape -plate member as a function of thickness. Therefore, in the present paper the attempt is to simulate a pitted corroded web beam with different DOP, with a uniform decreased thickness one.

The load carrying capacity of damaged pitting and uniform corrosion web plate beam has been shown in Figures 12 and 13, respectively. Both of them have been concluded from the obtained results of software. In other word, the thickness of the web plate has been decreased step by step uniformly, and then its residual strength as well as pitted specimens was examined and shown in Figures 12 and 13. The ratio of the ultimate strength to ultimate strength of intact specimen for both pitting corrosion and uniform corrosion has been developed by formulae. It is evident that the web plate beam ultimate strength under patch loading is significantly decreased as the level of DOP increases. The ultimate strength reduction factor for a web plate beam with pit corrosion can be expressed by ANNs of the computed results as a function of the DOP. In this study, the BP network is employed for predicting beam ultimate strength with web pitting corrosion under patch loading. In the next subsection, the theoretical background of the computational methods is briefly explained. As the reduction strength of damaged beams with web uniform corrosion give a semi-linear results, the regression analysis gives the exact and reasonable output.

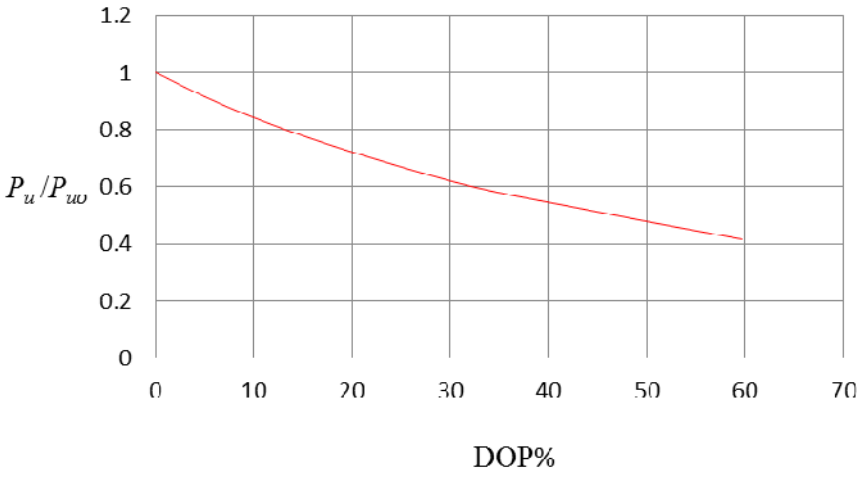

Figure 12. The Ultimate Strength Versus the DOP Ratio for a Steel Web Plate with Pit Corrosion under Patch Loading (P_u, P_{uo} are ultimate strengths for pitted and intact plates, respectively)

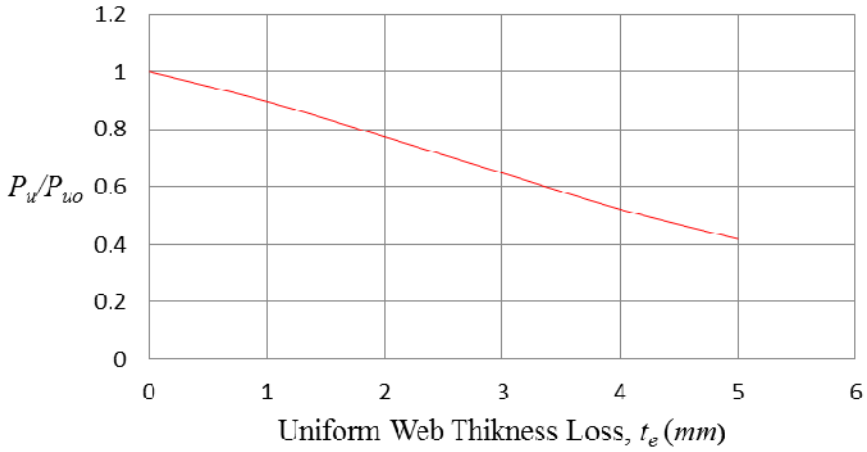

Figure 13. The Ultimate Strength Versus the Web Loss Thickness for a Steel Web Plate with Uniform Corrosion under Patch Loading (P_u, P_{uo} are ultimate compressive strengths for uniform loss thickness and intact plates, respectively)

7.1 ANN Approach

7.1.1 Introduction

A neural network is a massively parallel distributed processor that has a natural propensity for storing experiential knowledge and making it available for use (Haykin [28]). An ANN is a mathematical model that tries to simulate the structure and functionalities of biological neural networks. Basic building block of every artificial neural network is artificial neuron, that is, a simple mathematical model. The Multilayer Perceptron (MLP) procedure produces a predictive model for one or more dependent (target) variables based on the values of the predictor variables. The structure of an MLP consists of the neurons are organized in layers, which are usually fully connected by synapses. A synapse can only connect to subsequent layers. To each of the synapses, a weight is attached indicating the effect of the corresponding neuron. The Multilayer Perceptron (MLP) is the feed forward architecture because the connections in the network flow forward from the input layer to the output layer without any feedback loops. Feed forward networks often have one or more hidden layers of sigmoid neurons followed by an output layer of linear neurons. Multiple layers of neurons with nonlinear transfer functions allow the network to learn nonlinear relationships between input and output vectors. The linear output layer is most often used for function fitting (or nonlinear regression) problems (Neural Network Toolbox [29]).

The back propagation algorithm is used in layered feed forward ANNs. This means that the artificial neurons are organized in layers, and send their signals “forward”, and then the errors are propagated backwards (Rumelhart [30]). The back propagation algorithm is used for multilayered networks and is a supervised learning process. Supervised learning is the most typically neural network setting. These learning algorithms are characterized by the usage of a given output that is compared to the predicted output and by the adaptation of weights according to this comparison. The back propagation algorithm is used to minimize the simulation error until the network converges to the expected performance function. Back propagation looks for the error function minimum in the weight space by applying the gradient descent method (Rojas [31]). Define the error function for the output of neural network:

$$\varepsilon^2 = \left(traget - OUTPUT\right)^2 \tag{14}$$

where ε is error, target is dependent variables and *OUTPUT* is network outputs.

The Multilayer Perceptron (MLP) represents a useful neural network approach for predicting strength of structures. Pu and Mesbahi [32] have proposed a formula for predict ultimate strength of plates using ANN. Hajela and Berke [33] used back propagation neural network to represent the force displacement relationship in static structural analysis. Ok et al. [34] have proposed formulae that can accurately predict the ultimate strength of locally corroded plates under uniaxial in-plane compression. Guzelbey et al. [35] employed back-propagation neural network for estimation of available rotation capacity of wide flange beams. Fonseca et al. [11] predicted steel beam patch load resistance using back-propagation network. Fonseca et al. [36] have also carried out parametric studies based on the neural network model, and furthermore they have proposed a neuro-fuzzy system for the parametric analysis of patch load resistance (Fonseca et al. [37]). On the other hand, Cevik [38] has recently proposed a genetic programming-based formulation for load resistance. Gholizadeh et al. [39] employed back-propagation neural network for predict the load carrying capacity of the castellated steel beams. In this study, the back-propagation network and MLP are employed for predicting the load carrying capacity of damaged steel beams with web pitting corrosion subjected to patch loading.

7.1.2 ANN Structure

Input vector which has been selected for this proposed model is as $\{X_1 = DOP\}$. It is desired to assess the ultimate capacities of steel beams with damaged web plate with different pitting corrosion intensities under patch loading. Using obtained FE results the input vector, $X_1 = DOP$, has ten different values ranging from 0 (for intact specimen) to 59.72 (for maximum damaged specimen). Accordingly, the output vector for the neural network model is selected as $\{P_u / P_{uo}\}$. There is no direct method to select number of nodes in hidden layers. Generally a trial and error method is adopted for arriving at the network configuration. After doing a few trials, it is observed that the network has two hidden layer because this kind of model has been found to have sufficient accuracy and less demand on the amount of training data. There are three neurons in the input layer, e.g. X_1. Also the number of neurons in output layer is equal to one. Each input is weighted with an appropriate *w*. The sum of the weighted inputs and the bias forms the input to the transfer function *f*. Neurons can use any differentiable transfer function *f* to generate their output. The neural network's configuration shown in Figure 14.

The network that is used for this study is a three-layer feed forward network, with hyperbolic tangent transfer functions in the hidden layer and identity transfer functions in the output layer. The outputs using a logistic activation function can be expressed as

$$\frac{P_u}{P_{u0}} = \left| W_3 \times \left(\tanh\left(W_2 \times \begin{bmatrix} 1 \\ \tanh\left(W_1 \times X\right) \end{bmatrix} \right) \right) \right| \tag{15}$$

where

$$W_1 = \begin{bmatrix} b_{A1} & W_{1,A1} \\ b_{A2} & W_{1,A2} \\ b_{A3} & W_{1,A3} \end{bmatrix},$$

$$W_2 = \begin{bmatrix} b_{B1} & W_{A1,B1} & W_{A2,B1} & W_{A3,B1} \\ b_{B2} & W_{A1,B2} & W_{A2,B2} & W_{A3,B2} \\ b_{B3} & W_{A1,B3} & W_{A2,B3} & W_{A3,B3} \end{bmatrix},$$

$$W_3 = \begin{bmatrix} b_{out} & W_{B1,uot} & W_{B2,out} & W_{B3,out} \end{bmatrix},$$

$$X = \begin{bmatrix} 1 & x_1 \end{bmatrix}^T.$$

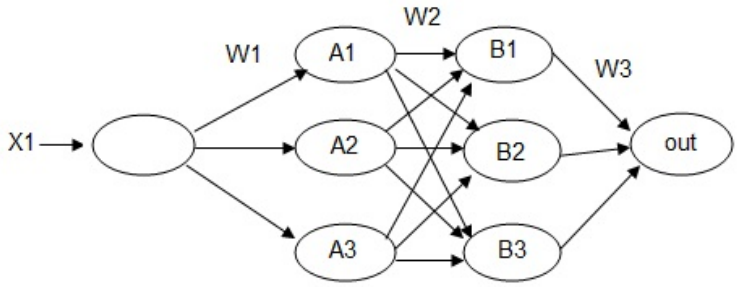

Figure 14. Structure of the Multi-Layer Feed forward Network

7.1.3 Training and Testing of the Network

Back propagation algorithm is used in layered feed forward ANNs for training in present study. During the training procedure, the input and desired data will be repeatedly presented to the network. As the network learns more and more, the error tends to drop towards zero. Updates the weights after passing all training data records, it is most useful for small datasets. The maximum number of epochs is equal to 10000. If the maximum number of epochs is exceeded, then training stops.

7.1.4 Residual Patch Loading Strength Assessment of Damaged Steel Beams with Pitting Corrosion

The ultimate capacity reduction factor (μ) for the deteriorated steel beams web plate with pitting corrosion may be expressed by ANN of the obtained FE results as a function of DOP, as follows:

$$\mu = \frac{P_u}{P_{uo}} \tag{16}$$

where P_{uo} is the ultimate strength for the perfect (i.e., without pit) specimen and P_u is the capacity of damaged beams with different pitting corrosion intensities subjected to patch loading. The derived formula based ANN for predicting strength reduction is expressed as:

$$\mu = \left| W_3 \times \left(\tanh\left(W_2 \times \begin{bmatrix} 1 \\ \tanh\left(W_1 \times X\right) \end{bmatrix} \right) \right) \right| \tag{17}$$

$$X = \begin{bmatrix} 1 & DOP \end{bmatrix}^T,$$

$$W_1 = \begin{bmatrix} -0.061 & 0.009 \\ 0.456 & 0.412 \\ -0.407 & -0.021 \end{bmatrix},$$

$$W_2 = \begin{bmatrix} -0.572 & 0.235 & -0.3 & -0.377 \\ 0-.456 & 0.499 & -0.407 & 0.176 \\ -0.381 & 0.51 & 0.236 & -0.616 \end{bmatrix},$$

$$W_3 = \begin{bmatrix} 0.459 & -0.518 & -0.344 & -0.815 \end{bmatrix}.$$

and then the derived remaining capacity of deteriorated beams (P_u) formula has been expressed as:

$$P_u = \mu \times P_{uo} \tag{18}$$

Table 4 shows summary of the neural network results along with error, relative error or percentage of incorrect predictions, and the training time. Regression analysis of the network outputs and desired outputs (targets) are then carried out to characterize the network accuracy. Figure 15 shows the correlation of both FEM results and ANN outputs. The results are accurate with a mean value of 1. It is evident from Figure15 that neural network is valid for predicting the ultimate residual strength of damaged beams with corroded web subjected to patch loading.

Table 4. Summary of the Neural Network Results for Predict Strength of Beam under Patch Loading

Training	Sample	70%
	Number of epochs	10000
	Sum of Squares Error	1.055E-7
	Relative Error	8.13E-7
	Training Time	0.019 sec
Testing	Sum of Squares Error	8.45E-5
	Sample	30%
	Relative Error	0.002

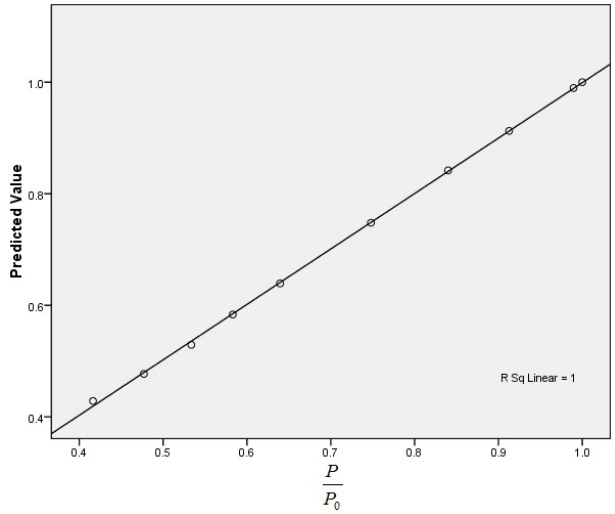

Figure 15. Correlation of FEM Results and ANN Outputs for Ultimate Strength of Beam Web Plate with Pitting Corrosion

It is evident from Figure 16, that Equation 18 is valid for predicting the ultimate strength of a steel web plate with pitting corrosion.

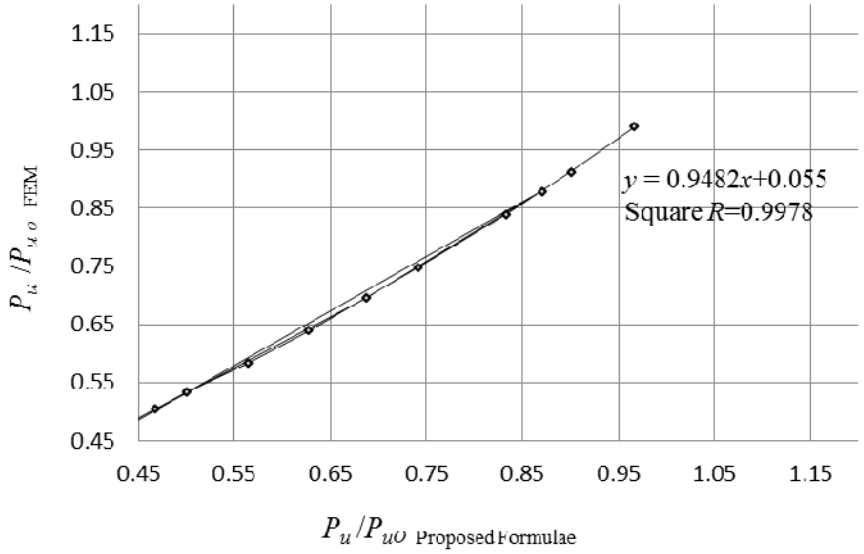

Figure 16. Accuracy of the Proposed Formulae, Equation 18, for the Ultimate Strength Prediction of a Pitted Steel Beam Web Plate with Equivalent Uniform Thickness Loss and under Compressive Loads

7.2 Residual Patch Loading Strength Assessment of Damaged Steel Beams with Uniform Corrosion

It was found that the relationship between the residual capacities of damaged steel plate structures with uniform corrosion is linear (Figure 13), approximately. Therefore, in order to assess the reduction factor formula the ANN and regression approaches give an equal formulation with same accuracy. In this reason the ultimate capacity reduction factor for a damaged web plate beam with uniform corrosion has been expressed by the regression analysis of the obtained FE results as a function of the uniform thickness loss (t_e), as follows:

$$\frac{P_u}{P_{uo}} = -0.119 \times t_e + 1.007, \quad t_e > 0 \tag{19}$$

P_u, P_{uo} are ultimate strengths for corroded and intact beam web plates, respectively, t_e is the uniform web thickness loss.

7.3. Simulation of DOP with an Equivalent Uniform Thickness Loss for Corroded Web Plate Beams in Term of Ultimate Capacity

For general corrosion, which uniformly reduces plate thickness, the plate ultimate strength calculations are typically carried out excluding the thickness loss due to corrosion. For pitting corrosion the strength calculation procedure can be more complex, and for a simplified pessimistic treatment, the corroded plates have been idealized using an equivalent general corrosion. Therefore, for a practical purpose, the equivalent uniform thickness can be an appropriate parameter for the evaluation of the beam capacity of pitted web plates. In this section the effort is to simulate damaged pit corrosion web beams with beams those webs are corroded uniformly by comparing

those ultimate capacities. Equations 18 and 19 summarize the computed results of the remaining ultimate strengths as a function of DOP and uniform thickness loss (t_e). As mentioned, the aim is to represent the pitted web plate beam with a beam that its web thickness is decreased uniformly on all over web surface. Therefore, a formula for simulating DOP to uniform thickness loss can be also derived by fitting curves. Equation 20 presents the equivalent thickness loss as function of pitting corrosion intensities in term of ultimate capacity.

$$t_e = t_w - t_r = 9.4622 - 8.40336 \times \mu_{pit} \tag{20}$$

where, t_e, t_w, and t_r are the uniform web thickness loss, initial web thickness and remaining uniform web thickness, respectively. μ_{pit} is the reduction strength in term of pitting corrosion which is just function of DOP based Equation 16.

8. CONCLUSIONS

The potential for the structural capability degrading effects of corrosion is of profound importance and must be fully understood and reflected in vessel's inspection and maintenance programme. Corrosion has been studied and quantified by many researchers, however its effect on structural integrity is still subject to uncertainty, particularly with regards to localized corrosion. In the present study, for the purpose of investigating the effect of pitting corrosion on ultimate strength of web plate beams subjected to patch loading, a series of ABAQUS elastic–plastic large deflection finite element analyses were carried out, varying the pit corrosion intensities. Obviously the ultimate strength of a web plate beam can be significantly decreased due to pit corrosion as well as general corrosion. In the present study, the ultimate strength reduction factor due to pitting corrosion is empirically derived by Artificial Neural Networks (ANNs) of the obtained FE results as a function of DOP. The ANN based empirical formulae show excellent accuracy to predict the residual strength reduction of corroded web plates beams with pitting corrosion under patch loading. The results and insights developed in the present study will be very useful for damage tolerant design of steel beam structures that are constructed in a very corrosive environment. The beam plate ultimate strength design formulae developed can be utilized for the ultimate limit state based reliability or risk assessment of beam plated structures with web pit corrosion wastage.

While ultimate capacity of a plate element subjected to different loads and boundary conditions with uniform corrosion can be calculated by excluding the thickness loss due to corrosion, predicting the ultimate capacity of a pitted plate is not a simple manner as well as uniform corrosion. It is desired to simulate damaged steel structures with pit corrosion wastage with an equivalent structure which corroded uniformly in term of strength. For a practical purpose, the equivalent uniform thickness can be an appropriate parameter for the evaluation of the beam behavior of pitted web plates. Therefore, based the obtained results of FEM and ANNs a practical formulae for predicting a damaged web pitted plate beam with a measured DOP with a beam that its web corroded uniformly is also developed.

ACKNOWLEDGEMENTS

The authors are pleased to acknowledge the Vali-e-Asr University of Rafsanjan support.

REFERENCES

[1] Nakai, T., Matsushita, H. and Yamamoto, N., "Effect of Pitting Corrosion on Strength of Web Plates Subjected to Patch Loading", Thin-Walled Structures, 2006, Vol. 44, pp. 10-19.

[2] Nakai, T., Matsushita, H., Yamamoto, N. and Hironori A., "Effect of Pitting Corrosion on Local Strength of Hold Frames of Bulk Carriers (1st report)", Thin-Walled Structures, 2006, Vol. 44, pp. 10-19.

[3] Nakai, T., Matsushita, H. and Yamamoto, N., "Effect of Pitting Corrosion on the Ultimate Strength of Steel Plates Subjected to In-Plane Compression and Bending". Journal of Marine Science and Technology, 2006, Vol. 11, No. 1, pp. 52-64.

[4] Paik, J.K., Lee, J.M. and Ko, M.J., "Ultimate Compressive Strength of Plate Elements with Pit Corrosion Wastage", Journal of Engineering Maritime Environment, 2003, Vol. 217, No. M4, pp. 185-200.

[5] Paik, J.K., Lee, J.M. and Ko, M.J., "Ultimate Shear Strength of Plate Elements with Pit Corrosion Wastage", Thin-Walled Structures, 2004, Vol. 42, No. 8, pp. 1161-76.

[6] Sharifi, Y. and Paik, J.K., "Ultimate Strength Reliability Analysis of Corroded Steel-box Girder Bridges", Thin-Walled Structures, 2011, Vol. 49, No. 1, pp. 157-166.

[7] Sharifi, Y. and Paik, J.K., "Environmental Effects on Ultimate Strength Reliability of Corroded Steel Box Girder Bridges", Structural Longevity, 2010, Vol. 18, No. 1, pp. 1-20.

[8] Sharifi, Y., "Reliability of Deteriorating Steel Box-Girder Bridges under Pitting Corrosion", Advanced Steel Construction, 2011, Vol. 7, No. 3, pp. 220-238.

[9] Sharifi, Y. and Tohidi, S., "Lateral-torsional buckling capacity assessment of web opening steel girders by artificial neural networks–elastic investigation", Frontiers of Structural and Civil Engineering, 2014, Vol. 8, No. 2, pp. 167–177.

[10] Nethercot, D.A., "Limit States Design of Structural Steelwork", 3rd ed. London, UK: Spon Press, 2001.

[11] Adeli, H., Hung, S.L., "Machine Learning: Neural Networks, Genetic Algorithms, and Fuzzy Systems", New York, Wiley, 1995.

[12] Fonseca, E.T., Vellasco, P.C.G., Andrade, S.A.L. and Vellasco, M.M.B.R., "Neural Network Evaluation of Steel Beam Patch Load Capacity", Advances in Engineering Software, 2003, Vol. 34, pp. 763–72.

[13] Jang, J.S.R., "ANFIS: Adaptive-Network-Based Fuzzy Inference Systems", IEEE Transactions on Systems, Man and Cybernetics, 1993, Vol. 23, pp. 665–85.

[14] Hagan, M.T. and Menhaj, M., "Training Feed-Forward Networks with the Marquardt Algorithm", IEEE Transactions on Neural Networks, 1999, Vol. 5, pp. 989–93.

[15] Guzelbey IH, Cevik bA, Gogus MT. Prediction of rotation capacity of wide flange beams using neural networks. Journal of Constructional Steel Research 2006; 62:950–61.

[16] EN 1993-1-1 Eurocode 3: Design of Steel Structures, Part 1.1 General Rules and Rules for Buildings, British Standard Institution, London 2005.

[17] Paik, J.K. and Thayamballi, A.K., "Ultimate Limit State Design of Steel-Plated Structures", John Wiley & Sons, Ltd., Hoboken, New Jersey, USA, 2003.

[18] Dogaki, M., Yonezawa, H. and Tanabe, T., "Ultimate Strength of Plate Girders with Longitudinal Stiffeners under Patch Loading", Proceedings of the 3rd Pacific Structural Steel Conference, The Japan Society of Steel Construction, Tokyo, 26-28 October, 1992, pp. 507-514.

[19] Dogaki, M., Nishijima, Y. and Yonezawa, H., "Nonlinear Behaviour of Longitudinally stiffened Webs in Combined Patch Loading and Bending", Constructional Steel Design: World Developments, Elsevier Applied Science 1992, London, pp. 141-150.

[20] Takimoto, T., "Plate Girders under Patch Loading", Ultimate Strength and Design of Steel Structures, The Japan Society of Civil Engineers, Tokyo 1994, pp. 122-127 (in Japanese).

[21] Roberts, T.M. and Rockey, K.C., "A Mechanism Solution for Predicting the Collapse Loads

of Slender Plate Girders when Subjected to In-Plane Patch Loading", Proc Inst Civ Eng Struct Build, 1979, Vol. 67, No. 2, pp. 155–75.

[22] Bergfelt, A., "Patch Loading On a Slender Web-Influence of Horizontal and Vertical Web Stiffeners on the Load Carrying Capacity", Chalmers University of Technology, Dept. of Structural Engineering, Div. of Steel and Timber Structures, Publ. S79:1, Goteborg, 1979.

[23] Eurocode 3: Design of Steel Structures, Part 1–5: General Rules, Supplementary Rules For Planar Plated Structures without Transverse Loading, ENV 1993-1-5:1997 E, 2006.

[24] Lagerqvist, O. and Johansson, B., "Resistance of I-Girders to Concentrated Loads", Journal of Constructional Steel Research, 1996, Vol. 39, No. 2, pp. 87–119.

[25] ABAQUS user's manual, version 6.9. Pawtucket, RI: Hibbit, Karlsson & Sorenson, 2005.

[26] Saad-Eldeen, S., Garbatov, Y. and Guedes Soares, C., "Compressive Strength Assessment of a Moderately Corroded Box Girder", Marine Systems and Ocean Technology, 2011, Vol. 6, pp. 27–33.

[27] Saad-Eldeen, S., Garbatov, Y. and Guedes Soares, C., "Experimental Assessment of the Ultimate Strength of a Box Girder Subjected to Severe Corrosion", Marine Structures, 2011, Vol. 24, pp. 338–57.

[28] Haykin, S., "Neural Networks: a Comprehensive Foundation", 2nd ed. New York: Macmillan College Publishing; 1998.

[29] Neural Network Toolbox 7 User's Guide, Mark Hudson Beale Martin T. Hagan Howard B. Demuth, 2010.

[30] Rumelhart, D. and McClelland, J., "Parallel Distributed Processing", MIT Press, Cambridge, Mass; 1986.

[31] Rojas, R., "Neural Networks- A Systematic Introduction Springer- Verlag", 1996.

[32] Pu, Y. and Mesbahi, E., "Application of Artificial Neural Networks to Evaluation of Ultimate Strength of Steel Panels", Engineering Structures, 2006, Vol. 28, pp.1190–1196.

[33] Hajela, P. and Berke, L. "Neurobiological Computational Models in Structural Analysis and Design", Computers and Structures, 1991, Vol. 41, No. 4, pp. 657–667.

[34] Ok, D., Pu, Y. and Incecik, A., "Artificial Neural Networks and Their Application to Assessment of Ultimate Strength of Plates with Pitting Corrosion", Ocean Engineering, 2006, Vol. 34, pp. 2222–2230.

[35] Guzelbey, I.H., Cevikb, A. and Gogus, M.T., "Prediction of Rotation Capacity of Wide Flange Beams Using Neural Networks", Journal of Constructional Steel Research, 2006, Vol. 62, pp. 950–61.

[36] Fonseca, E.T., Vellasco, P.C.S., Andrade, S.A.L. and Vellasco, M.M.B.R. "A Patch Load Parametric Analysis using Neural Networks", Journal of Constructional Steel Research, 2003, Vol. 59, No. 2, pp. 251–67.

[37] Fonseca E.T., Andrade, S.A.L. and Vellasco, P.C.G.D., "A Parametric Analysis of the Patch Load Behaviour using a Neuro-Fuzzy System", Journal of Constructional Steel Research, 2007, Vol. 63, pp. 194–210.

[38] Çevik, A.A., "New Formulation for Longitudinally Stiffened Webs Subjected to Patch Loading", Journal of Constructional Steel Research, 2007, Vol. 63, pp. 1328–40.

[39] Gholizadeh, S., Pirmoz, A. and Attarnejad, R., "Assessment of Load Carrying Capacity of Castellated Steel Beams by Neural Networks", Journal of Constructional Steel Research, 2011, Vol. 67, pp. 770–779.

SEISMIC BEHAVIOR OF THROUGH-DIAPHRAGM CONNECTIONS BETWEEN CFRT COLUMNS AND STEEL BEAMS-EXPERIMENTAL STUDY

Ying Qin[1], Zhihua Chen[2,*], Xiaodun Wang[3] and Ting Zhou[4]

[1] *Graduate Research Assistant, Department of Civil Engineering, Tianjin University, Tianjin, China, and Visiting Research Scholar, Department of Civil Engineering, Johns Hopkins University, Baltimore, MD, USA*
[2] *Professor, Key Laboratory of Coast Civil Structure Safety of China Ministry of Education, Tianjin University, Tianjin, China, and Department of Civil Engineering, Tianjin University, Tianjin, China*
[3] *Associate Professor, Department of Civil Engineering, Tianjin University, Tianjin, China*
[4] *PhD, Department of Civil Engineering, Tianjin University, Tianjin, China*
**(Corresponding author: E-mail: zhchen@tju.edu.cn)*

Received: 1 August 2013; Revised: 18 September 2013; Accepted: 23 September 2013

ABSTRACT: This paper is an extension study to an experimental program involving one traditional and three novel through-diaphragm connections between concrete-filled rectangular tubular columns and steel H-beams. The proposed connection types utilize tapered diaphragm or triangular plates at the end of the beam to improve the seismic performance of traditional through-diaphragm connections. Based on the experimental results, the lateral force versus beam-column deformation response was assessed and the shear force versus shear distortion relationship in the panel zone was evaluated. It was observed that the improvement in connection details significantly enhanced the rotation capacity and shear stiffness. The deformation of the connections was also analyzed in terms of the contribution of the column, the beam, and the joint. In addition, the force transfer mechanism in the connections was investigated by analysis of the strain distribution The test results indicate that the proposed through-diaphragm connections are able to alleviate the stress concentration in the load transfer path and exhibit better seismic behavior. As a result, it can be concluded that the proposed connections are more suitable for applications in moment resisting frames in seismic regions.

Keywords: Through-diaphragm connections, Concrete-filled rectangular tubular column, Seismic performance, Experimental behavior, Strain distribution

1. INTRODUCTION

Concrete-filled rectangular tubular (CFRT) columns have been widely used in practical applications these days due to their benefits of excellent mechanical behavior and architecturally pleasing advantages.

A large amount of research has been conducted on the connections between CFRT columns and steel H-beams. Previous investigation on the experimental behavior of H-beam-to-CFST column connections has included that of Kang et al. [1], Varma et al. [2], Ricles et al. [3], Shin et al. [4], Cheng et al. [5], Wu et al. [6], Nie et al. [7], Wang et al [8], Park et al. [9], and Qin et al. [10-11]. Theoretical study on the flexural strength and shear strength has been conducted by Kawano et al. [12], Koester [13], Lu et al. [14], Morino et al. [15], Fukumoto et al. [16], Park et al. [17], Jiang et al. [18], Nie et al. [19], Rong et al. [20], and Qin et al. [21-23]. Additionally, various connection alternatives have been proposed and explored by researchers, such as the application of blind bolt [24-26], combined channel angle connections [27], and through-bolt connections [28]. Damage assessment [29], computationally performance simulation [30], and design approach investigation [31] represent other areas of interest. Several state-of-the-art reports and papers also presented a large number of research results on CFRT column-to-H-beam connections [32-36].

However, few studies have considered the improvement of the through-diaphragm connections or the seismic behavior of the panel zone. As a part of investigations on the seismic behavior of CFRT connections, in this research, one traditional and three improved through-diaphragm specimens were tested to evaluate the seismic performance of the connections subjected to cyclic loading. The experimental results including moment-rotation response, strength and stiffness degradation, ductility, drift rotation and energy dissipation have been presented in a parallel paper [10]. An extension to this work which considers the behavior of panel zone, the deformation, and the force transfer mechanism is described here.

2. CFRT CONNECTIONS

2.1 Traditional Connection Types

Three conventional connections are currently used for CFRT column moment resisting frame (MRF) system in some Asian countries such as China, Japan and Korea [37]. As shown in Figure 1, each employs an internal diaphragm, an external diaphragm, or a through diaphragm.

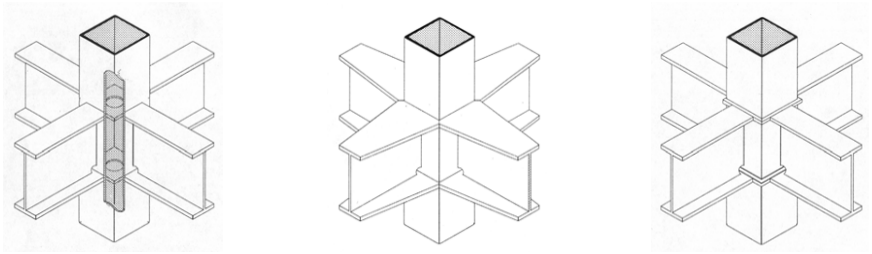

(a) Internal diaphragm (b) External diaphragm (c) Through diaphragm

Figure 1. Conventional Details of Connections to CFRT Columns

The internal diaphragm connection is made by inserting the diaphragm into the steel tube and connecting the beam flanges to the tube surface, as shown in Figure 1(a). It has the merit of not interfering with the finishing materials outside the column. However, necessary measures should be taken when infilling concrete into the steel tubes, in order to prevent the occurrence of voids under the diaphragm. In this case, the tensile force transferred from beam flanges is directly delivered to column flanges. Since the internal diaphragm is welded around its perimeter to the steel tube and the steel tube column restrains the deformation of the diaphragm, most of the deformation in the panel zone is concentrated along the direction of the thickness of the column flanges. When the tensile force is large enough, the failure of the connections may accompany punching shear, which induces the fracture of the weld between the beam flanges and column flanges. Additionally, lamellar tearing of the column flange may occur at the same time. This failure mode was observed in the simple tension test and cyclic loading test conducted by Choi et al. [38], as shown in Figure 2(a).

The external diaphragm connection detail, as shown in Figure 1(b), attaches the diaphragm to the outside of the steel tube and needs no cutting of steel tube for fabrication. However, the external diaphragm lacks aesthetics and may have limitations on the size of the diaphragm for a joint of an exterior frame. Due to the abrupt change of the cross-sectional area between the beam flange and external diaphragm, the stress and deformation concentration there causes the failure of groove weld [39].

The detail of through diaphragm connection, as shown in Figure 1(c), requires diaphragms penetrating the steel tube and beam flanges directly welding to the through diaphragm. In this case, the tensile force is transferred from the beam flanges to the through diaphragm. This detail significantly moves the plastic hinge away from the steel tube surface and smooth the load transfer path, although it involves much on-site welding and imposes construction complication. The failure of connections is often caused by the crack developed in the groove weld between beam flanges and through diaphragm, as shown in Figure 2(b) [38].

(a) Internal diaphragm

(b) Through diaphragm

Figure 2. Example of Connection Failure

2.2 Proposed Connections with through Diaphragm

To avoid the abrupt change of cross section between the beam flanges and through diaphragm and reduce the stress concentration there, three improved through-diaphragm connection details were studied herein. Specimen JD-2 had a tapered diaphragm with an extended length of 320mm, as illustrated in Figure 3(b). In Specimen JD-3 and JD-4, the through-diaphragm penetrated the steel tube and extended a length of 20 mm. Horizontal haunches were attached to the beam flange to form the tapered flange at the beam end as shown in Figure 3(c) and (d). These details were both designed to transfer the tension force from the beam flange directly to the sides of the steel tube and provide a more gradual transition in the geometry of the connection region. The weld access hole shown in Figure 4(a) was used in specimen JD-1 and JD-2, while that in Figure 4(b) was used for specimen JD-3 and JD-4. A more detailed description on the specimen design can be found in [10].

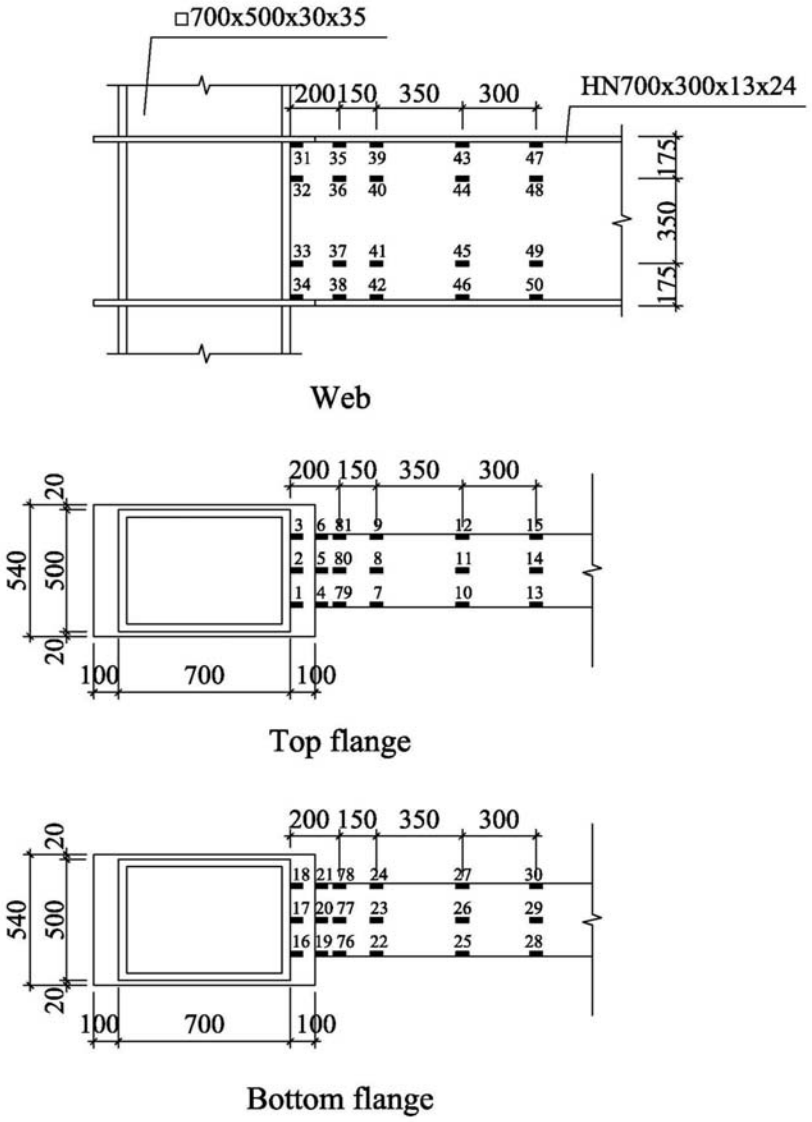

(a) Specimen JD-1

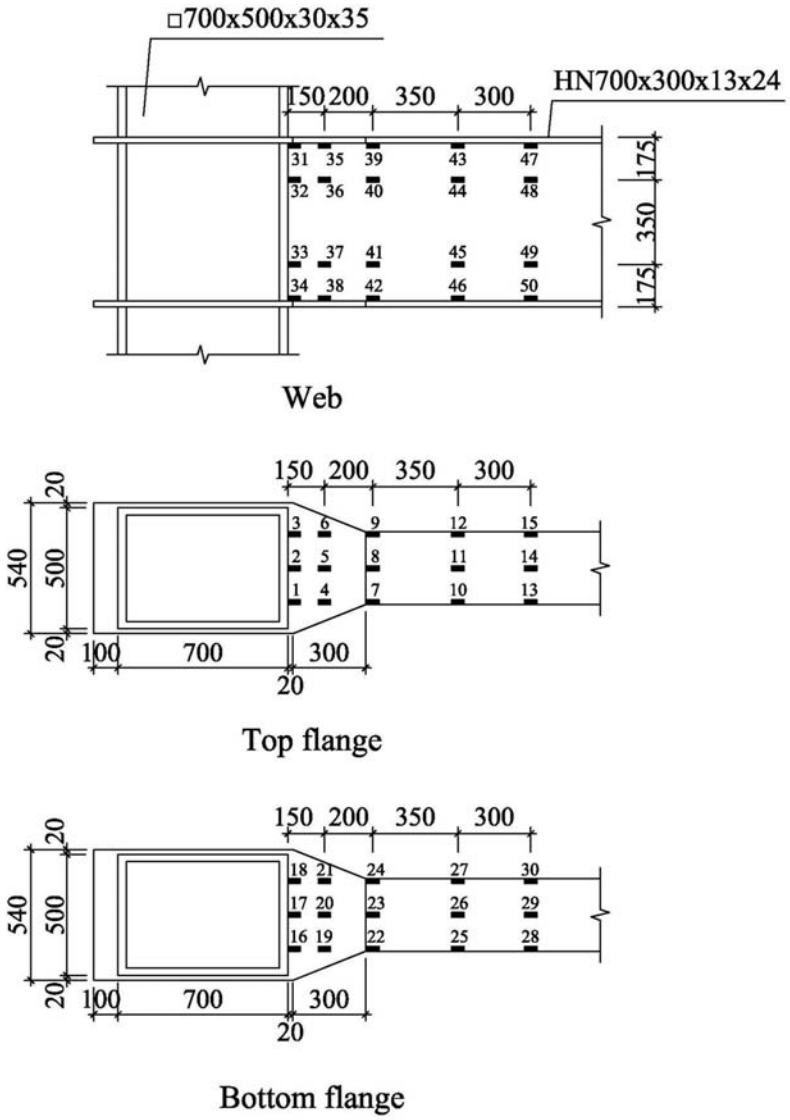

(b) Specimen JD-2

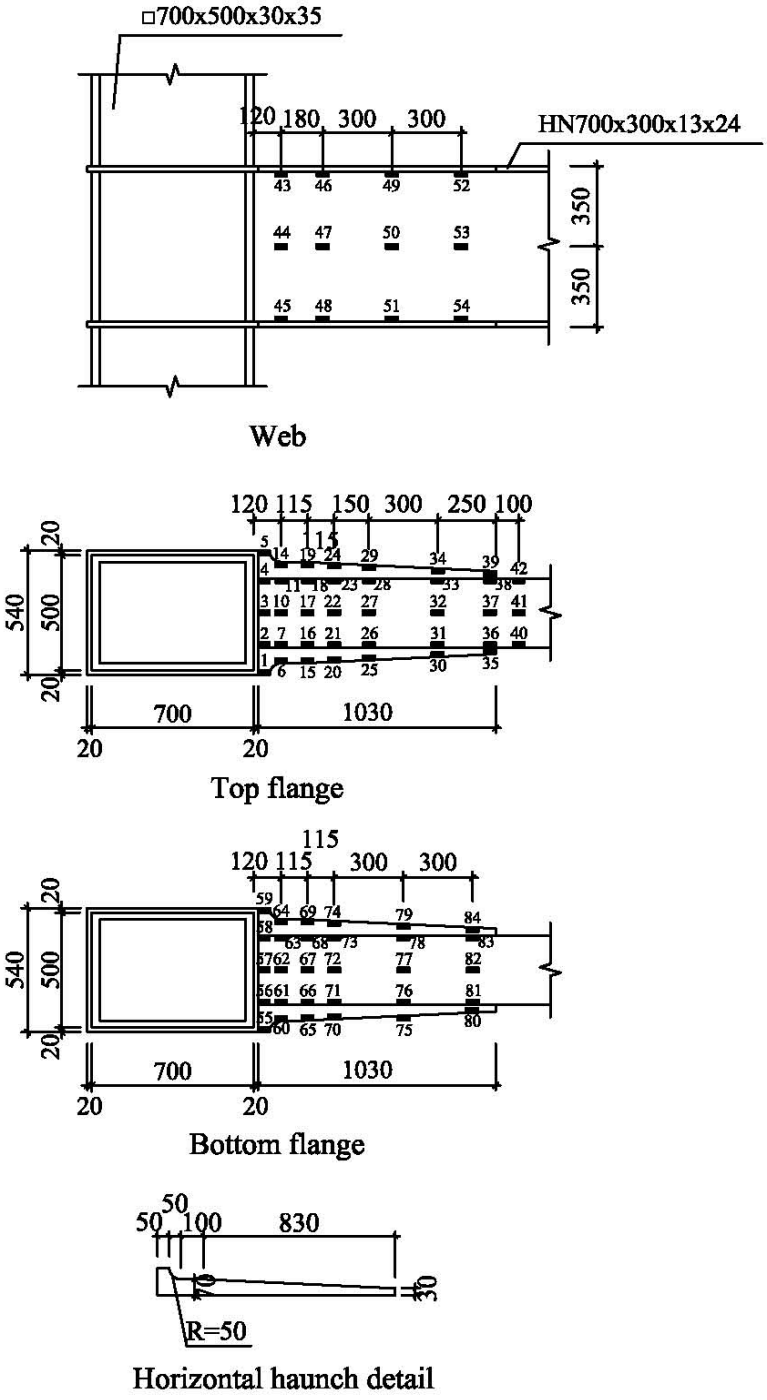

(c) Specimen JD-3

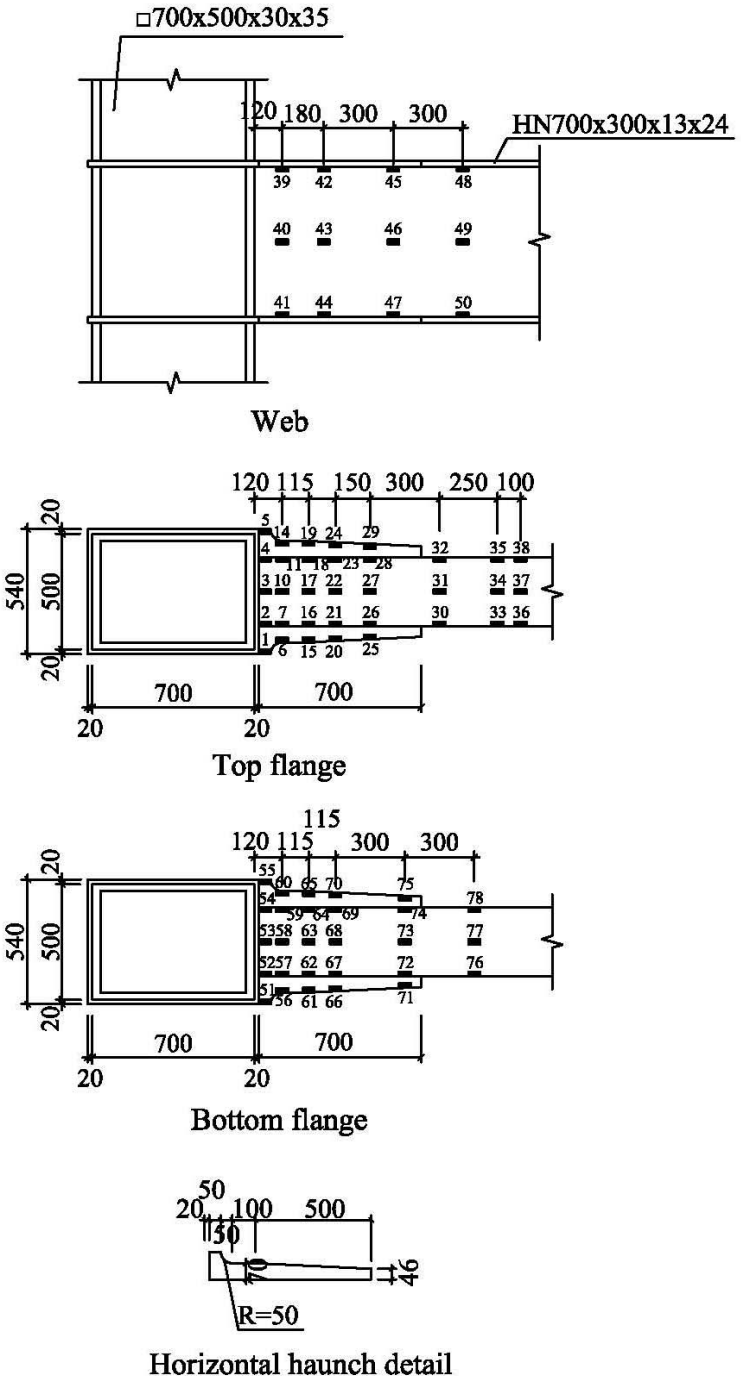

(d) Specimen JD-4

Figure 3. Details of Specimens and Layout of Strain Gauge

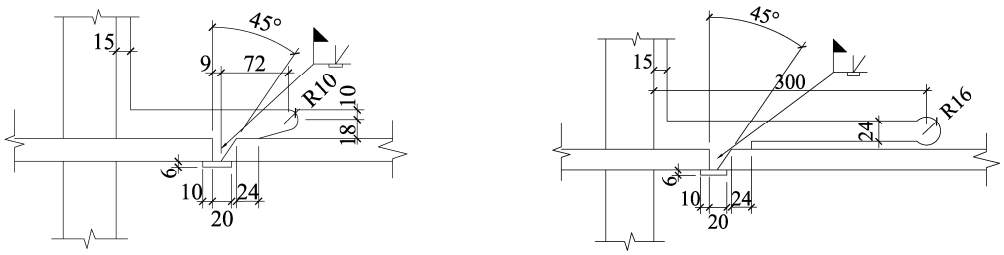

(a) Type 1 (b) Type 2

Figure 4. Weld Access Hole

3. EXPERIMENTAL PROGRAM AND TEST RESULTS

3.1 Experimental Program

The test specimens were constructed in a tee shape to simulate the external connection of a steel MRF with a height of 4.2 m and a bay width of 7.2 m. Four full-scale beam-to-column connections were tested under quasi-static cyclic loading to study the hysteretic behavior of the existing and proposed through-diaphragm connections to CFRT columns. The geometric detail of the connections and the test setup are given in Figures 3 and 5, respectively. The pin boundary condition was created where the inflection points were assumed. The horizontal cyclic loading was applied to the specimen by an actuator bolted to the reaction wall. The lateral loading procedure of the specimens was generally according to recommendations provided by ANSI/AISC 341-10 [40]. The layout of the displacement transducers is illustrated in Figure 6. The detailed description of the test program is described in the parallel paper [10].

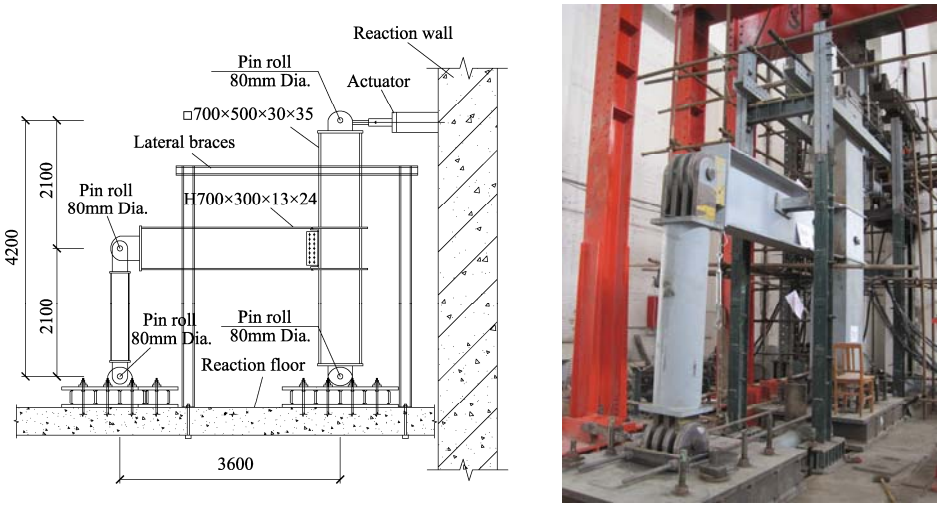

Figure 5. Test Setup

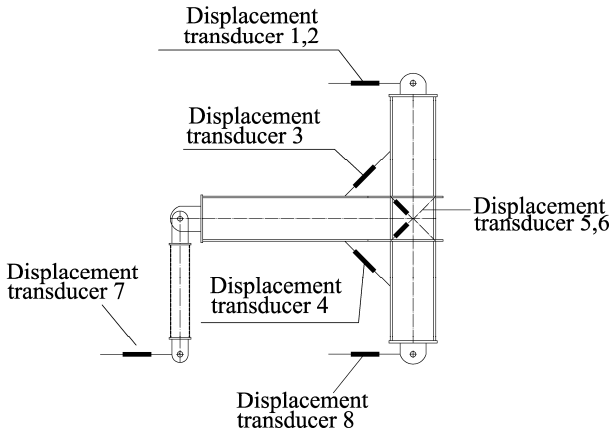

Figure 6. Arrangement of Displacement Transducers

3.2 Lateral Force Versus Beam-Column Deformation Relationship

The lateral load versus beam-column deformation relationship is one of the principal ways of assessing the seismic behavior of the connection. The force-deformation curves are shown in Figure 7, in which force is the horizontal load applied to the top of the column and deformation is the rotational angle of the beam-column measured by displacement transducer 3 and 4, as shown in Figure 6.

It can be seen that the hysteresis loops of all the specimens are in a shuttle shape, stable, plentiful and energy dissipative. A ductile behavior is developed as the number of cycle increases and the cyclic loading process continues. No obvious strength or stiffness degradation is observed in the test. As a consequence, the specimens exhibit satisfactory seismic performance. Meanwhile, it is observed that the hysteresis behavior of proposed connections (Specimen JD-2-JD-4) achieved a higher rotation capacity compared to the traditional through-diaphragm connection (Specimen JD-1). This enhanced behavior is attributed to the additional seismic resistance that is provided by the tapered diaphragm or the triangular plates at the end of the steel beam.

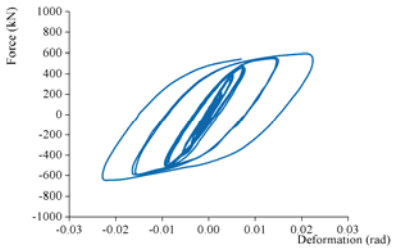

(a) Specimen JD-1

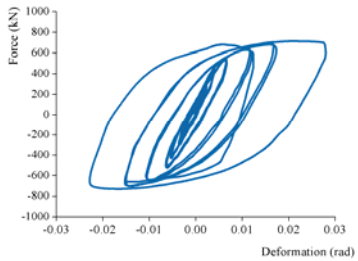

(b) Specimen JD-2

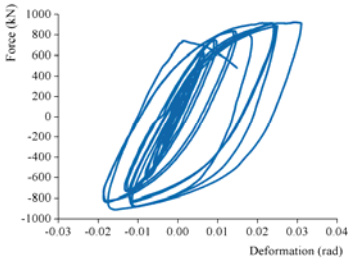

(c) Specimen JD-3

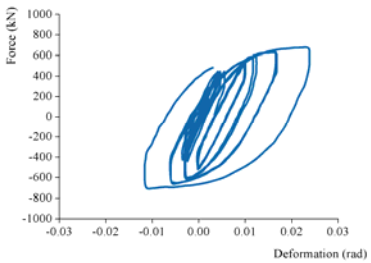

(d) Specimen JD-4

Figure 7. Lateral Force Versus Beam-column Deformation Curves

3.3 $Q_j - \gamma_j$ Curves

Regarding through-diaphragm connections, the cyclic behavior is governed by the panel zone and/or by the beam end. Considering the strengthening and stiffening effect of through-diaphragm, the cyclic response of the connections is given by the cyclic shear behavior of the panel zone, by the cyclic bending behavior of the connected steel beam, or by a combination of both [40]. In order to evaluate the performance of the panel zone of the connection, $Q_j - \gamma_j$ hysteresis loops of the specimens are shown in Figure 9. Q_j is the shear force in the panel zone, γ_j is the shear deformation in the panel zone as shown in Figure 8 and can be determined by Eq. 1.

$$\gamma_j = \frac{1}{2}(\Delta_1+\Delta_2+\Delta_3+\Delta_4)\frac{\sqrt{a^2+b^2}}{ab} \tag{1}$$

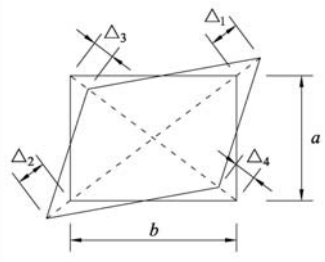

Figure 8. Shear Distortion in the Panel Zone

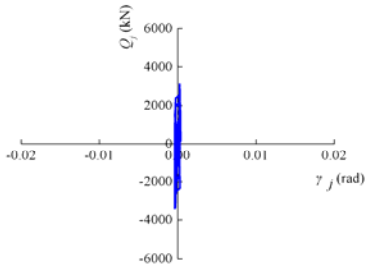

(a) Specimen JD-1

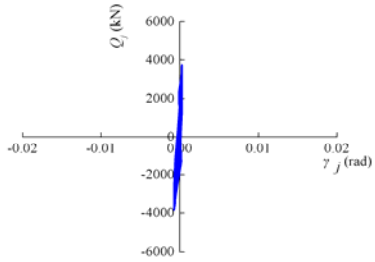

(b) Specimen JD-2

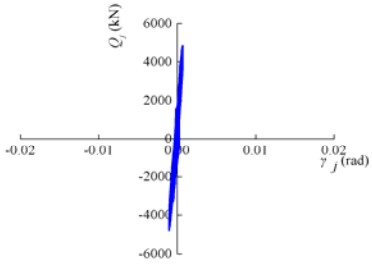

(c) Specimen JD-3

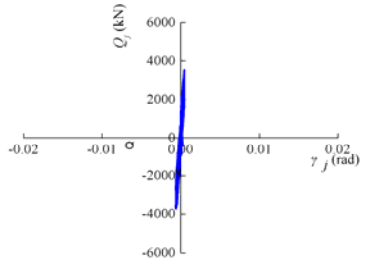

(d) Specimen JD-4

Figure 9. $Q_j - \gamma_j$ Curves

The hysteresis curves of all the specimens are almost linear, which demonstrated that the panel zone of connections is still in the elastic range. The maximum shear distortions of the specimens are less than 8×10^{-4} rad. Consequently, it can be concluded that all the specimens have strong panel zone and the energy absorbed is largely attributed to the components surrounding the panel zone.

The shear stiffness of these four connections was found to range from 6,639,545 kN/rad (Specimen JD-1) to 7,532,542 kN/rad (Specimen JD-4), where the 11% and 13% increase in stiffness in Specimen JD-3 and JD-4, respectively, is associated with the addition of the horizontal stiffeners to the through-diaphragm connection detail. The tapered through-diaphragm connection detail (Specimen JD-2) had a 12% greater stiffness than Specimen JD-1. Therefore, it indicates that the connection detail provided a comparable stiffness to that of the traditional through-diaphragm connection for steel beams-to-CFRT columns.

3.4 Deformation Analysis

When the specimens are subjected to lateral cyclic loading, the deformation of the connections is based on the contribution of the CFRT columns, the steel beam, and the panel zone. As shown in Figure 10, the displacement at the top of the column Δ is the summation of the displacement caused by the column ($\triangle_c$), the beam ($\triangle_b$), and the panel zone ($\triangle_j$). Faella and Rizzano [40] pointed out that from the theoretical point of view, the rotation of beams and panel zones is of concern in the case of through-diaphragm connections, because in this case, yielding occurs at the member ends.

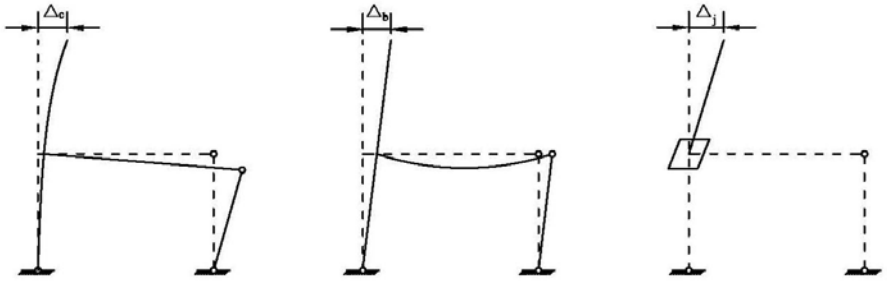

Figure 10. Deformation Analysis of An Exterior Connection

As shown in Figure 6, Δ is measured by transducer 1 and 2; $\triangle_j$ is obtained by transducer 5 and 6; The total displacement of beam end and panel zone $\triangle_{bj}$ is determined by transducer 3 and 4. Thus, $\triangle_b$ can be calculated by Eq. 2. Another two transducers were installed at the bottom of the box foundations to obtain the displacement there. The deformation analysis results are shown in Figure 11, where $r_{\Delta j} = \Delta_j / \Delta$, $r_{\Delta b} = \Delta_b / \Delta$.

$$\Delta_b = \Delta_{bj} - \Delta_j \tag{2}$$

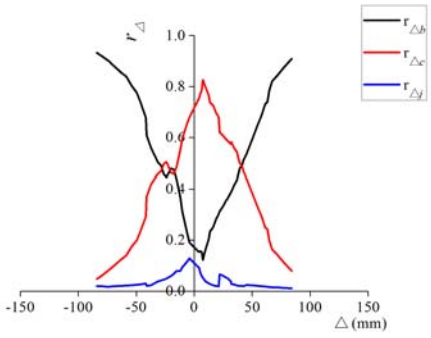

(a) Specimen JD-1

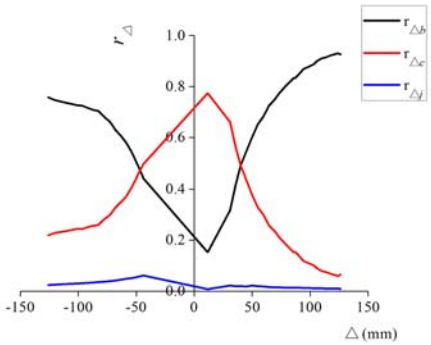

(b) Specimen JD-2

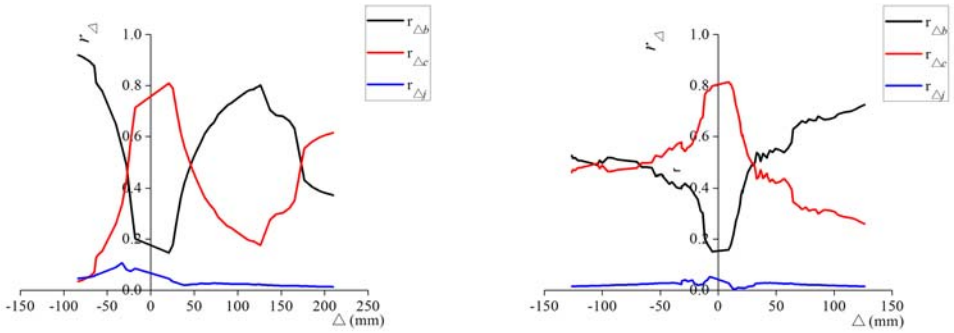

(a) Specimen JD-3 (b) Specimen JD-4

Figure 11. $r_{\Delta} - \Delta$ Curves

The displacement induced by the deformation of panel zone is the smallest. During the test, the shear deformation of the panel zone developed insufficiently and the value of $\triangle_j$ remained at an extremely low level. In general, the displacement caused by beam end grew larger with the continuing loading process. At the end of the test, the ratio of $\triangle_b$ to $\triangle$ exceeded 80% in most cases.

4. STRAIN DISTRIBUTIONS

Strain gauges were used to monitor the strains in the beam, through-diaphragm, and steel tube. Placement of the beam strain gauges was mainly concentrated in the beam closer to the connection. All readings were recorded using a computer. The layout of the strain gauges is illustrated in Figure 3. During the test, the strain distribution of Specimen JD-4 was similar to that of Specimen JD-3. Thus, for ease of presentation, only the strains of Specimen JD-1, JD-2 and JD-3 are discussed below.

4.1 Strains of Specimen JD-1

The distribution of the strains in the beam flange along the transverse direction are shown in Figure 12(a)-(e). The yield strain of the beam is 1740 $\mu\varepsilon$. The test results showed that except for the strains near the complete joint penetration weld, the strains were uniformly distributed along the width of beam flange until the failure occurred. However, it was determined from Figure 12(b) that a non-uniform strain distribution developed across the width of the beam flange adjacent to the groove weld when the story drift angle exceeded 1.0% rad, and the value of strain at the side of beam flange was larger than that in the center. This is because the weld access hole there reduces the beam web section, which provides a weaker support to the center of flange of the beam and induces more force transferred through the sides of beam flange. Meanwhile, the strain in the center of the through-diaphragm was greater than that at the side. This phenomenon illustrates that the force from the beam flange did not sufficiently transfer to the part of column wall far away from the center.

Figure 12(f) shows the response of the strains in the beam flange along the longitudinal direction. It should be noted that the strains decreased steadily as the distance between the measured location and column face increased; the through-diaphragm and the end of the beam flange started to yield when the story drift angle was greater than 0.75%. Additionally, there is a significant increase in the strain at the location between the beam flange and the through-diaphragm because the abrupt cross-section change there results in strain concentration.

Figure 12(g)-(k) illustrate the strains of the beam web, where the positive values denote tensile strains, while the negative values denote compressive strains. The behavior was plotted at the point of each story drift. It demonstrates that the strains were linearly distributed over the section of the beam when the story drift angle was less than 1.0% rad. However, the distribution of strains over the section at a distance 20 mm and 200 mm away from the column face became non-linear when the story drift angle was greater than 1.0% rad, which indicates yielding began to develop in the web. This can also be seen from the slope change on moment-rotation curve.

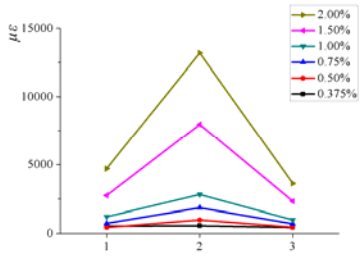

(a) Strain gauge No. 1-3

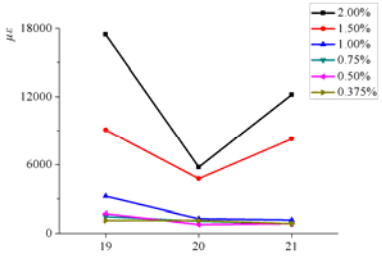

(b) Strain gauge No. 19-21

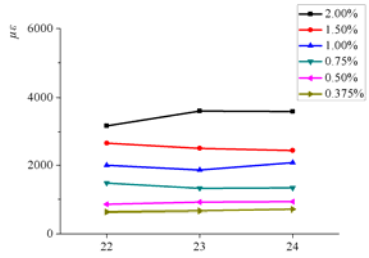

(c) Strain gauge No. 22-24

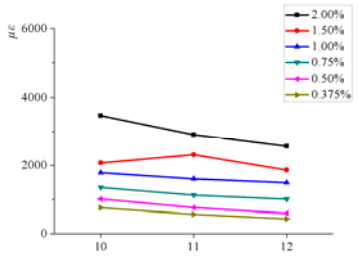

(d) Strain gauge No. 10-12

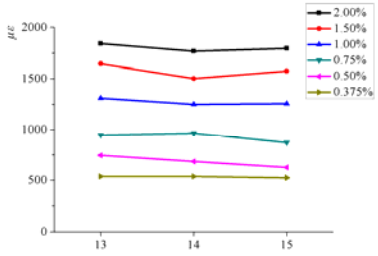

(e) Strain gauge No. 13-15

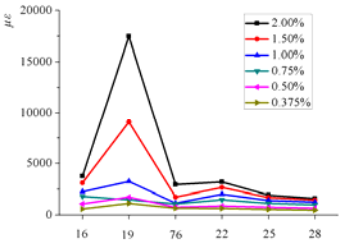

(f) Strain gauge No. 16,19,76,22,25,28

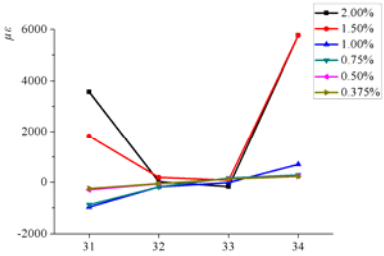

(g) Strain gauge No. 31-34

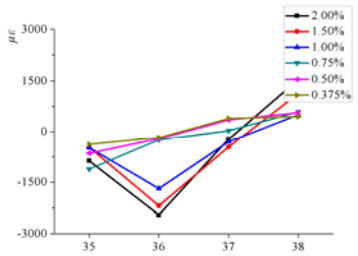

(h) Strain gauge No. 35-38

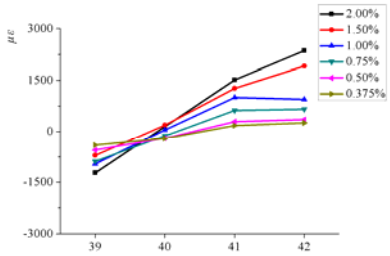

(i) Strain gauge No. 39-42

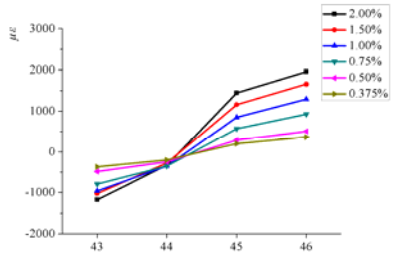

(j) Strain gauge No. 43-46

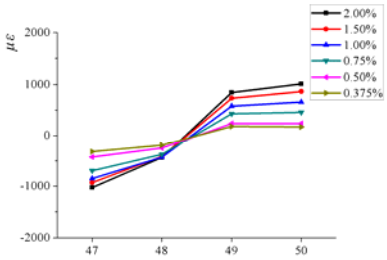

(k) Strain gauge No. 47-50

Figure 12. Strain Distribution of Specimen JD-1

4.2 Strains of Specimen JD-2

The strain distribution of Specimen JD-2 across the beam's flange shows a very consistent and similar behavior to that of Specimen JD-1, as shown in Figure 13(a)-(e). The cross-section strains were uniformly distributed until the story drift angle arrived at 3.0%. However, the distribution of strains became non-uniform when the story drift angle exceeded 3.0% rad. Compared to Specimen JD-1, the distribution of strains of Specimen JD-2 in the through-diaphragm near the column face shows different results. The strain level at the side was obviously higher than that in the center. This can be explained by the fact that the tapered through-diaphragm helps the force transfer to a larger part of column tube.

The strain distribution in the beam flange along the beam length is illustrated in Figure 12(f). It can be seen that the tapered diaphragm provides a more gradual transition in the force transfer path, although the strain concentration still developed at the location between the beam and the diaphragm.

The strain distribution shown in Figure 12(g)-(j) indicate that yielding began to develop at a distance 150 mm away from the column tube face. As the test progressed, the beam web had yield for a distance of up to 350 mm before the connection failed. The same figure also shows that the maximum strain located 700 mm from column face is almost equal to the yield strain at the ultimate load. This result implies that this tapered plates connection detail significantly helps move the plastic hinge away from the column and the length of yielded region was less than the depth of beam.

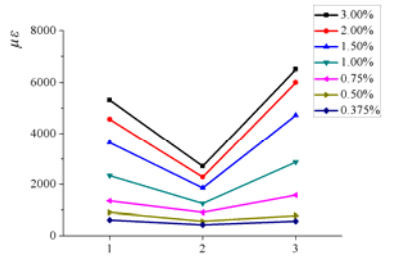

(a) Strain gauge No. 1-3

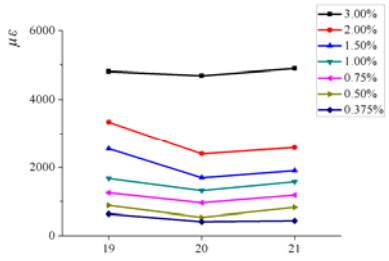

(b) Strain gauge No. 19-21

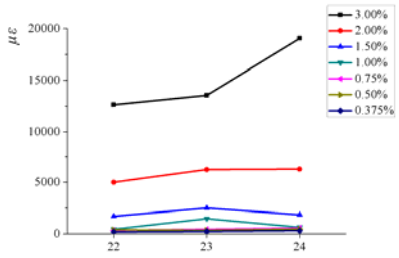

(c) Strain gauge No. 22-24

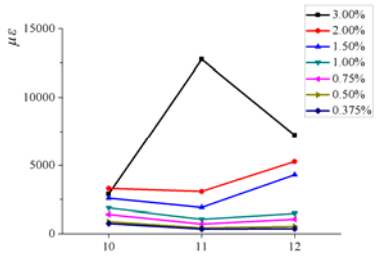

(d) Strain gauge No. 10-12

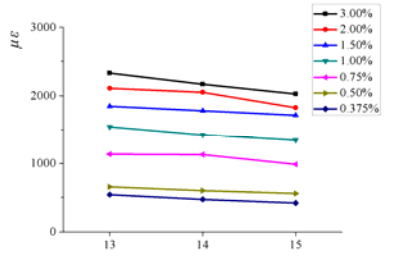

(e) Strain gauge No. 13-15

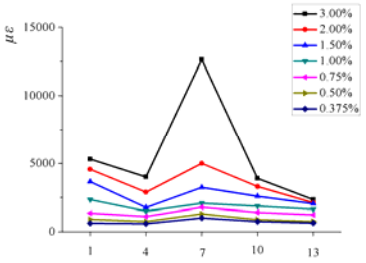

(f) Strain gauge No. 1,4,7,10,13

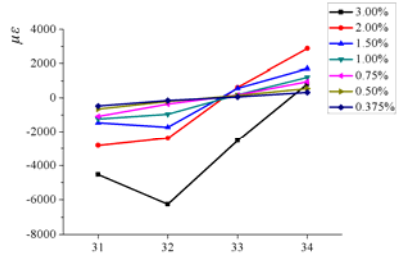

(g) Strain gauge No. 31-34

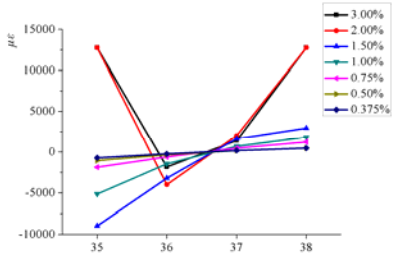

(h) Strain gauge No. 35-38

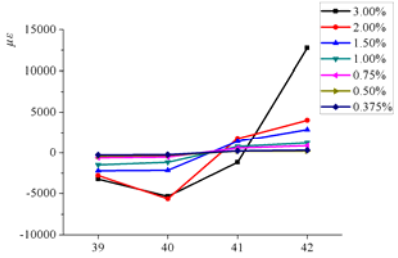

(i) Strain gauge No. 39-42

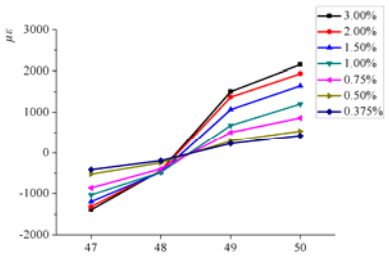

(j) Strain gauge No. 47-50

Figure 13. Strain Distribution of Specimen JD-2

4.3 Strains of Specimen JD-3

Figure 14(a)-(f) show the typical strain profile measured across the width of beam flange at different positions along its span, illustrating the different behavior which occurred. It is worth noting the more evident change in the strain distribution as the cross-section is closer to the connection, mainly attributed to the more extensive inelastic yielding of the steel beam. An examination of the strains of the beam flange in the fractured area indicates that a significant amount of strain had developed there. Reading from strain gauges located near the crack revealed a strain had developed that exceeded 14,000 microstrain before fracture occurred. Strain gauge readings revealed that a shear lag phenomenon developed along the width of through-diaphragm, where the longitudinal strain was relatively larger in the location adjacent to the horizontal stiffener. This indicates that a significant amount of the beam's flange force was transferred from the triangle plates to the sides of the steel tube that formed the connection's panel zone.

Figure 14(g) illustrates response of the bottom flange strains along the longitudinal direction. The strains were measured at the distance of 0 mm, 120 mm, 235 mm, 350 mm, 650 mm, and 950 mm, respectively, from the column face. The specimen had less strain at both sides than it did in the center of the beam. It is attributed to the effort of tapered plates which shares a large amount of force transferred through the sides of the beam flange. It should be noted that the maximum strain of the top and bottom flanges for Specimen JD-3 was obviously less than that in Specimen JD-1, which implied that the triangular plates can affect the strain distribution of the beam.

The web strain response of Specimen JD-3 is shown in Figure 14(h)-(k). The yielding first developed at the region 120 mm from the column face, which is expected since the its access hole had a 300 mm longitudinal cut deep in the web of the beam, and the reduced web section of the beam force most of the deformation occurring within this region.

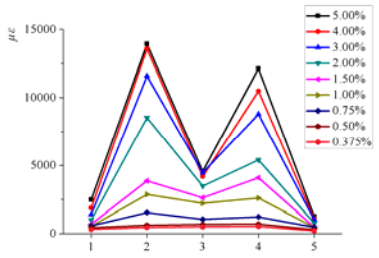

(a) Strain gauge No. 1-5

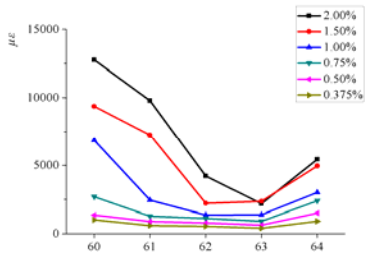

(b) Strain gauge No. 60-64

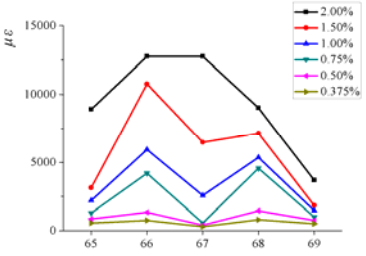

(c) Strain gauge No. 65-69

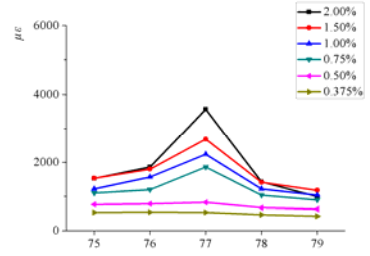

(d) Strain gauge No. 75-79

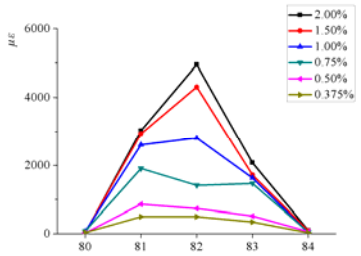

(e) Strain gauge No. 80-84

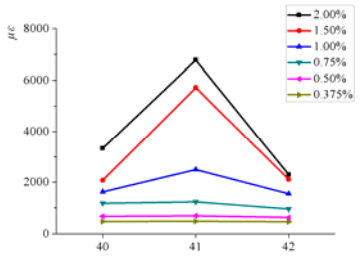

(f) Strain gauge No. 40-42

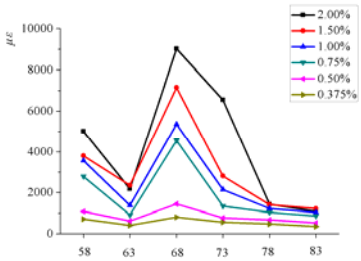

(g) Strain gauge No. 58,63,68,73,78,83

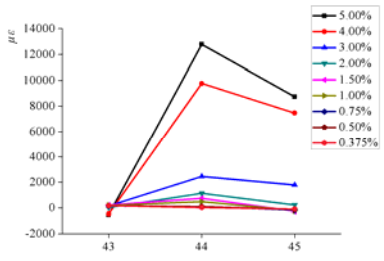

(h) Strain gauge No. 43-45

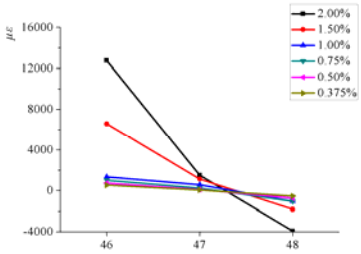

(i) Strain gauge No. 46-48

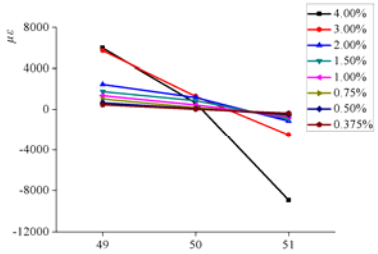

(j) Strain gauge No. 49-51

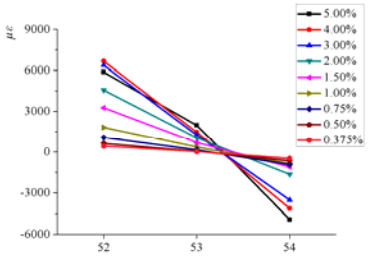

(k) Strain gauge No. 52-54

Figure 14. Strain Distribution of Specimen JD-3

4.4 Key Findings

Comparison of strain distribution among four connections indicates that, it is evident that the behavior in the beam strain was considerably influenced by the variation in the connection details, as illustrated by results of Specimen JD-1, JD-2, and JD-3.

In the figure, it can be observed that both the web and flanges of the beams near the connections in all specimens had far exceeded the yield strain. The traditional through-diaphragm connection (Specimen JD-1) appeared to be the highest stressed at both the diaphragm and the beam flange at the same load level. This phenomenon demonstrates that providing improvement to connection configuration guarantees an increase in rotation capacity and a significantly higher strength

capacity. Moreover, the connection details have a significant influence on the position of the plastic hinge and determine whether or not the force can be sufficiently delivered from the steel beam to the CFRT column.

Meanwhile, Specimen JD-3 had the highest strain values in the web, which is reasonable since the deep longitudinal cut in the web results in the stress concentration there. This is also the region that was designed to absorb the seismic energy and thus, provide a ductile behavior of the through-diaphragm connection.

5. SUMMARY AND CONCLUSIONS

In this paper, an experimental program comprising four through-diaphragm connections subjected to cyclic load was conducted, and the relationship of lateral force versus beam-column rotation, shear force versus shear distortion curves, deformation, and strain distribution were analyzed. The main conclusions can be drawn as follows:

(1) The lateral force versus beam-column rotation response of the proposed connections was obviously enhanced when compared to the traditional connection, attributed to the improved geometrical detail of the connection. This indicates that seismic resistance of the proposed connections is much better than the existing one. As a result, the proposed types are more suitable for application in moment resisting frames in seismic regions.

(2) The stiffness of the proposed connections is higher than that of the traditional one. Therefore, the beneficial effect of the elements surrounding the panel zone should be taken into account to calculate the shear stiffness.

(3) The deformation of the beam end is the largest contribution to the total displacement of the connection. This demonstrates that more yielding occurred there.

(4) The connection details clearly affect the load path how the force is transferred from the beams to the columns. Additionally, the proposed types significantly alleviate the stress concentration in the beam flange and evidently enhance the ductility of the traditional connection.

ACKNOWLEDGEMENTS

This work is sponsored by the National Natural Science Foundation of China (Grant No. NSFC61272264), the twelfth five-year national science and technology support program (Grant No. 2011BAJ08B02-04) and key project in the Tianjin Science & Technology Pillar Program (Grant No. 11ZCGYSF01000). The authors would like to thank the Zhejiang Hangxiao Steel Structure Co. Ltd. for the supply of test specimens, the Architecture Design Co. Ltd of Tadi for technical support on the specimen design, Wan Fanggui of Tianjin University and Wang Hailiang, Yang Xinlei, Ren Quancang, Bao Quanli, Jin Cheng, Wang Zhenyu of Tianjin Chengjian University for their assistance with the laboratory work. The authors also appreciate the financial support provided by the Chinese Scholarship Council (File No. 201206250067) that enables the Visiting Research Scholar to cooperate with Dr. Benjamin W. Schafer at Johns Hopkins University at Baltimore.

REFERENCES

[1] Kang, C.H., Shin, K.J., Oh, Y.S. and Moon, T.S., "Hysteresis Behavior of CFT Column to H-beam Connections with External T-stiffeners and Penetrated Elements", Engineering Structures, 2001, Vol. 23, No. 9, pp. 1194-1201.

[2] Varma, A.H., Ricles, J.M., Sause, R. and Lu, L.W., "Seismic Behavior and Modeling of High-strength Composite Concrete-filled Steel Tube (CFT) Beam-columns", Journal of Constructional Steel Research, 2002, Vol. 58, No. 5-8, pp. 725-758.

[3] Ricles, J.M., Peng, S.W. and Lu, L.W., "Seismic Behavior of Composite Concrete Filled Steel Tube Column-wide Flange Beam Moment Connections", Journal of Structural Engineering, 2004, Vol. 130, No. 2, pp. 223-232.

[4] Shin, K.J., Kim, Y.J., Oh, Y.S. and Moon, T.S., "Behavior of Welded CFT Column to H-beam Connections with External Stiffeners", Engineering Structures, 2004, Vol. 26, No. 13, pp. 1877-1887.

[5] Cheng, C.T., Chan, C.F. and Chung, L.L., "Seismic Behavior of Steel Beams and CFT Column Moment-resisting Connections with Floor Slabs", Journal of Constructional Steel Research, 2007, Vol. 63, No. 11, pp. 1479-1493.

[6] Wu, L.Y., Chung, L.L., Tsai, S.F., Lu, C.F. and Huang, G.L., "Seismic Behavior of Bidirectional Bolted Connections for CFT Columns and H-beams", Engineering Structures, 2007, Vol. 29, No. 3, pp. 395-407.

[7] Nie, J.G., Qin, K. and Cai, C.S., "Seismic Behavior of Connections Composed of CFSSTCs and Steel-concrete Composite Beams—Experimental Study", Journal of Constructional Steel Research, 2008, Vol. 64, No. 10, pp. 1178-1191.

[8] Wang, W.D., Han, L.H. and Zhao, X.L., "Analytical Behavior of Frames with Steel Beams to Concrete-filled Steel Tubular Column", Journal of Constructional Steel Research, 2009, Vol. 65, No. 3, pp. 497-508.

[9] Park, S.H., Choi, S.M., Kim, Y.S., Park, Y.W. and Kim, J.H., "Hysteresis Behavior of Concrete Filled Square Steel Tube Column-to-beam Partially Restrained Composite Connections", Journal of Constructional Steel Research, 2010, Vol. 66, No. 7, pp. 943-953.

[10] Qin, Y., Chen, Z., Yang, Q. and Shang, K., "Experimental Seismic Behavior of Through-Diaphragm Connections To Concrete-Filled Rectangular Steel Tubular Columns", Journal of Constructional Steel Research, 2014, Vol. 93, pp. 32-43. http://dx.doi.org/10.1016/j.jcsr.2013.10.020

[11] Qin, Y., Chen, Z. and Wang, X., "Experimental Investigation of New Internal-Diaphragm Connections to CFT Columns Under Cyclic Loading", Journal of Constructional Steel Research, 2014, Vol. 98, pp. 35-44. http://dx.doi.org/10.1016/j.jcsr.2014.02.014

[12] Kawano, A., Matsui, C. and Murai, N., "Load-deformation Relationship Models for Local Deformations in Diaphragm-stiffened Connections of H-shaped Steel Beams to Rectangular CFT Columns", Steel Construction Engineering, 1998, Vol. 5, No. 17, pp. 93-104.

[13] Koester, B.D., "Panel Zone Behavior of Moment Connections between Rectangular Concrete-filled Steel Tubes and Wide Flange Beams", Ph.D. thesis, The University of Texas at Austin, Austin, 2000.[14] Lu, X.L., Yu, Y., Kiyoshi, T. and Satoshi, S., "Experimental Study on the Seismic Behavior in the Connection between CFRT Column and Steel Beam", Structural Engineering and Mechanics, 2000, Vol. 9, No. 4, pp. 365-374.

[15] Morino, S. and Tsuda, K., "Design and Construction of Concrete-filled Steel Tube Column System in Japan", Earthquake Engineering and Engineering Seismology, 2002, Vol. 4, No. 1, pp. 51-73.

[16] Fukumoto, T. and Morita, K., "Elastoplastic Behavior of Panel Zone in Steel Beam-to-concrete Filled Steel Tube Column Moment Connections", Journal of Structural Engineering, 2005, Vol. 131, No. 12, pp. 1841-1853.

[17] Park, J.W., Kang, S.M. and Yang, S.C., “Experimental Studies of Wide Flange Beam to Square Concrete-filled Tube Column Joints with Stiffening Plates Around the Column”, Journal of Structural Engineering, 2005, Vol. 131, No. 12, pp.1866-1876.

[18] Jiang, X.L., Miao, J.K. and Chen, Z.H., “Experiment on Seismic Performance of Diaphragm-through Joint between Concrete-filled Square Steel Tubular Column and Steel Beam”, Journal of Tianjin University, 2009, Vol. 42, No. 3, pp. 194-200.

[19] Nie, J.G., Qin, K. and Cai, C.S., “Seismic Behavior of Composite Connections – Flexural Capacity Analysis”, Journal of Constructional Steel Research, 2009, Vol. 65, No. 5, pp. 1112-1120.

[20] Rong, B., Chen, Z.H., Zhang, R.Y., Apostolos, F. and Yang, N., “Experimental and Analytical Investigation of the Behavior of Diaphragm-through Joints of Concrete-filled Tubular Columns”, Journal of Mechanics of Materials and Structures, 2012, Vol. 7, No. 10, pp. 909-929.

[21] Qin, Y., Chen, Z. and Wang, X., “Elastoplastic Behavior of Through-Diaphragm Connections to Concrete-Filled Rectangular Steel Tubular Columns”, Journal of Constructional Steel Research, 2014, Vol. 93, pp. 88-96. http://dx.doi.org/10.1016/j.jcsr.2013.10.011

[22] Qin, Y., Chen, Z. and Rong, B., “Component-Based Mechanical Models for Axially-Loaded Through-Diaphragm Connections to Concrete-Filled RHS Columns”, Journal of Constructional Steel Research, 2014, Vol. 102. [in press] http://dx.doi.org/10.1016/10.1016/j.jcsr.2014.06.016

[23] Qin, Y., Chen, Z. and Han, N., “Research On Design of Through-Diaphragm Connections Between CFRT Columns and HSS Beams”, International Journal of Steel Structures, 2014. [in press]

[24] Loh, H.Y., Uy, B. and Bradford, M.A., “The Effects of Partial Shear Connection in Composite Flush End Plate Joints Part Ⅰ — Experimental Study”, Journal of Constructional Steel Research, 2006, Vol. 62, No. 4, pp. 378-390.

[25] Wang, J.F., Han, L.H. and Uy, B., “Behaviour of Flush End Plate Joints to Concrete-filled Steel Tubular Columns”, Journal of Constructional Steel Research, 2009, Vol. 65, No. 4, pp. 925-939.

[26] Tizani, W., Wang, Z.Y. and Hajirasouliha, I., “Hysteretic Performance of a New Blind Bolted Connection to Concrete Filled Columns under Cyclic Loading: An Experimental Investigation”, Engineering Structures, 2013, Vol. 46, pp. 535-546.

[27] Málaga-Chuquitaype, C. and Elghazouli, A.Y., “Behaviour of Combined Channel/Angle Connections to Tubular Columns under Monotonic and Cyclic Loading”, Engineering Structures, 2010, Vol. 32, No. 6, pp. 1600-1616.

[28] Wu, L.Y., Chung, L.L., Tsai, S.F., Shen, T.J. and Huang, G.L., “Seismic Behavior of Bolted Beam-to-column Connections for Concrete Filled Steel Tube”, Journal of Constructional Steel Research, 2005, Vol. 61, No. 10, pp. 1387-1410.

[29] Tort, C. and Hajjar, J.F., “Capacity Assessment of Rectangular Concrete-filled Steel Tube (RCFT) Members and Connections for Performance-based Design of Composite Frames”, Structures Congress 2005, New York, United States, April 20-24, 2005.

[30] Zhao, H.L., Kunnath, S.K. and Yuan Y., “Simplified Nonlinear Response Simulation of Composite Steel-concrete Beams and CFST Columns”, Engineering Structures, 2010, Vol. 32, No. 9, pp. 2825-2831.

[31] Choi, Y.H., Routch, D.A. and LaFave, J.M., “New Approach to AISC P-M Interaction Curve for Square Concrete Filled Tube (CFT) Beam-columns”, Engineering Structures, 2006, Vol. 28, No. 11, pp. 1586-1598.

[32] Shams, M. and Saadeghvaziri, M.A., “State of the Art of Concrete-filled Steel Tubular Columns”, ACI Structural Journal, 1997, Vol. 94, No. 5, pp. 558–571.

[33] Shanmugam, N.E. and Lakshmi, B., “State of the Art Report on Steel–concrete Composite Columns”, Journal of Constructional Steel Research, 2001, Vol. 57, No. 10, pp. 1041–1080.
[34] Nishiyama, I., Morino, S., Sakino, K. et al., “Summary of Research on Concrete-filled Structural Steel Tube Column System Carried Out under the US–Japan Cooperative Research Program on Composite and Hybrid Structures”, BRI Research Paper No.147, Japan: Building Research Institute, 2002.
[35] Kurobane, Y., Packer, J.A., Wardenier, J. and Yeomans, N., “Design Guideline for Structural Hollow Section Column Connections”, Germany, 2004.
[36] Chen, Z., Qin, Y. and Wang, X., “Development of Connections to Concrete-Filled Rectangular Tubular Columns”, Advanced Steel Construction, 2014. [in press]
[37] Fukumoto, T., “Steel–beam–to–concrete–filled–steel–tube-column Moment Connections in Japan”, Steel Structures, 2005, Vol. 5, No. 4, pp. 357-365.
[38] Choi, S., Lee, S., Hong, S. and Kim, J., “Structural Capacities of Tension Side for CFT Square Column-to-beam Connections with Combined-cross Diaphragm”, Advances in Structural Engineering, 2008, Vol. 11, No. 2, pp. 209-227.
[39] You, J., Chen, G. and Han, L., “Preliminary Discussion on Dimension of Ring of Concrete-filled Steel Tube Column Joint with External Ring”, Journal of Harbin Institute of Technology, 2005, Vol. 37, pp. 354-357.
[40] ANSI/AISC 341-10, “Seismic Provisions for Structural Steel Buildings”, Chicago (IL), 2010.
[41] Faella, C. and Rizzano, G., “Structural Steel Semirigid Connections: Theory, Design and Software”, Fla (Boca Raton): CRC Press, 2000.